Volume Conformal Irradiation of Moving Target Volumes with Scanned Ion Beams

Vom Fachbereich Physik
der Technischen Universität Darmstadt

zur Erlangung des Grades
eines Doktors der Naturwissenschaften
(Dr. rer. nat.)

genehmigte Dissertation von

Dipl.-Phys. Sven Oliver Grözinger

aus Wiesbaden

Darmstadt 2004

D17

Referent:	Prof. Dr. G. Kraft
Korreferent:	Prof. Dr. D. H. H. Hoffmann
Tag der Einreichung:	25.11.2003
Tag der Prüfung:	26.01.2004

"Nicht weil die Dinge unerreichbar sind, wagen wir sie nicht – weil wir sie nicht wagen, bleiben sie unerreichbar."

Lucius Annaeus Seneca, römischer Philosoph

Zusammenfassung

Die intensitäts-modulierte Rasterscantechnik ermöglicht eine extrem präzise Bestrahlung von Tumoren, deren Position exakt fixiert werden kann und die sich nicht bewegen. Im Rahmen dieser Arbeit wurde untersucht, wie sich das Rasterscanverfahren auf bewegte Zielvolumina, z. B. im Thoraxbereich, ausdehnen lässt. Dabei wurden zwei Strategien betrachtet: Eine Mehrfachbestrahlung, die nicht mit der Bewegung korreliert ist, und eine aktive Nachführung des Strahls während der Bestrahlung in allen drei Dimensionen.
Die Simulationen und Experimente zur Mehrfachbestrahlung zeigten, dass sich die Dosisverteilung in einem Teilbereich des Bestrahlungsfeldes verbessern lässt, dass der Randbereich des Feldes aber stark inhomogen bleibt. Um die Homogenität über das gesamte Zielvolumen zu steigern, wäre es notwendig, das Bestrahlungsfeld zu vergrößern und damit die Konformität der Bestrahlung aufzugeben. Dies würde zu einem erhöhten Dosisbeitrag im gesunden Gewebe des Tumorbettes führen.
Durch eine aktive Strahllagekorrektur während der Bestrahlung wird dagegen eine Verschmierung der Dosisverteilung vermieden. In Simulationsrechnungen wurde der Einfluss verschiedener Bewegungsparameter auf die Dosishomogenität untersucht. Basierend auf diesen Rechnungen wurde ein Prototyp System zur Strahllagekorrektur in allen drei Dimensionen aufgebaut. In diesem System wird die Kompensation der lateralen Zielbewegung in den Rastermagneten verwirklicht. Zur Kompensation der Tiefenvariation wird ein schnelles, passives Keil-Absorber System verwendet, das von Linearmotoren angetrieben wird. Beide Systeme ermöglichen eine Anpassung der Strahlposition mit einer Genauigkeit von besser als einem Millimeter. Mit diesem Korrektursystem konnten die Homogenität und die Kontur der Dosisverteilung für Bewegungen, die dem Atemzyklus entsprachen, mit einer Genauigkeit von 1-2 % der statischen Bestrahlung angenähert werden.

Abstract

The intensity modulated raster scanning technique enables an extremely precise irradiation of tumours, which can be fixed in position and do not move. This thesis investigates how to extend raster scanning to moving target volumes, like in the thorax. Two different strategies were studied: A rescanning of the volume which is not correlated to the target motion and an active realignment of the beam in all three dimensions during the irradiation (online motion compensation).
The simulations and experiments concerning rescanning showed that the dose distribution can be improved in a limited part of the irradiation field, but the border area of the field remains strongly inhomogeneous. To improve the homogeneity over the whole target volume an extension of the irradiation field would be required, sacrificing volume conformity and increasing the dose contribution to the normal tissue in the tumour bed.
The approach of active realignment of the beam during the irradiation avoids smearing of the dose distribution. In simulations the effect of different motion parameters on the dose homogeneity was calculated. Based on these calculations, a prototype for online motion compensation was constructed. In this setup the compensation of lateral motion components was realised with the scanning magnets. Longitudinal motion compensation was achieved with a fast, passive wedge system driven by linear motors. Both systems enabled an online realignment of the beam position with sub-millimetre precision. This prototype setup allowed the delivery of static dose distributions to targets, which were subject to respiration-like motion, with a precision of 1-2 %.

Contents

List of Figures xi

List of Tables xiii

List of Abbreviations xv

1 Introduction 1

2 Radiation Cancer Therapy 5
2.1 Basic Physical Properties 5
2.2 Conventional Radiotherapy 9
2.3 Biological Effects of Charged Particles 11
2.4 Heavy Ion Therapy 12
2.4.1 Beam Delivery 12
2.4.2 Patient Positioning 17
2.4.3 Treatment Verification – PET 18
2.4.4 Treatment Planning 19

3 Target Motion in Cancer Therapy 21
3.1 Types of Target Motion 22
3.2 Parameters of Respiration-Related Target Motion 23
3.3 Tracking of Target Motion 24
3.3.1 Direct Motion Measurements 25
3.3.2 Indirect Motion Measurements 28
3.4 Consequences and Management of Respiration-Related Motion . . . 30
3.4.1 Rescanning 31
3.4.2 Gating 32
3.4.3 Online Compensation 35

4 Simulating the Effect of Target Motion 39
4.1 Simulation Environment 39
4.1.1 Dose Calculation Algorithm 40
4.1.2 Time Correlation via Beam Intensity Profile 44

4.2 Target Configuration 47
4.3 Results 47
4.3.1 Influence of the Beam Spill Profile 47
4.3.2 Translation of Target Volume 49
4.3.3 Rotation of Target Volume 57
4.3.4 Strategies for Compensation 59

5 A Motion Compensation System for Heavy Ion Therapy 65
5.1 Motion Adapted Heavy Ion Therapy 65
5.2 Prototype Setup for Motion Adapted Beam Delivery 69
5.2.1 Fast Range Modulation 70
5.2.2 Lateral Motion Compensation 72
5.2.3 3D Motion Compensation 73

6 Experimental Means and General Sources of Errors 77
6.1 Inducing Target Motion 77
6.1.1 Lateral Motion 78
6.1.2 Longitudinal Motion 79
6.2 Online Motion information 82
6.2.1 Data Connection 82
6.2.2 Lateral Positioning Accuracy 83
6.2.3 Accuracy of Depth Variation 83
6.3 Experimental Verification of Dose Distributions 85
6.3.1 Water Column for Depth Dose Verification 85
6.3.2 X-Ray Films for Lateral (2D) and 3D Dose Verification . . . 85
6.3.3 BANG^{TM} Gels for full 3D Dose Verification 88

7 Feasibility Study for 3D Online Motion Compensation 91
7.1 Rescanning the Target Volume 91
7.1.1 Experimental Setup 91
7.1.2 Data Analysis 92
7.1.3 Results and Discussion 93
7.2 Lateral Online Motion Compensation 98
7.2.1 Experimental Setup 98
7.2.2 Data Analysis 99
7.2.3 Results and Discussion 100
7.3 Longitudinal Online Motion Compensation 109
7.3.1 Experimental Setup 110
7.3.2 Data Analysis 111
7.3.3 Results and Discussion 111
7.4 Online Motion Compensation on Complex 3D Target Volumes . . . 115
7.4.1 Experimental Setup 117

7.4.2 Data Analysis 119
7.4.3 Results and Discussion 120

8 Summary and Outlook **127**

Zusammenfassung und Ausblick **129**

A Terms and Terminology **133**
A.1 Geometrical Concepts in Radiation Cancer Therapy 133
A.2 Anatomical Directions and Planes 134

B Estimation of Respiration-Related Target Rotation **137**

C Medical Imaging Methods **141**
C.1 X-ray imaging 141
C.2 Computed Tomography (CT) 142
C.3 Nuclear Medicine 144
C.4 Magnetic Resonance Imaging (MRI) 145
C.5 Ultrasound Imaging 147

D Construction of PMMA Wedges **151**

E Software for the Prototype Setup **153**
E.1 SAM Programs for Motion Compensation 153
E.2 Wedge Drive Control System 155

F Time Behaviour of the Data Connection **157**

Bibliography **161**

List of Figures

1.1 Comparison of photon IMRT and ^{12}C dose distribution 2

2.1 Depth dose profile of photons and ^{12}C ions 7
2.2 Lateral beam broadening for photons, protons and ^{12}C ions 9
2.3 Composition of ^{12}C depth dose profile 10
2.4 Comparison of biological effective and physical absorbed dose 12
2.5 Irradiating extended target volumes with single Bragg peaks 13
2.6 Conformal tumour irradiation with passive systems 14
2.7 Principle of intensity controlled magnetic raster scanning 15
2.8 Patient head mask for stereotactic fixation 18

3.1 Schematic drawing of the TULOC assembly 28
3.2 Principle of respiratory gated irradiation 33
3.3 Gating with variable accelerator cycle 34
3.4 Principle of online motion adapted x-ray therapy 36
3.5 Effect of variations in radiological path length 37

4.1 Relation between CT and raster coordinate system 42
4.2 Dose calculation for moving target volumes 43
4.3 Measured beam spill profile vs. reduced data set 45
4.4 Comparison of two reduced spill profiles 46
4.5 Inhomogeneous particle deposition for a spherical target 48
4.6 Dose homogeneity for different beam spill profiles 49
4.7 Difference in dose homogeneity for different beam spill profiles . . . 50
4.8 Dose distribution histogram of a single IES 51
4.9 Dose homogeneity dependence on motion amplitude and direction . 53
4.10 Influence of the motion direction on the dose distribution 54
4.11 Dose homogeneity dependence on initial phase 56
4.12 Dose homogeneity dependence on motion period 57
4.13 Change of relative voxel position due to target rotation 58
4.14 Dose homogeneity dependence on target rotation 59
4.15 Phase dependent dose homogeneity after 10 times rescanning 60
4.16 Effect of rescanning the target 61

4.17 Active motion compensation on target translation 62
4.18 Active motion compensation on target rotation 63

5.1 Motion adapted heavy ion therapy 66
5.2 Ideal vs. real depth dose distribution of ion beams 68
5.3 Wedge drive system for fast, passive energy modulation 70
5.4 Longitudinal motion compensation 71
5.5 3-dimensional online motion compensation 73
5.6 Components and communication links of the prototype setup 75

6.1 3D positioning table for lateral target motion 78
6.2 Measured lateral target displacement 80
6.3 Phantom for changing the WEL 82
6.4 Calibration of phantom for WEL changes 84
6.5 Water column setup for depth dose distribution measurement . . . 86
6.6 Film stack for 3D dose verification 87
6.7 Calibration of film response 88

7.1 Dose distributions for rescanning 93
7.2 Film measurements: rescanning 95
7.3 Effect of rescanning on dose homogeneity 96
7.4 Film measurements: point pattern 100
7.5 Lateral compensation accuracy 101
7.6 Film measurements: line pattern 102
7.7 Horizontal compensation accuracy 103
7.8 Vertical compensation accuracy 104
7.9 Different motion data update rates 105
7.10 Film measurements: homogeneous square 107
7.11 Effect of compensation rate on dose profiles 108
7.12 Influence of wedges on beam profile 112
7.13 Compensation of three alternating energies 113
7.14 Compensating random changes in initial energy 114
7.15 Compensation of continuous density changes 116
7.16 Patient plan for static tumour 118
7.17 Film measurement: spherical target volume 121
7.18 Compensation performance on extended target volume 122
7.19 Homogeneity over spherical target volume 123
7.20 BANG^{TM} gel measurement: realistic patient plan 124
7.21 Compensation performance on realistic patient plan 125

A.1 Geometrical target concepts in cancer therapy 133
A.2 Anatomical planes and directions 135

B.1 Estimation of target rotation amplitude 138

C.1 Generation of x-rays in an x-ray tube 141
C.2 Principle of CT measurement 143
C.3 Principle of PET measurement 144
C.4 Principle of ultrasound B-image acquisition 150

D.1 Construction of PMMA wedges 152

E.1 Process control for longitudinal motion compensation 156

F.1 Time lag analysis in data transfer 159

List of Tables

2.1 Scanning control unit: distribution of tasks 17

5.1 Mechanical properties of the wedge drive system 72

7.1 Effect of ROI size on dose inhomogeneity for rescanning 97
7.2 Fraction of misplaced dose with rescanning 97
7.3 Effect of 3D-OMC on dose homogeneity 109

C.1 Typical longitudinal relaxation times for MRI 146
C.2 Sound velocity in biological material 148
C.3 Typical parameters for diagnostic ultrasound imaging 149

E.1 List of VIs in *wedgedrive.llb* library 156

List of Abbreviations

2D	two-**d**imensional
3D	three-**d**imensional
3D-OMC	three-**d**imensional **o**nline **m**otion **c**ompensation
a.p.	**a**ntero**p**osterior, from front to back
CAMAC	**c**omputer **a**utomated **m**easurement **a**nd **c**ontrol (internationally accepted IEEE standard)
CaveM	the medical treatment room at GSI Darmstadt
CT	**c**omputed **t**omograph(y)
CTV	**c**linical **t**arget **v**olume
DNA	**d**eoxyribo**n**ucleic **a**cid
DRR	**d**igitally **r**econstructed **r**adiograph
DSP	**d**igital **s**ignal **p**rocessor, fast, numeric micro-processor on-board the SAM modules
E7	VME processor card EUROCOM 7, Eltec Elektronik GmbH, Mainz (Germany)
FWHM	**f**ull **w**idth at **h**alf **m**aximum
GSI	**G**esellschaft für **S**chwer**i**onenforschung mbH, Planckstr. 1, 64291 Darmstadt, Germany
GTB	device bus, differential data bus connecting a SAM module with the assigned frontend electronics
GTV	**g**ross **t**arget **v**olume
Gye	**G**ra**y** **e**quivalent, unit for dose of particle radiation normalised to the effect of photon irradiation
HF	**h**igh **f**requency
HU	**h**ounsfield **u**nit, unit of CT information
IC	**i**onisation **c**hamber
IR	**i**nfra**r**ed
IMRT	**i**ntensity **m**odulated **r**adiation **t**herapy
IES	**i**so-**e**nergy **s**lice
LET	**l**inear **e**nergy **t**ransfer, $\mathrm{LET}_\infty \hat{=} \frac{dE}{dx}$ (LET_∞: all energy transfer processes included)
MLC	**m**ulti-**l**eaf **c**ollimator
MRI	**m**agnetic **r**esonance **i**maging/**i**mages

MWPC	**m**ulti**w**ire **p**roportional **c**hamber
NMR	**n**uclear **m**agnetic **r**esonance
OAR	**o**rgan **a**t **r**isk
PET	**p**ositron **e**mission **t**omograph(y)
pixel	picture element
PMMA	**P**oly**m**ethyl-**M**eth**a**crylat (known as plexiglass)
PSI	**P**aul **S**cherrer **I**nstitute, Villingen, Switzerland
PTV	**p**lanning **t**arget **v**olume
RBE	**r**elative **b**iological **e**ffectiveness
r.l.	**r**ight-**l**eft
ROI	**r**egion **o**f **i**nterest
SAM	VME module for control and read-out (**S**teuerungs- und **A**uslese**m**odul)
SCU	**s**canning **c**ontrol **u**nit
s.i.	**s**upero**i**nferior, from top to bottom
SMB	**s**hared **m**emory **b**lock
spill	ion pulse, corresponding to one synchrotron filling
TOM	**t**herapy **o**nline **m**onitor
US	**u**ltra**s**ound
VOI	**v**olume **o**f **i**nterest
voxel	volume element (analogous to pixel)
VME	real-time data bus (derived from Motorola's Versabus)
VDB	**V**SB **d**ifferential **b**us, converts VME TTL into differential signal, extents VSB to connect remote hardware
VSB	**V**ME **s**ubsystem **b**us
VI	**v**irtual **i**nstrument, program routine for the LabView environment
WE	**w**ater-**e**quivalent, normalised to density of water
WEL	**w**ater-**e**quivalent path **l**ength, the length along the particle path, converted to the density of water

Chapter 1

Introduction

Precision Tumour Therapy

As early as 1946 R. R. Wilson realised the therapeutic potential of energetic beams of protons and heavier ions[1] [Wil46]. Due to their physical properties and interaction mechanisms, such as the small lateral scattering, finite range and inverse depth dose profile, heavy, charged particles could deliver a higher dose to the tumour with the same contribution to the surrounding normal tissue than it was possible with photon beams.
With the most advanced technique for photon therapy, intensity modulated radiation therapy (IMRT), the high dose region can be matched quite closely to the shape of the tumour. Photon beams from multiple directions are superimposed to create a region of enhanced dose deposition deep inside the body. Computer controlled multileaf collimators are used for intensity modulation [Bra88] in order to fit the region of maximum dose deposition to the tumour shape and spare the surrounding structures. Using photon IMRT techniques, a similar conformity of the irradiated volume to the target volume can be achieved as with ion beam irradiation, but because of the exponential depth dose relation, the integral dose to the normal tissue is always significantly greater (cf. fig. 1.1(a)).
Compared to photons, ions show an inverse depth dose relation. Towards the end of the range, the energy deposition rises reaching a pronounced peak (Bragg peak) and finally drops sharply to zero. In the entrance channel (plateau region), the ionisation density is small compared to the peak region. Consequently, the proximal, healthy (normal) tissue is much less damaged than the target tissue. In the peak region, heavy ions like carbon have a several times higher relative biological effectiveness (RBE)[2]. In addition, the reduced lateral scattering of heavy ion beams compared to e. g. proton beams inside the tissue leads to a smaller beam diameter

[1] In this thesis, the term *ion* refers to the group of charged atoms, including the proton as the charged hydrogen atom, whereas the term *heavy ion* is used for all charged atoms heavier than hydrogen.

[2] The relative biological effectiveness is defined as the quotient of ion and photon dose leading to the same biological effect.

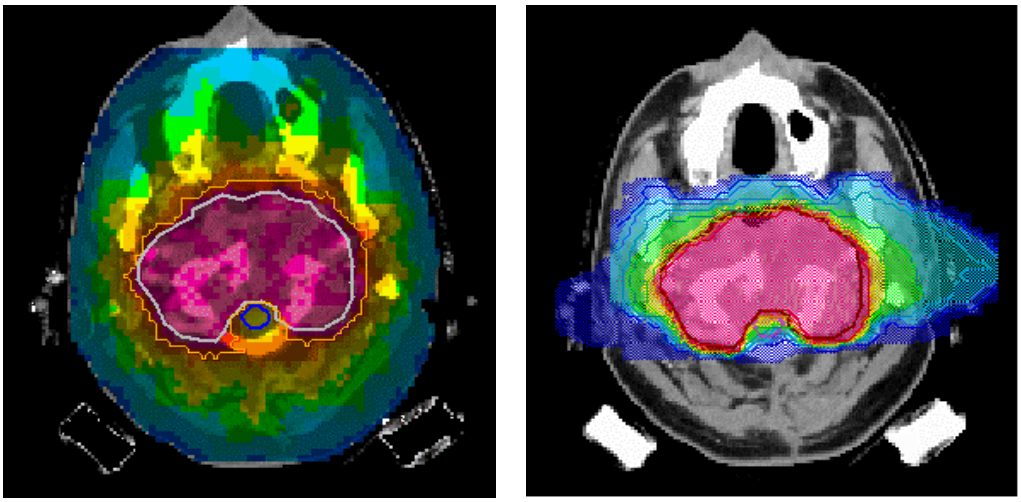

Figure 1.1:
Comparison of optimised dose distributions for a nine field photon IMRT (left) and a two field ^{12}C (right) treatment. The pictures show complete treatment plans for the same patient colour coded from high (red) to low dose (blue). In both cases the tumour is painted homogeneously with a high dose. However, in the photon case the brain-stem (organ at risk), as well as all the normal tissue receive significantly higher doses than in the ^{12}C case.

at the tumour. Combined with modern beam delivery techniques like magnetic raster scanning [Hab93], complex tumour shapes can be painted very accurately in 3D with a high dose level, whereas sharp dose gradients enable a maximum sparing of the surrounding normal tissue (cf. fig. 1.1(b)). For the best match of irradiated to target volume, the dose is applied point by point in 3 dimensions[3].
Outstanding volume conformal dose application has been achieved with scanned heavy ion beams [Kra00]. However, since the dose distribution is shaped to closely fit the target volume, the precision is limited by the knowledge of shape, size and position of the tumour at the time of irradiation. In clinical practice, sophisticated protocols for patient positioning at the beginning of each treatment session have been developed. As long as the tumour does not move during the irradiation (static case), a high spatial precision in dose delivery can be achieved. But in most parts of the body unavoidable organ motion causes a displacement, which destroys the high degree of volume conformity. All the spatial precision requires a fixed relation between target volume and beam's frame of reference. Any deviation between actual and planned target position causes distortions in the applied dose

[3]The "three-dimensional points"are called volume elements (voxels). So, more precisely, it is a voxel-by-voxel processing.

distribution and reduces the volume conformity. This problem is inherent to all conformal beam delivery techniques.
Displacements due to patient positioning and inter-fractional target motion are routinely minimised following dedicated protocols. Intensity modulated heavy ion therapy is currently only applied for indications in the head, neck and pelvic region or close to the spinal cord, where target motion can be fully suppressed by stereotactic fixation [Sch93b]. However, for dealing with intra-fractional motion no method has prevailed, yet. Each of the investigated strategies either sacrifices accuracy or drastically elongates the treatment time. The higher the aspired precision the more carefully all sources of target motion have to be taken into account. Intensity modulated heavy ion therapy, for instance, is up to now not feasible for the thorax or abdominal region, at all.

Aims of this work

The aim of this thesis is to develop a strategy of conformal heavy ion irradiation of moving target volumes. Up to now, the fully active, magnetic raster scanning technique [Hab93] is only feasible for the irradiation of immobilised targets. However, the lateral scanning system has a speed of up to $10\,\frac{\mathrm{m}}{\mathrm{s}}$ for the maximum beam rigidity (up to $30\,\frac{\mathrm{m}}{\mathrm{s}}$ for the lowest energies), which is much greater than the maximum speed of most organ motion. Therefore, it seems reasonable to study the possibility of following the target motion online with the pencil beam in all three dimensions. For the longitudinal motion component (the change in depth), a similar fast tool is available with the depth scanning system developed earlier [Web00]. The combination of both systems, the lateral magnetic and the depth scanning, provides an universal tool to online adapt the position of the pencil beam. In this thesis, the correction for target motion is studied under the precondition that the actual location of the target volume is known at any time. The problems of online motion tracking and applying time differential dose corrections will not be a subject of this work.
The investigations in this thesis, concerning the effect of target motion on the dose delivered to exemplary target volumes, refer to respiration-like target motion. The simulations are based on an extension of the well proven treatment planning software for particle irradiation (TRiP98) [Krä01]. The study of several strategies for motion compensation leads to the concept of 3D online motion compensation (3D-OMC) as the most suitable method for heavy ion irradiation. The results of the simulations define the boundary conditions, requirements and technical parameters for the design of the corresponding prototype system. During the irradiation, 3D-OMC combines the pre-determined scanning parameters with a measured 3D target displacement vector, to deposit the planned number of particles at the planned position inside a moving target volume. The active compensation of motion does not

require any regular interruptions of the irradiation process, and therefore does not elongate the treatment time. For compatibility reasons, the prototype setup should follow the philosophy of the existing raster scanning facility and would ideally be the outline of an upcoming system upgrade. On the other hand, the ongoing clinical study for immobilised tumours allows only minor changes to the existing therapy control system, that must not influence the safety or the performance of the patient treatments. Although the primary range of use will be respiration-related motion compensation in the thoracic and abdominal region, the design should be flexible enough to deal with other kinds of slow target motion.
The performance of the prototype setup and the applicability of 3D online motion compensation for the irradiation of moving target volumes is proven in a feasibility study. This study utilises irradiation phantoms, which allow a mechanical position measurement. A flexible interface will combine with any suitable motion tracking system. The major parameter to be investigated is the applied dose distribution. In the case of total motion compensation, the dose distribution will be equivalent for all states of target motion. Although the experiments are performed with carbon beams and the prototype setup is dimensioned for ^{12}C ions, the general considerations are valid for all ion species.
Chapter 2 of this thesis summarises the current status of heavy ion tumour therapy[4] for static target volumes, based on GSI's therapy project. After looking into the general difficulties introduced by the presence of target motion in chapter 3, the motion-related effect on the applied dose distribution is simulated for heavy ion therapy in chapter4. In chapter 5 the design of the prototype setup for 3D-OMC is discussed. The experimental methods used in the feasibility study and the resulting sources of errors are presented in chapter 6. Chapter 7 contains the experimental feasibility study of the compensation method.

[4] "Heavy ion" refers to all ions heavier than hydrogen. The term *heavy* does not reflect the actual mass of the ions but their increased biological effectiveness.

Chapter 2

Radiation Cancer Therapy

Despite the enormous developments in cancer therapy, a large fraction of patients with localised tumours is still impossible to be cured. In contrast to metastatic tumours, localised ones can usually be precisely delineated and therefore directly addressed. Many tumours are located close to critical structures[1]. In those cases complete resection by surgery is frequently impossible and conventional radiation therapy often fails, because the maximum dose to the tumour volume is limited by the contribution to the surrounding, normal tissue. Only extremely volume conformal irradiation techniques allow the necessary dose escalation while sparing the organs at risk (OAR). A further escalation in conformity can only be reached when moving from photon to ion beams. It is estimated that more than 10 000 patients in Germany will benefit from the conformal dose application of ion therapy [Deb98].

2.1 Basic Physical Properties

As a result of the different physical interaction mechanisms, electromagnetic radiation (photons) and heavy charged particles (protons or heavier ions) show fundamental differences in dose deposition pattern. The deposited dose in units of Gray (1 Gy=1 J/kg) is defined as the total energy absorbed per unit mass

$$D(\vec{x}) = \left.\frac{dE}{dm}\right|_{\vec{x}} \tag{2.1}$$

The physical dose equals the differential energy deposition from all penetrating particles divided by the mass of the volume element. For thin targets the dose in Gy deposited by a parallel beam of particles is given by

$$D = 1.6 \cdot 10^{-9} \cdot \frac{dE}{dx} \cdot F \cdot \frac{1}{\rho} \tag{2.2}$$

[1]The term *critical structure* refers to organs which fulfil important functions for the living organism, e. g. brain stem, visible nerve, gut etc. Irreparable damage to these structures causes functional failure and has to be avoided. Such organs, in general, do not show a high radioresistance.

with the differential energy loss $\frac{dE}{dx}$ in $\frac{\text{keV}}{\mu\text{m}}$, the target mass density ρ in $\frac{\text{g}}{\text{cm}^3}$ and the particle fluence[2] F in cm^{-2}.
The interaction of electromagnetic radiation and matter is based on three fundamental processes:

1. Photoelectric Effect
2. Compton Scattering
3. Pair Production

All of these processes completely remove the interacting photon from the beam [Leo94]. The penetrating photons are therefore those who did not interact at all. Their number, i. e. the intensity of the beam, is reduced exponentially

$$I(x) = I_0 \exp(-\mu x) \tag{2.3}$$

with initial intensity I_0, thickness of absorber x and absorption coefficient μ.
Compton scattering dominates for high energetic photons. Since the Compton electrons are strongly forward scattered some of the transferred energy is transported a few centimetres deeper into the tissue and the energy deposition in the first tissue layers is smaller than the intensity loss of the photon beam. In a depth corresponding to the mean electron range an equilibrium in the electron distribution is established and the deposited energy reaches a maximum. For larger depths the dose decreases exponentially due to the reduction in photon intensity. The position of the maximum depends on the initial photon energy. For therapeutically relevant, high-energetic electron bremsstrahlung the depth of the maximum is in the order of a few centimetres [Kra00].
Due to electromagnetic coupling, heavy charged particles interact in a different way. The main two atomic interaction processes are:

1. Inelastic Collisions with atomic target electrons
2. Elastic Scattering from target nuclei

In the therapeutically relevant energy regime from approximately 85 to 430 MeV/u, inelastic collisions with atomic target electrons are mainly responsible for the ion's energy loss. This is described by the Bethe-Bloch formula [Bet30, Blo33]

$$-\frac{dE}{dx} = \frac{4\pi e^4 z_{eff}^2}{m_e v^2} nZ \ln \frac{2m_e v^2}{I} + \text{relativistic corrections} \tag{2.4}$$

with the electron charge e and mass m_e, the effective ion charge z_{eff} and velocity v, the atomic density $n = \frac{N_A}{A}\rho$ (N_A is Avogadro's Constant, A the atomic mass

[2] fluence = number of particles per unit area

and ρ the mass density), the atomic number Z and the average excitation energy I of the target medium.
At high energies the $\frac{1}{v^2}$ term is dominating. It causes the energy deposition to rise with falling velocity. If the velocity is small enough electrons from the target material are picked up and the effective charge z_{eff} decreases, reducing the energy deposition. This behaviour leads to the inverted depth dose profile for ^{12}C ions shown in fig. 2.1. Close to the surface the energy deposition is small and almost

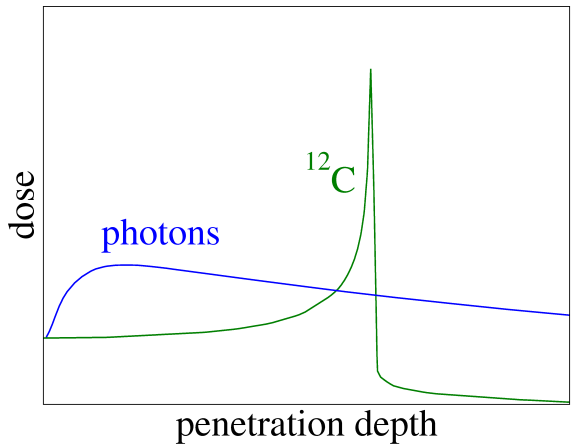

Figure 2.1:
Schematic drawing of the depth dose distribution for a photon and a ^{12}C ion beam. The dose maximum for photons is located shortly below the surface, whereas in the ion case the maximum dose is deposited at the end of the track. The photon dose decreases exponentially, while the ion dose has a sharp cut-off right after the maximum. The additional tail in the ion case is caused by nuclear reaction products (fragments) with longer ranges.

constant (plateau region). As the velocity becomes smaller the energy deposition rises and reaches a maximum when the electron collection starts (Bragg peak). Finally the decreasing z_{eff} causes a sharp drop of the dose and soon the ion is completely stopped. The mean range of the particle

$$S(T_0) = \int_0^{T_0} \left(\frac{dE}{dx}\right)^{-1} dE \tag{2.5}$$

and thus the position of the Bragg peak is (for the same target material) depending on the initial particle energy T_0. For a known target material, the particle energy can be adjusted to shift the Bragg peak in depth. The peaked depth dose distribution leads to an enhanced dose deposition in a short range right at the end of the ion track. Irradiating a larger area orthogonal to the beam yields a slice of the

same particle range with a finite thickness. According to eq. (2.4) and (2.5), the range of the particles scales with $\frac{1}{\rho_{target}}$. Particles crossing a material with double the density will therefore only have half the range. In a mixed density target (e. g. the body with its different organs, bony structures etc.) the slice of constant particle energy, iso energy slice (IES), will not be flat anymore. But normalised to the density of water, a planar slice of the same water-equivalent (WE) particle range is obtained, simplifying treatment planning (cf. chapter 2.4.4).
The width of the Bragg peak results from the stochastic nature of multiple scattering processes causing an approximately Gaussian range distribution [Leo94]. The observed Bragg peak is the sum of the depth dose distributions of many single particles. Folding a very sharp single particle dose with the Gaussian range distribution leads to the wide Bragg peak. The width of the range distribution scales with the travelled distance dx. Lower particle energies correspond to a shorter range, less scattering and consequently sharper Bragg peaks. The same is true for the particle mass. Heavier particles produce sharper Bragg peaks than lighter ones.
The elastic Coulomb scattering processes from target nuclei are individually governed by Rutherford's Scattering formula

$$\frac{d\sigma}{d\Omega} = z_{eff}^2 Z^2 r_e^2 \frac{(m_e c/\beta p)^2}{4\sin^4(\Theta/2)} \tag{2.6}$$

The $\frac{1}{\sin^4(\Theta/2)}$ dependence causes negligibly small angle deflections to dominate. Nevertheless, many events in multiple scattering processes accumulate to a noticeable deflection from the initial beam direction. For small angles ($\Theta \lesssim 30°$) Molière's theory [Mol48] is valid. The angular distribution can be approximated by a Gaussian distribution with a width of [Hag02]

$$\sigma_0 = \frac{13.6\text{MeV}}{\beta c p} z_{eff} \sqrt{\frac{d}{X_{rad}}} \left[1 + 0.038 \ln\left(\frac{d}{X_{rad}}\right)\right] \tag{2.7}$$

with the momentum p, velocity βc and charge z of the projectile, as well as the thickness d and radiation length[3] X_{rad} of the target material. As a consequence of the lower momentum, protons are laterally much more deflected than ions. A comparison between photons, protons and ^{12}C ions is shown in fig. 2.2.
Additional interaction processes like nuclear reactions and bremsstrahlung do not play a significant role for the energy loss of ions. Nuclear reactions, however cause fragmentation of the ions. This process leads to a loss of primary ions and, at the same time, to a contamination with lighter fragments of different mass, charge and energy. Due to geometrical considerations, peripheral collision are by far more

[3]The radiation length of a target material is defined as the distance over which the energy of electrons is reduced by a factor 1/e considering radiation loss only. This parameter is used as a scale length for describing high-energy electromagnetic cascades.

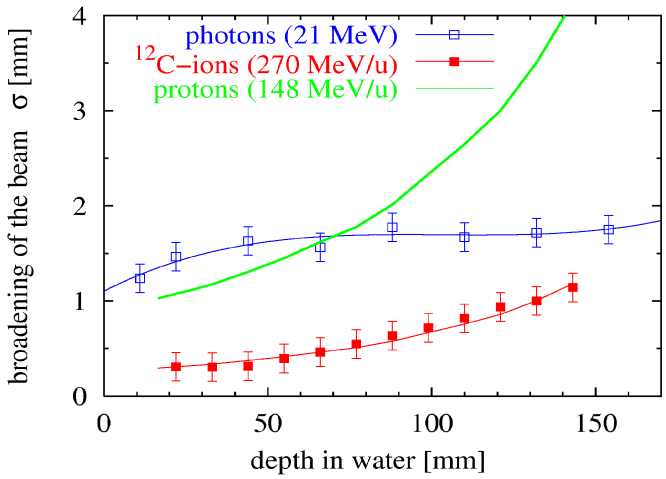

Figure 2.2:
Comparison of the lateral beam broadening for photons, protons and ^{12}C ions as a function of the water-equivalent penetration depth [Web96]. Over the first 150 mm carbon ions experience the lowest amount of lateral deflection.

frequent than central ones [Kra00]. As a consequence, the most of the fragments remain large and continue their way with almost the same velocity.
For different particles of the same energy the range scales like

$$R \sim \frac{A}{Z^2} \tag{2.8}$$

The frequently produced carbon isotopes ^{10}C and ^{11}C, for instance, have a similar range as the primary ^{12}C ions (R(^{11}C)=$\frac{11}{12}$R(^{12}C)). The contamination of the primary beam with these β^+ decaying isotopes is the physical basis for the unique possibility of online treatment verification in heavy ion therapy with PET (cf. chapter 2.4.3).
Fig. 2.3 illustrates how the final depth dose distribution of heavy ions is made up. The wide depth dose distribution of the mixed fragment field is added to the sharp Bragg curve of the primary ^{12}C ions. The resulting dose tail is responsible for a small dose contribution at $x > R(^{12}C)$.

2.2 Conventional Radiotherapy

In clinical practice, the standard method of radiation therapy is the irradiation with photon beams. The generally rectangular field of irradiation is shaped with collimators to match the maximum tumour extension. The 3D dose distribution is conditioned by the depth dose distribution. Due to dose build-up effects in the

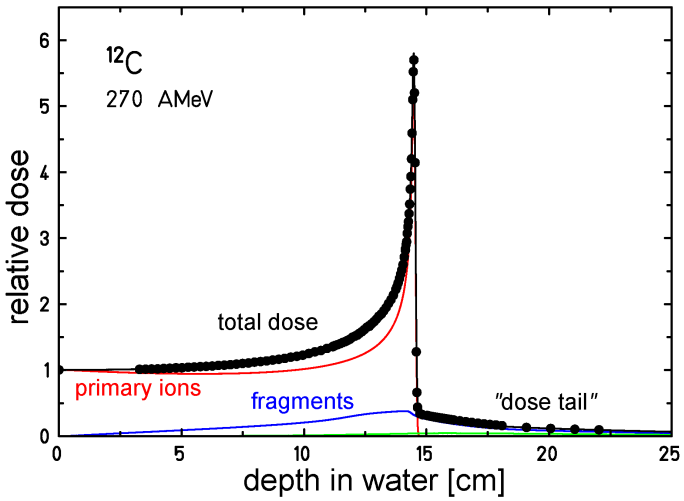

Figure 2.3:
Composition of the ^{12}C depth dose profile. The wide dose distribution from the mixed fragment field is added to the sharp Bragg curve of the primary ^{12}C ions. The distal dose cut-off is destroyed and after a steep fall-off a small fraction of dose is deposited deeper than the range of the ^{12}C ions. (The green curve represents the contribution of second generation fragments.) (taken from [Sih98])

entrance channel, the skin of the patient is spared. The dose deposition of high energetic photons increases over the first few cm in tissue, reaches a maximum, which is determined by the photon energy, and declines exponentially for larger depths. Consequently, the irradiation of deep seated tumours with photons requires more dose to be deposited outside of the target volume than inside. In conventional photon therapy, the dose contribution to the normal tissue is locally minimised by superimposing many beams from different directions. Crossing each other in the tumour volume, every beam contributes only with a fraction of the prescribed dose, reducing the dose deposition in the proximal tissue.
Modern photon therapy techniques include intensity modulation across the irradiation field. The single field is divided into several small sub-fields which are irradiated independently of each other, allowing position dependent variations of the photon intensity [Bor94]. State-of-the-art is field shaping by means of computer-controlled multileaf collimators[e. g. Con92], first proposed by [Bra88]. For a summary on the techniques of intensity modulated radiation therapy (IMRT) refer to [Web93]. IMRT achieves a good conformity between dose and target volume but based on photon irradiation more integral dose is deposited outside the target volume than inside.
The current standards for photon therapy provide a 3D dose homogeneity of $+8/-5\,\%$ of the reference dose, 1 cm penumbra (from 80 to 20 %) and an exposure of the

normal tissue in the irradiation field of approximately 70 % of the reference dose [Pöt98a].

2.3 Biological Effects of Charged Particles

Compared to photons, heavy charged particles show an increased effect on biological target material which depends on the local ionisation density [e. g. Sch94, Sch97]. For light ions the linear energy transfer (LET) in the plateau region is small and the track diameter is large, resulting in a low ionisation density. Only in the peak region, where LET is high and the track diameter small, the ionisation density is high. This leads to an increased biological effect.
The main aim of a radiation therapy, namely killing the malignant tumour cells, is achieved by destroying the genetic code (DNA), so that the tumour is not growing and the tumour cells can be eliminated in different biological path ways. Being a double strand with complementary information the DNA is most effectively damaged by an accumulation of double strand breaks[4]. The probability for such an event rises with the ionisation density. In the case of sparsely ionising radiation, the strands are only occasionally damaged and the impacts are located too far apart to really separate the fragments. Most of the time, the repair system will be able to restore the state of the DNA. In the case of densely ionising radiation the DNA will be fragmented into small pieces leaving the cell no chance for repair. Apart from the ionisation density, the cell damage depends on many different factors, like cell species dose level etc.
To express this difference the relative biological effectiveness (RBE) is defined as the quotient of photon to particle dose leading to the same biological effect

$$\mathrm{RBE} = \frac{\mathrm{D}_{\mathrm{photon}}}{\mathrm{D}_{\mathrm{particle}}} \tag{2.9}$$

For light ions large differences in RBE enhance the biological effect of the physical dose in the peak region compared to the plateau. Therefore, the biological damage to the target volume can be increased, while the effect on the tissue in the entrance channel remains almost the same (see fig. 2.4). In practice, a lower physical dose is required to yield the same biological effect inside the target volume. Consequently, the healthy tissue in the entrance channel is better spared.
Being closely related to the ionisation density, the RBE varies not only along the ion path, but also for different initial energies, fragment distributions etc. Each of the fragments, for instance, deposits dose with a different RBE. The effect of the

[4]Damage of both strands where the impact sites are located close to each other. Accumulation of double strand breaks yields small areas of high local damage (clustered lesion) where the genetic code is completely lost.

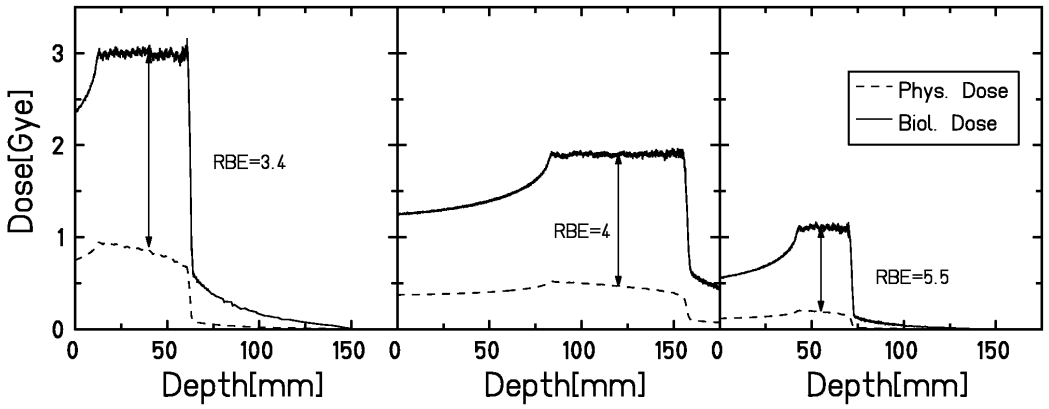

Figure 2.4:
Comparison of biological effective and physical absorbed dose. Shown are the depth dose profiles for different chordoma patients with different prescribed biologically effective dose levels. In the target region, the almost flat physical dose distribution is enhanced by a large RBE. (taken from [Krä00])

complex fragment distribution on the applied dose has been carefully studied and included into the treatment planning and dose optimisation.

2.4 Heavy Ion Therapy

8All the physical and biological properties of heavy charged particles are useful for precision irradiation of tumours. The sharp, high Bragg peak, the steep distal dose fall-off and the small amount of lateral scattering of heavy ions are ideal prerequisites for a high, 3D spatial resolution in dose deposition, allowing the dose distribution to be matched very precisely to complexly shaped tumours. The unavoidable dose deposition in the normal tissue is much lower than in conventional therapy. Due to the increased biological effectiveness in the tumour region, the overall dose level is much lower in heavy ion therapy than in photon or proton therapy. In summary, the tumour can be heavily damaged while the surrounding structures and tissue is maximally spared. ^{12}C ions, as used for the pilot study on heavy ion cancer therapy at GSI, provide an optimum in RBE, geometrical beam properties and fragmentation.

2.4.1 Beam Delivery

In general, tumours are large compared to the dimensions of a particle beam and the beam has to be spread over the whole target volume in longitudinal and lateral

direction. For charged particles an extended depth dose distribution (so called spread-out Bragg peak, SOBP) is generated by overlaying Bragg peaks of different energy. As shown in fig. 2.5 the peaks have to be stacked close enough to yield a smooth envelope and the pre-irradiation in the plateau region requires the proximal peaks to be scaled in intensity.

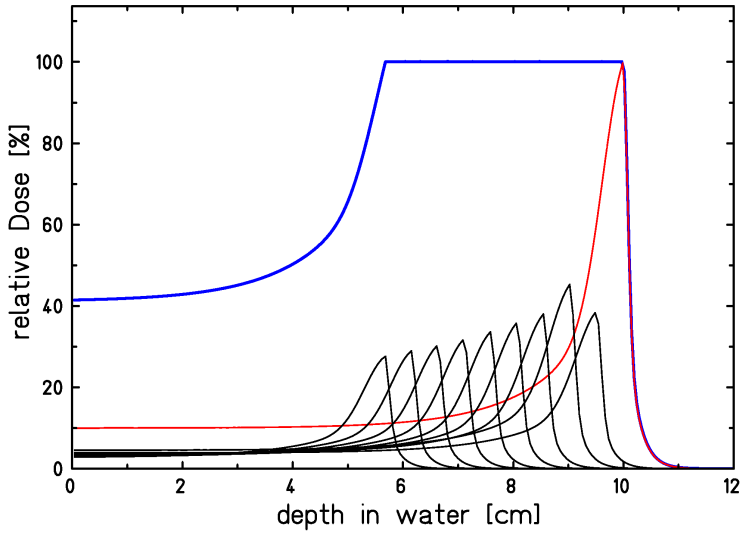

Figure 2.5:
Illustration on how to irradiate an extended target volume by adding many single Bragg peaks with different particle energies. The Bragg peaks are positioned close enough to yield a smooth envelope. The pre-irradiation of the proximal slices by the plateau contribution leads to a declining intensity for lower depths.

Two fundamental beam shaping methods exist, passive and active beam shaping. Combinations of both (semi-active methods) are used in therapy, as well. Historically, passive methods have been used first. But modern active methods largely improve the volume conformity.

Passive Methods

Passive beam shaping relies on scattering and energy loss in interposed absorber material. For lateral spreading sophisticated scatterers are used to form a uniform, extended field [e. g. Chu93]. Once the beam's lateral extension is large enough to cover the maximum cross-section of the target volume, it has to be spread longitudinally.
Historically, charged particle therapy was started at physics research centres, since those could provide the required accelerators. These machines were originally designed to serve the needs of physical experiments and typically did not offer a fast

energy variation. When using such accelerators for therapeutic purposes, complexly shaped absorbers, e. g. ripple filters, are used for range modulation. The resulting SOBP is shifted to the required depth by using flat range shifters of variable thickness. Patient specific collimators and compensators shape the SOBP as closely to the target volume as possible. Nowadays, the fixed collimators are substituted by computer controlled, dynamic multi-leaf collimators (MLC) so that the lateral dimensions can be adapted to the target cross-section at the actual depth.

The principle of passive beam delivery is schematically summarised in fig. 2.6. Passive beam delivery does not require changes of the particle energy during the irradiation. In addition, fluctuations in beam intensity in time do not affect the homogeneity of the applied dose distribution. However, the volume conformity is limited and parts of the beam delivery system, like compensators, have to be manufactured for each patient.

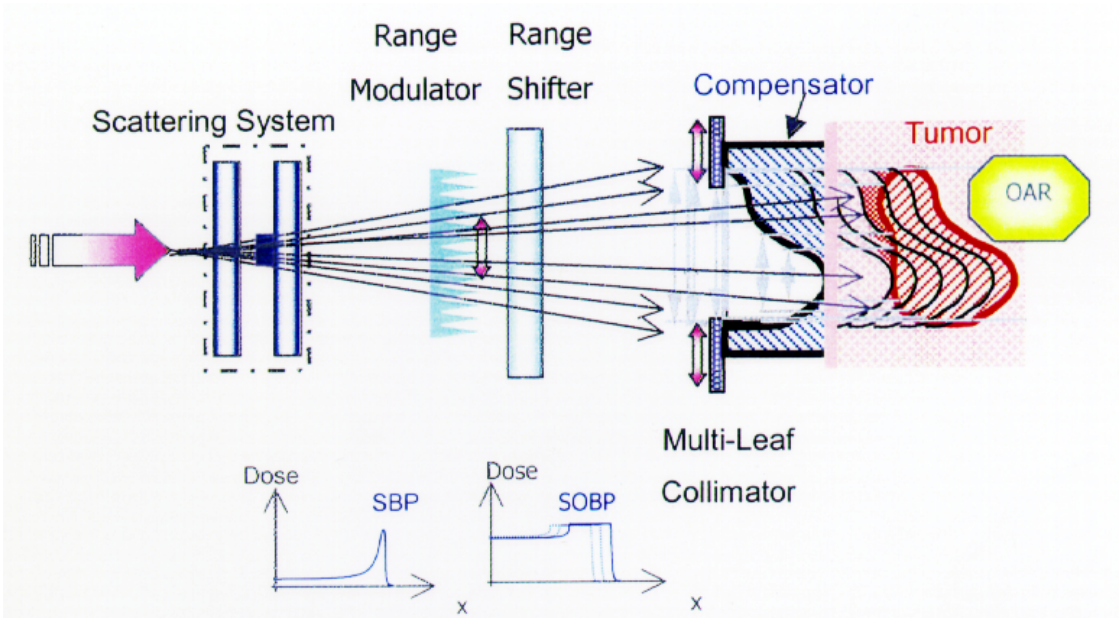

Figure 2.6:
Schematic representation of a purely passive spreading system. A set of sophisticated scatterers generates a flat transverse dose distribution over a large field. Starting with a single Bragg peak (SBP) a ripple filter (in combination with a flat energy degrader as range shifter) produces the SOBP with correct intensity for each depth. A special compensator conforms the distal surface of the radiation field with the distal surface of the target. (taken from [Reg02])

Active Methods – Intensity Controlled Magnetic Raster Scanning

Passive beam shaping systems are due to the limited flexibility not able to produce really conformal target volumes. In addition, a large fraction of the beam intensity is lost by the collimation of the scattered beam. Therefore, active strategies have been developed, as for instance proton spot scanning at PSI [Bla90, Ped95] or intensity controlled magnetic raster scanning at GSI [Hab93], avoiding all passive beam shaping devices in the path of the beam.

For active, intensity controlled particle therapy the target volume is divided into virtual slices of equal particle energy which are treated sequentially. For the heavy ion therapy at GSI the energy variation required to switch between the slices is achieved by a synchrotron providing a pulsed beam with a cycle time of $\approx 5\,\mathrm{s}$. After each pulse of extracted particles (spill) the synchrotron is refilled and the ions in the ring are accelerated to the next required energy.

In the lateral direction the beam is spread by a fast, magnetic deflection system. As shown in fig. 2.7, the plane of each IES is subdivided into single picture elements (pixels). These are irradiated on a point-to-point basis with a pencil-like ion beam being magnetically deflected to the corresponding coordinates, so called

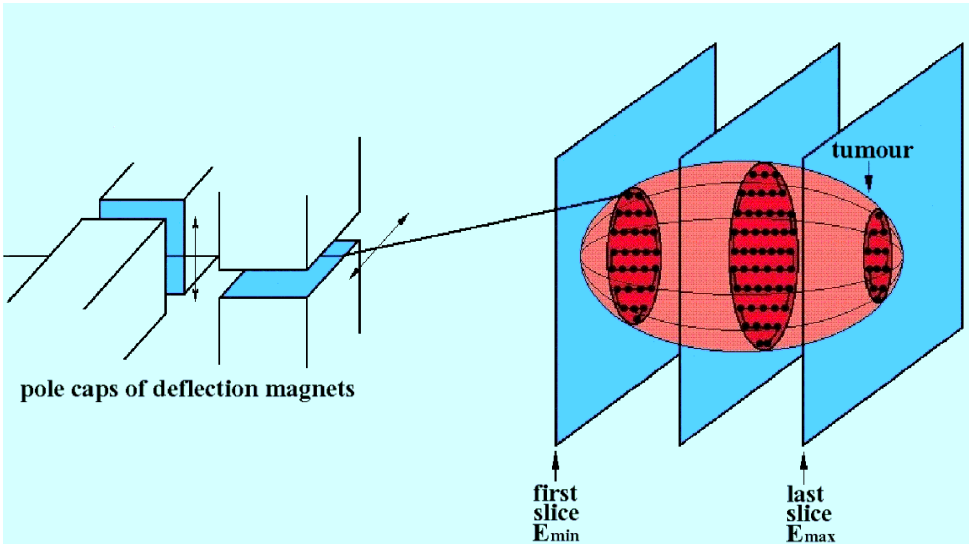

Figure 2.7:
Principle of intensity controlled magnetic raster scanning. The tumour is divided into slices of the same particle energy, each of those again being subdivided into single points. A thin pencil beam is scanned on a point-to-point basis over the slices, resting long enough at each point to deposit a pre-defined number of particles. In order to move to the next slice the beam is switched off and the corresponding energy is requested from the accelerator for the next pulse.

raster points. The size of the maximum scanning field is $200 \times 200\,\mathrm{mm}$. The scanning speed is intensity controlled, leaving the beam at each position as long as necessary to apply a pre-defined number of particles. In order to get a smooth dose distribution even with minor fluctuations in the beam quality, the distance between two neighbouring raster points was optimised to approximately $\frac{1}{3}$ of the beam's FWHM [Hab93] (typically $\approx 2\,\mathrm{mm}$). Variations in beam intensity and position are registered by a monitor system, consisting of two multiwire proportional chambers (MWPC) for position verification and three ionisation chambers (IC) for beam intensity measurement in front of the patient. The position verification is repeated every $150\,\mu\mathrm{s}$ while the beam intensity is measured every $12.5\,\mu\mathrm{s}$. For cases in which the measured beam position differs from the expected one, a feedback loop to the scanner magnets for fast position correction is implemented in the scanning control system.
Modern computing technology allows to store the settings for all accelerator and transfer line elements of 252 different particle energies, 7 different beam spots sizes and 15 intensity levels in a large database. At GSI, these settings can be switched on a spill-to-spill basis enabling a fast energy variation without any absorbing material. Instead of longitudinally spreading the Bragg peak, the IES slices are irradiated one after the other.

The Scanning Control Unit

The complex, intensity controlled scanning process requires a real-time control and safety system. The VME-based scanning control unit (SCU) at GSI consists of three main components: a fast, autonomously running treatment sequencer, a slow control unit and a user interface. The slow control unit manages the data transfer to the frontend hardware and monitors the equipment parameters and the interlock unit [Deb98]. During the irradiation, all time critical processes run on the treatment sequencer. It consists of seven dedicated control modules (SAM[5]), which are responsible for beam measurements, beam request, beam positioning, data logging, interlock management etc. The distribution of the tasks on the single modules is summarised in table 2.1. Each of these modules consists of a digital signal processor (DSP), a shared memory block (SMB) and two device bus ports (GTB) providing data connection to the frontend electronics. In order to synchronise the tasks and share the data during irradiation, the SAM modules are interlinked with DSP-links, the so called synchronisation bus. Via this bus SAM I1 sends the relevant data for each of the raster points to the other modules and they report their data back. Apart from the synchronisation bus, the only connections which remain open during the irradiation are those from SAM D to the online data memory and the GTB connections to the electronics. The system control processor receives

[5]abbreviation for Steuerungs- und Auslesemodul

module	tasks during irradiation
SAM P	requests different accelerator parameters according to the specifications in the treatment plan
SAM D	transfers the data from all other SAMs to the online data memory
SAM I1	measures the number of ions every 12.5 μs and decides when to proceed to the next point
SAM I2	redundant to SAM I1
SAM O1	measures and verifies the beam position every 150 μs, if necessary a fast feedback loop with SAM S realigns the beam
SAM O2	redundant to SAM O1
SAM S	sets the power supplies for the scanning magnets, according to the planned position of the next raster point in the treatment plan and the result of the position verification measurement

Table 2.1: Distribution of tasks in the scanning control unit during irradiation.

information about the status of the irradiation via the interlock unit, the online data memory and the position counter. This data is displayed in real-time on the therapy control panel and the therapy online monitor (TOM). In case of failure the interlock unit interrupts the treatment within 200 μs.
At the beginning of the irradiation, the software for the SAM modules (stand-alone programs without operating system), as well as all the parameters for every single raster point, i. e. the tables with the x/y positions for the deflection magnets, the table with the specifications for the accelerator parameters, the tables with the numbers of particles and the tolerated deviations for all online measurements are loaded into memory. This data determines the sequence of the irradiation process which is automatically controlled by the SAM modules according to online measured monitor signals. For safety reasons, no manipulation of the data in memory is possible, once the irradiation has been started.

2.4.2 Patient Positioning

Heavy ion therapy gains its spatial precision from a controlled particle deposition to small volume elements on a point-to-point basis. In the treatment planning process the position of each of the voxels is optimised with respect to the patient based medical imaging data. Every deviation between actual and expected target position leads to errors in dose painting and reduces the conformity. Consequently, at the beginning of each treatment session the patient has to be positioned exactly as in the preparation session, when the medical images for treatment planning were taken. The accurate positioning is ensured by a sophisticated patient setup procedure. From the 3D computer tomography (CT) data, used for treatment planning, planar projections, so called digitally reconstructed radiographs (DRR),

are calculated. In the treatment room, the patient is positioned as good as possible using a calibrated laser setup as reference. Next, at least two orthogonal verification x-ray images are taken and each of these is compared to the corresponding DRR. If the x-ray images match the DRRs, the patient is positioned correctly. Otherwise, he/she has to be re-positioned and the procedure starts again. With this method the patient based coordinates are transferred into the room-based frame of the scanning system with an accuracy of better than 1 mm [Har93].
Once the patient is set up correctly, the position has to be kept absolutely stable during the whole treatment session. At GSI, patient immobilisation is achieved by means of stereotactic fixation [Sch93b]. For head patients a tight mask from self-hardening thermoplastic bandages is made in the preparation phase. Being

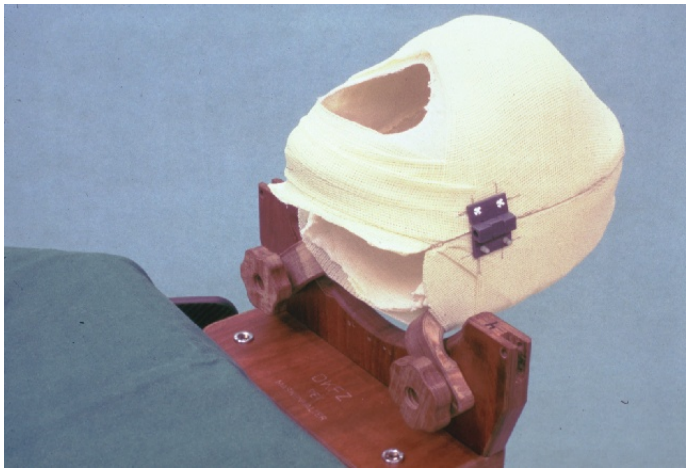

Figure 2.8: Patient head mask for stereotactic fixation

screwed to the patient couch (see fig. 2.8), this mask holds the bony structures of the skull and the enclosed tissue very reliably in position. The same strategy can be successfully applied to all indications where the tumour does not move relative to the surrounding bony structures, e. g. tumours in the head, neck, pelvic region or close to the spinal cord. Because the final dose distribution of heavy ion therapy is built up from single points with optimised particle deposition, it is currently not feasible for any indication where the single volume elements are subject to intra-fractional motion. In general, the possible deviations in target position have to be smaller than the precision of the irradiation process.

2.4.3 Treatment Verification – PET

Although the fragmentation processes tend to deteriorate the sharp beam contours by enhancing longitudinal and lateral scattering [Kra00], they offer the unique feature of in vivo treatment verification. Among the produced fragments is a large

number of lighter carbon isotopes, mainly ^{11}C and ^{10}C, from beam- and ^{15}O from target-fragmentation. All of these are β^+ emitters with a relatively short lifetime of 20.38 min, 19.3 s and 2.03 min, respectively. Because the lifetime of these isotopes is much longer than the drift time trough the body, they decay under emission of positrons at the end of their range. After decay, the emitted positrons will travel a short distance in the tissue before annihilating with target electrons into two oppositely directed 511 keV photons. These photons can be measured coincidently by a dedicated positron emission tomograph (PET) [Eng99]. For more details on PET imaging see appendix C. Since ^{11}C and ^{10}C have, according to eq. (2.8), almost the same range as ^{12}C, the reconstructed signal provides fundamental information about where the primary beam was stopped inside the patient.

2.4.4 Treatment Planning

Although different physical processes have to be included, treatment planning for heavy ion therapy is based on the same patient specific data sets as for conventional photon therapy. The tumour tissue is identified using computed tomography (CT) images with contrast agent. T_1 and T_2 weighted magnetic resonance images (MRI) with contrast agent improve the definition of organs at risk [Jäk01]. In each slice of the CT data set the target to be irradiated and the critical structures to be spared are delineated manually. The therapeutic dose to the target volume as well as potential dose limits for the critical structures are specified and according to the orientation of the marked structures suitable incidental angles are chosen for the irradiation fields. In order to define the energy range, the CT data is converted into a WE image [Kra00]. Exact information on the electron density distribution, which directly determines the penetration depth of the particles, is gained from CT scans without contrast agent, since the enhanced contrast would misrepresent the conversion into water-equivalent path length (WEL).
Active beam shaping methods provide an enormous amount of degrees of freedom. Therefore the treatment parameters are adjusted by "inverse planning". For each of the up to tens of thousand beam spots the energy, position, number of particles etc. have to be set in a way to yield the prescribed 3D dose distribution. Starting with the most distal iso energy slice, the scanner positions and number of particles per voxel are automatically optimised by the treatment planning software *TRiP98* [Krä01], taking into account that all voxels but those in the most distal slice can receive a certain pre-irradiation from the plateau contributions of the distal Bragg curves. The dose calculation algorithm is described in more detail in chapter 4.1.1. The required one-dimensional energy loss distribution is calculated via the YIELD ion transport model [Hab93]. This physical beam model is based on experimental data and covers the ion interaction with tissue, calculating the distribution of primary, as well as secondary ions and their energies as a function of depth. The optimised raster data file (rst-file) includes all the relevant parameters for each of

the scanner positions (energy, focus, beam intensity, x/y coordinates and number of ions) and is the basis for the automatically generated process data file. For the final assessment the dose distribution can be calculated on the CT-grid, accumulating the contributions from each of the beams on the single raster grid positions to every CT-voxel. In addition, the read-outs of detectors with non-linear response functions (like x-ray films) can be calculated.
For physical experiments the optimisation and calculation of the absorbed (physical) dose is sufficient but for biological experiments as well as for the treatment of tumours the different biological effects due to variations in RBE have to be taken into account. The later dose is referred to as *biological dose*, but beyond the scope of this thesis.

Chapter 3

Target Motion in Cancer Therapy

The main aim of any radiation therapy is the deposition of a lethal dose to all tumour cells with a minimum contribution to the surrounding, normal tissue. In accordance with the basic principles of radiation protection and the medical needs of the patient, the amount of dispensable dose to the normal tissue has to be kept as low as technically achievable. In this context much effort has been put into the further development of volume conformal radiation therapy methods, i. e. those which match the applied dose distribution best to the contours of the tumour.

No matter how precisely the geometry of the target can be approximated, some safety aspects, like the accuracy of patient positioning and beam delivery, or target displacement and deformation during therapy, have to be considered, leading to an unavoidable extension of the treated volume into normal tissue. The corresponding concepts are shortly summarised in appendix A.1. The volume which provides the basis for treatment planning is called planning target volume (PTV). The PTV consists of the visible tumour volume (gross tumour volume, GTV), a margin for non-visible, latent tumour spread (clinical tumour volume, CTV) and an additional margin accounting for all geometrical and planning uncertainties.

In the treatment planning process all therapy-relevant parameters have to be optimised in such a way that the PTV is sufficiently covered with the prescribed dose. To avoid collateral damage to neighbouring structures, the PTV should contain no more normal tissue than absolutely necessary. On the other hand, it has to be large enough to guarantee that all parts of the clinical target volume receive the full, prescribed dose. In case of tissue motion in the irradiation field a strong conflict exists between the conformity of the treatment and organ motion which can move tumour tissue out of the treatment field and normal tissue in. For a static irradiation field any change in position and form of the target volume during the treatment requires an extension of safety margins, such that all possible target positions are covered. Especially close to the borders of the field, where the dose gradients are steep, areas can exist, which contain target tissue for short time intervals only. These areas do not receive the full therapeutic dose and might be a germ for relapse. For an irradiation with a pencil beam the situation is even more complex because target motion produces inhomogeneities not only at the borderline but also inside the treatment

field. In this case, margin extension is not sufficient to guarantee a homogeneous dose deposition.

3.1 Types of Target Motion

Target motion is one of the key issues which has to be considered when planning a patient treatment. Obviously, if the patient moves the body, the position of the target volume relative to the room's frame of reference is altered. This external motion can be limited very precisely using immobilisation devices like stereotactic frames, bite-blocks, thermoplastic head masks, foam beds etc. Applying stereotactic fixation, room-based treatment parameters can be applied to irradiate a target volume defined in patient-based coordinates. Purely internal motion, on the other hand cannot be restricted by fixation techniques. Although being as important as precise patient positioning, up to now, no standardised strategy exists to deal with internal motion in precision radiation therapy.
In general, target motion occurs on two different time-scales, within minutes or seconds during a single treatment session (intrafractional) and from fraction of hours to days between different sessions (interfractional). Latent interfractional target motion can be accounted for by verifying that the target is in the planned position right before the irradiation. Intrafractional target motion, on the other hand, is fast compared to the irradiation time. It has either to be restricted by suitable means (e. g. external fixation) or included into the irradiation process.
According to [Oku95] organ motion can have one or more of the following sources. In some cases, the motion will be a superposition of several components of different impact and time scale (e. g. lung: respiration-related and vascular pulsation).

gravity or position-related Depending on the position of the patient, contour and location of the organs vary. In general, the significance of these variations increases from skull to abdomen [Lan01]. The body surface does not necessarily reflect the position-related organ motion but it can be accounted for by positioning the patient under exactly the same conditions in the treatment sessions as during the planning scans. For a properly immobilised patient, no further position-related target motion should occur during the treatment session.

pressure-related Due to differences in filling, the bladder as well as the gut significantly change their size and shape. The surrounding organs are directly affected by these deformations. Therefore, pressure-related motion can be found for almost all organs in the pelvic region. This is an extremely latent type of organ motion and can currently only be controlled by following dedicated protocols for bladder and gut filling prior to each treatment session.

gut movements In addition to the latent, filling dependent deformations, the digestion process rapidly alters the gut's position and shape. These displacements occur arbitrarily, since the gut is a very mobile organ. Due to their speed and unpredictability they are not easy to account for.

vascular pulsation The vascular pulsation itself is too small to cause significant target motion [Oku95]. For treatment planning only the pulsation of the heart has to be considered. Due to the high frequency (approximately 60-80 beats per minute) and the superposition with the respiration it is extremely hard to be compensated.

respiration-related In the thorax and abdomen (lung, liver, kidney, pancreas, diaphragm etc.), breathing has the largest influence on the target position. Therefore, dealing with respiration-related target motion is of major importance in radiation therapy. Although the respiration-related target motion strongly depends on anatomical site and breathing pattern of the individual patient, it is in general periodical, slow (approximately 10-15 cycles per minute) and quite regular. Consequently, it is well suited for online compensation methods and will be the basis for all target motion considerations in this thesis.

3.2 Parameters of Respiration-Related Target Motion

Respiration is the most regular and periodic source of target motion in the patient's body. In the human trunk, the largest contribution to organ motion is breathing-related. Multiple studies on the pattern of respiration and the resulting displacements of tumours are carried out all over the world. A detailed summary of organ motion data can be found in [Lan01]. Although the precise parameters vary significantly depending on the specific patient and tumour location, some general remarks can be made.

The magnitude of motion observed in lying patients is different for the 3 body specific directions (see appendix A.2 for the definition). The largest amplitude occurs in superoinferior (s.i.) direction. For the diaphragm, values up to 30 mm peak-to-peak (free, quiet respiration) are found in literature [e. g. Dav94, Han99]. For the two orthogonal directions anteroposterior (a.p.) and right-left (r.l.) the motion is much smaller [Kor92]. Displacements up to 8-10 mm peak-to-peak are reported for these directions [e. g. Kub96, Ros90].

In case of the upper-abdominal structures, the motion is predominantly translational and does not exhibit any significant dilation [Kor92]. However, translational motion causes the tumour to move in and out of the observation level. This be-

haviour can lead to an apparent change in size and shape. Moreover, due to partial volume effects, a pure target translation can alter the measured density distribution in the CT, since the resulting Hounsfield units (HU) represent the average signal over the corresponding voxel. Both effects have to be carefully considered when analysing dynamic patient-data.
The relative displacement of organs and anatomical structures inside the body generates shifts in the radiological path length for single voxels. The radiological path length corresponds to the water-equivalent (WE) depth of the voxel parallel to the particle path. According to eq. (2.4) and (2.5) it is proportional to the integral of the inverse density distribution the particle has to traverse. In some cases, respiration-related target motion changes the path length significantly. For relaxed breathing, the average lung density varies by up to 80 CT numbers, corresponding to approximately 8% of the density of water [Hen82]. In a more recent study, *Minohara et al.* found respiration-related variations in WE path length (WEL) in the abdominal region of up to 18.9 mm in p.a. direction [Min02].
Target rotation might occur at the periphery of the lung or at the diaphragm, where the corresponding organ significantly changes its form. In general, target rotation is expected to be small. Up to now, very limited data is available on the rotation of tumours due to respiration. For the theoretical investigations in this thesis, the expected rotation of a tumour, attached to the wall of the lung, was estimated with a very coarse model: If the lung is approximated by a semi-ellipsoid with variable volume, the tangent plane at each point of the surface determines the orientation of a potential target volume attached to the lung at that point. A statistical analysis of the differences in orientation between exhalation and inhalation revealed that $\pm 5^\circ$ is a reasonable value for respiration-induced target rotation close to the lung (refer to appendix B for more details). It has to be emphasised, that this model is very coarse and does not reflect the anatomy of the lung. Nonetheless, the results agree with first patient studies involving time-resolved CT, which in general do not reveal any significant respiration-related rotations in the lung within the precision of current imaging methods [Rie].
The respiration-related motion parameters presented in this section are empirically determined in clinical trials. These values vary significantly from patient to patient, depend on the patient's condition, position etc. They only serve as a guideline for the theoretical study of motion-related effect on the dose application. In clinical practice, the detailed motion pattern will have to be studied for each patient separately.

3.3 Tracking of Target Motion

The analysis of patient-specific motion patterns as well as the inclusion of target motion into the irradiation process require precise and time-resolved information

on the position, shape and density of internal structures. The issue of looking inside the human body dates back about 2000 years. For the first 1900 years all anatomical knowledge was gained from the dissection of corpuses. Prior to the discovery of x-rays by Wilhelm Conrad Roentgen in 1895 a non-invasive imaging of the interior of a body was considered to be impossible. Approximately since 1970, methods for 3D imaging of a human body exist. Nowadays, a lot of medical-related fields routinely gain information from inside the body with different methods, and the development of new strategies is still in progress. The potential applications range from diagnostics and morphology to radiosurgery and particle therapy; some need a high resolution, some are time-critical etc. Each method has its advantages and restrictions. Therefore, the choice of method will always be a compromise and the selection of the means according to the present situation requires a skilled and experienced physician.
All existing methods for managing target motion in radiation therapy (cf. chapter 3.4) are based on precise, time-resolved knowledge of the target motion either included in treatment planning or beam delivery. To include target motion in beam delivery, the tumour position has to be tracked and analysed in real-time. The existing real-time tracking approaches for respiration-related target motion can be grouped into two categories: direct and indirect methods. In direct motion tracking approaches, the target itself is monitored using appropriate probes. From the displacement of prominent structures close to or inside of the target volume, all relevant motion information can be extracted. On the other hand, in the case of a periodically motion pattern, the same information can be gained indirectly, by monitoring a property which is directly related to the source of the motion (e. g. the external motion of the breast driven by the respiration-related motion of the lung). Without being exhaustive, the following section provides an overview on different methods for tracking target displacement and their impact on heavy ion therapy. A short review on the technical principles of the most common medical imaging methods is given in appendix C.

3.3.1 Direct Motion Measurements

Ionising Imaging Methods

The field of medical imaging with ionising radiation covers of two main categories: x-ray and nuclear medicine. In x-ray diagnostics, electromagnetic radiation is passed through the body and the measured attenuation provides information on the density distribution along the path. In contrast, nuclear medical methods measure the distribution of radioactive decays inside the body, originating mostly from injected, radioactively marked substances. X-ray imaging includes radiography, fluoroscopy and computed tomography (CT). The field of nuclear medicine mainly

involves positron emission tomography (PET) and single photon emission computed tomography (SPECT).
Nowadays, radiography is a well known method in all medical fields. a focussed x-ray beam is passed through parts of the anatomy hitting an x-ray sensitive film placed on the distal site of the patient. The absorption pattern of the x-rays produces a static image of anatomical structures of different atomic density on the x-ray film. The film shows the integrated signal over the whole exposure time. Therefore, standard radiography is not suited at all for tracking of fast target motion.
In fluoroscopy, the absorption pattern behind the body is displayed on a fluorescent screen which can be monitored by a camera and viewed in a television screen [e. g. Bai80]. Nowadays, analogue camera and TV are replaced by image-intensifier camera systems (digital fluoroscopy) enabling digital image processing. Providing real-time imaging, fluoroscopy is especially suited for x-ray guided surgery or organ motion studies, but the monitoring time or frame rate is limited by the dose deposition. In photon therapy, the penetrating therapy beam can be used as imaging beam (portal imaging), eliminating the overhead in diagnostic dose to the patient. In analogy to radiography, fluoroscopy provides 2D projections, only. Therefore, at least two (orthogonal) imaging directions are necessary to gain 3D motion information.
CT is mandatory for treatment planning in particle therapy, revealing the electron density which determines the ion range. With modern CT techniques, time-resolved electron density distributions can be measured yielding planning data sets for different motion states [Rie03a, Rie03b]. CT could provide full 3D motion information including density distribution, but CT scanners are too bulky to be operated at the treatment site during the irradiation.
The main restriction for all ionising imaging methods in real-time motion tracking is the intrinsic dose deposition to the patient. In contrast to the therapeutic dose, the diagnostic contribution is not focussed on the target, only. If the information of the target vicinity is required as well (e. g. the WEL for the treatment planning), the field of view cannot be restricted to the target volume. Therefore, more normal tissue is affected, limiting the imaging frequency and observation time with ionising methods.

Non-Ionising Imaging Methods

Medical imaging without ionising radiation is mainly performed with magnetic resonance (MRI) and ultrasound (US) imaging. If applied during heavy ion treatment, the large, inhomogeneous magnetic fields of MRI will interfere with the delivery of charged particle beams and deflect the ions from their planned trajectories (cf. appendix C). Consequently, MRI is not feasible for online motion tracking in heavy ion therapy.

Modern 3D ultrasound techniques are fast enough for real-time imaging. As the absorption coefficient in biological tissue is proportional to the wavelength, the spatial resolution declines with the imaging depth (cf. appendix C). The destructive influence of air limits the feasibility of US imaging in the thorax. Depending on the direction of imaging only up to 60 % of the surface of the human lung can be imaged [Kle99]. For the same reason, the sonic head has to keep permanent contact with the patient's skin during imaging, causing the image frame to move in space according to the external motion. *Bouchet et al.* realised a real-time image guidance system for therapeutic procedures based on 3D ultrasound imaging and IR tracking of the sonic head [Bou01]. Correcting the orientation of the US image with the 3D position of the sonic head, they report an average tumour tracking accuracy of 0.2 mm, 0.9 mm and 0.6 mm in the AP, lateral and axial directions respectively.
For a limited number of indications ultrasound imaging might be feasible for real-time tracking of tumour motion. In any case the problem of attaching the sonic head to the patient has to be solved. Furthermore, it has to be verified that the breathing pattern does not change when the patient feels the contact with the sonic head. To avoid artefacts in the data set, the sonic head cannot be attached to the patient during CT. If used afterwards, the correlation between target motion and breathing cycle might be altered and the CT data sets required for treatment planning would be invalid.

Magnetic Position Tracking

Some non-ionising strategies have been developed which measure the target position via electromagnetic interaction with special markers attached to the tumour. The most promising attempt for radiotherapy is the TULOC (tumour location) system presented by Seiler et al. [Sei00]. A setup of 6 differential field generating coils is sequentially excited with a 12 kHz alternating current of 2 A. For each excited coil the induction voltage in tiny sensor coils (8 mm by 0.8 mm in diameter), endoscopically attached to the tumour, is measured. The setup is schematically shown in fig. 3.1. From the distribution of the induction voltages the position of the sensors can be calculated with a spatial accuracy of 1-2 mm (RMS) and an angular resolution of 0.5-1° (RMS) depending on the sensor orientation. Since one full excitation cycle lasts 20 ms the maximum repetition frequency of the position determination is 50 Hz. The setup was successfully combined with the proton spot scanning technique at PSI [Sei00]. With interchanged function of sensor and emitter coils, the latter being driven with a 7 kHz alternating current of 0.4 A, the magnetic field outside the body was reported to be smaller than $10^{-4}\,\frac{\mathrm{A}}{\mathrm{cm}}$ [Kir97], which is three orders of magnitude smaller than the magnetic flux of the earth[1] and about one order of magnitude below the limits for medical supply units in Germany

[1] at the equator about $3.1 \cdot 10^{-5}\,\mathrm{T}$

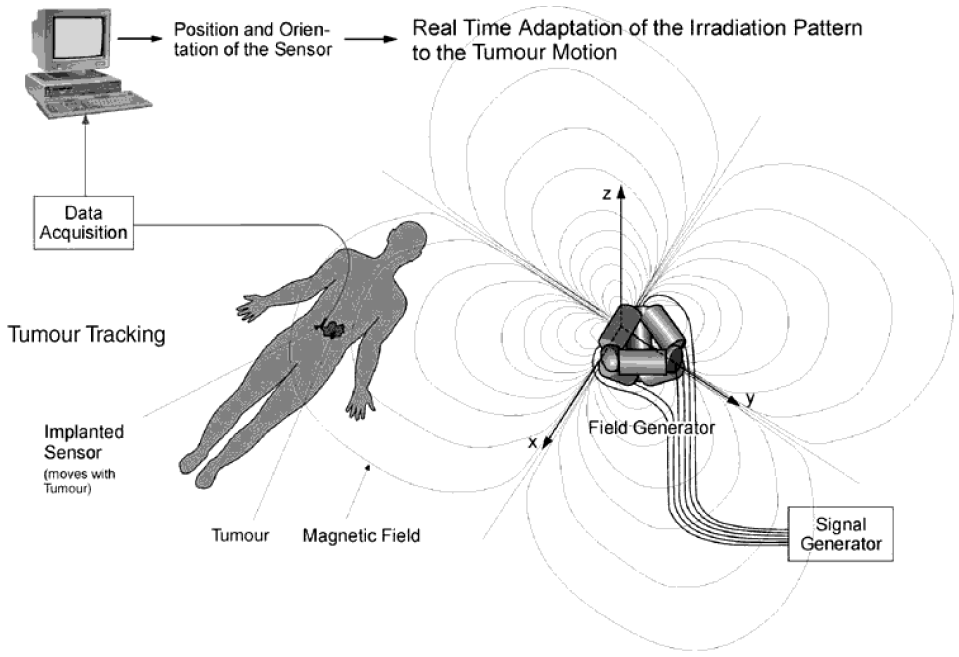

Figure 3.1:
Schematic drawing of the TULOC assembly. Tiny sensor coils are endoscopically attached to the tumour. The induction voltage into these coils is analysed to track their position within an external magnetic field. (taken from [Sei00])

[DIN97]. The influence of such a small magnetic flux on the therapeutic ion beam is absolutely negligible.

3.3.2 Indirect Motion Measurements

Regular respiratory motion can be measured indirectly determining the state within the breathing cycle. The correlation to the breathing cycle provides a measure for relative target motion. The corresponding absolute displacement information has to be determined in addition to the actual tracking process.
Kubo and Hill investigated three types of respiration sensors [Kub96]: temperature sensors to measure temperature differences of the air near the nostrils (room temperature when inhaling vs. lung temperature when exhaling), a belt-like strain gauge wrapped around the patient torso to monitor the motion of the chest and a pneumotachograph to integrate the volume of air passing through the airway. They concluded that either method is feasible for tracing the respiratory cycle but recommended the use of temperature or strain sensors due to their low price, commercial availability and patient comfort. *Mah et al.* conclude that a pneumotach spirometer is not suited to reliably track diaphragm motions of less than 4 mm [Mah00]. In a different approach *Ohara et al.* used an airbag to measure the thoracoabdominal

pressure in patients and reported a good patient comfort, but suggested to use more sophisticated sensors, like ultrasound or lasers, due to the easier daily handling [Oha89]. *Minohara et al.* attached an infrared light emitting diode (ir-LED) to the patient's body and monitored its position with a camera system based on position-sensitive semiconductor detectors (PSD) [Min00]. The camera signal of the ir-LED could successfully be used to follow the motion of the diaphragm. The phase of the detector signal was 200 ms delayed with respect to the internal motion and strongly depended on the position of the markers on the chest (difference of 120 ms). The position sensitivity of a similar setup was reported by *Bova et al.* to be 0.1-0.15 mm per LED with a camera-to-patient distance of 2.5 m [Bov97]. *Tada et al.* successfully utilised a laser displacement sensor being statically mounted above the patient and continuously measuring the distance between the sensor and the surface of the abdomen [Tad98]. They report only a small time lag compared to the ir-LEDs.
In general, the correlation of measured to internal motion differs from patient to patient and depends on the specific setup (marker positions, imaging direction etc.). None of the indirect tracking systems described above was able to trace the absolute internal tumour position with high enough precision for radiation therapy when purely relying on external motion information. However, determining the correlation to the internal motion for the single patient and frequently verifying it (e. g. by ionising imaging), indirect tracking of internal motion is possible. *Schweikard et al.* successfully used a combined approach to compensate respiratory motion during radiosurgery [Sch93c]. They attached infrared emitters to the patient's skin and monitored their position more than 60 times per second using optical methods. In the preparation session, a series of time-stamped snapshots were correlated to two-axes x-ray images, taken at the same time. From this information, a patient specific model on the relation of external and internal motion was derived. During the treatment session, a new set of x-ray images was taken every 10 s in order to verify the motion model. If the actual correlation between external and internal motion differed from the expected one, the model was updated in real-time. To reduce the time required to extract the internal motion information from the x-ray data, small gold markers had to be implanted close to the tumour. With this setup a typical respiration-related motion was reported to be traced in real-time with an accuracy of 1-2 mm [Sch93c].
In the combined approach the low x-ray imaging rate reduces the additionally applied, diagnostic dose to a tolerable amount. For a radiosurgical treatment with this system the integral dose is reported to be less than 50 mGy, corresponding to 0.25 mGy per image, assuming an image registration based on anatomical structures [Adl99]. At GSI, a typical irradiation time of 250 s per field [GSI02], an average of 2.5 fields per fraction and 20 fractions would lead to a total beam-on time for a heavy ion treatment of 1.25×10^4 s. An imaging rate of 0.1 Hz would yield a total of 1250 sets of x-ray images, each consisting of 2 single images summing up to a

total dose of 0.625 Gy (about 1 % of the therapeutic dose). In a dedicated clinical environment, the treatment time and cons3equently the diagnostic dose for motion tracking can be further decreased, for instance by roughly a factor of three for the planned Heidelberg facility [GSI02].
Real-time x-ray tracking is already used in gated radiotherapy to monitor the position of a 2.0 mm gold marker with two sets of diagnostic x-ray television systems, taking images at a rate of 30 Hz [Shi00]. This setup allows a tracking accuracy better than 1.5 mm in a pelvic phantom with an additional, estimated dose rate of 0.82 to 10.74 $\frac{\text{mGy}}{\text{min}}$ (exit and entrance dose respectively) [Shi00]. The conditions of a heavy ion treatment described above would lead to an additional skin dose to the patient of 2.24 Gy. Reducing the image rate from 30 Hz to 0.1 Hz, the integral contribution can be drastically reduced to less than 10 mGy (corresponding to about 0.01 % of the total prescribed target dose).
In summary, combining precise stereo x-ray imaging with non-radiative, indirect motion tracking offers flexibility in weighing tracking precision against diagnostic dose deposition. This way, the expected dose distribution due to online motion tracking can be included into treatment planning and optimised according to medical aspects.

3.4 Consequences and Management of Respiration-Related Motion

In case of conventional therapy the respiration-induced dose inhomogeneities inside the field are in the order of a few percent and thus negligible [Hen82]. To prevent underdosage of regions close to the border of the tumour, large safety margins, for instance about 15 mm in cranio-caudal direction for lung tumours [Ekb98], have to be applied. In many cases the tolerance dose for surrounding normal tissue and critical structures limits the maximum therapeutic dose inside the tumour.
Using intensity modulation the dose inside the static tumour can be raised while keeping the exposure of the surrounding tissue small. For moving tumours the interference between beam and target motion introduces dose inhomogeneities. In IMRT the dose applied to a moving target varies in extreme cases by up to 480% of the stationary target fluence over the tumour volume [Yu98]. Uncompensated spot scanning with charged particles is in the presence of any intra-fractional motion only possible, if the target displacement does not exceed the beam spot size and the volume is scanned several times averaging out the arising dose inhomogeneities [Phi92]. The beam diameters used in heavy ion therapy at GSI range from 4 to 10 mm FWHM. As described in chapter 3.2, the target displacement can be as large as 30 mm in some cases, making uncompensated raster scanning (without rescanning) of moving targets impossible.

In principle, all methods for high precision radiation therapy face the same basic problem if the target position is not static. The standard approach for static field irradiation is PTV extension in which the irradiation field is blown up as much as required to cover the target volume at any time. Intensity modulated radiation therapy, however is based on a position dependent variation of the dose distribution which requires exact knowledge of the location of the subvolume to be treated. Several strategies for the intensity modulated irradiation of moving target volumes have been investigated (for a summary refer to [Oku95, Lan01]). These strategies can be divided into three categories: rescanning, gating and online-compensation.

3.4.1 Rescanning

The strategy of target rescanning is derived from statistical considerations. It is based on the fact, that every volume element of a moving object has a motion specific, spatial probability distribution. Assuming that a point n is at the position of point n' with a certain probability $P(n, n')$, the dose received by n in a static field is [Li00]

$$D(n) = \sum_{n'} P(n, n') D_f(n') \tag{3.1}$$

with the fluence dose D_f. On the other hand, the basic idea of intensity modulated irradiation is a time-dependent fluence dose $D_f(n', t)$ at each spot n'. Consequently, it is not only important *how often* the voxel n is found at the position of n' but also *when* and a time-dependent probability function has to be considered. Therefore, the dose received by point n in an intensity modulated field is

$$D(n) = \int_T \sum_{n'} P(n, n', t) D_f(n', t) dt. \tag{3.2}$$

Unfavourable probability distributions $P(n, n', t)$ will lead to large dose inhomogeneities. In the worst case of a synchronous target and beam scanning motion, point i always follows the beam, while the next points ($i + 1$, $i + 2$, ...) are never hit. The dose received by the target volume elements $i + x$ would be far below the prescribed dose level, in the worst case zero. These cold spots have to be avoided under all circumstances, since the tumour cells in this voxel would most likely survive the treatment. On the other hand, a multiple of the lethal dose is deposited in voxel i. Such hot spots are not dangerous for the local tumour control, since the aim of the therapy is the death of all cells inside the target volume, anyway. None the less, any overdosage inside the tumour raises the probability for side-effects in the normal tissue affected by the beam.
From the statistical point of view, an uncorrelated target motion ($P(n, n', t)$) and intensity modulation ($D_f(n', t)$) will average the dose over repeated irradiations, improving the variance in the single scan dose distributions by $\frac{1}{\sqrt{N}}$ where N is the

number of scans. A large number of scans will yield an average dose distribution, which is independent of the detailed target motion pattern and can be adjusted to meet the requirements for a successful therapy. However, this is only true for the *average* dose distribution after *many* scans.
Bortfeld et al. [Bor02] simulated the effect of multiply painting the target volume with the same field for intensity modulated photon therapy (IMRT) and concluded that the variance in the single scan dose distributions is reduced by more than the purely statistical factor $\frac{1}{\sqrt{N}}$, even with a scanned photon beam. This estimate was based on the assumption that the spatial dose distribution is not altered by the displacement of internal structures [Li00]. For photons, this assumption is valid, but not for charged particles, which show a strong depth dependence on the density of the material in the entrance channel. *Phillips et al.* [Phi92] performed similar calculations for protons and found a slightly smaller reduction than $\frac{1}{\sqrt{N}}$. The effect of rescanning with ^{12}C ion beams is not investigated in the literature, yet. Corresponding simulations and an experimental study are included in chapters 4.3.4 and 7.1 of this thesis, respectively.
On the one hand, averaging over several uncorrelated motion states raises the dose homogeneity inside the tumour. On the other hand, in some of the motion states, the corresponding fraction of the total dose is deposited outside the target volume. The previously volume conformal dose distribution is smeared and, inevitably, the contribution to the normal tissue is increased. In addition, the dose homogeneity is restored only in the inner parts of the target volume. To apply a homogeneous dose to all parts of the target volume, the irradiation field has to be expanded (PTV extension), which even further increases the dose contribution to the normal tissue.

3.4.2 Gating

The rescanning approach does not require online information on the target position. The increased dose distribution in normal tissue results from the fact, that all possible motion states are included in treatment planning and the beam delivery does not differ between these states. Up to now, the most common strategy to overcome this limitation is gating the beam. The term *gating* refers to a controlled pausing of the irradiation, as long as a certain monitoring condition is not fulfilled. As soon as the condition becomes true again, the irradiation is resumed. As shown in fig. 3.2, the respiration cycle has a flat gradient around the point of maximum exhalation. If the irradiation takes place during this part of the breathing cycle only, the target displacement is drastically reduced, but a large fraction of the cycle is not used for the irradiation. Much more time is required to deposit the same amount of dose. Consequently, the total treatment time is significantly elongated. For a continuous beam delivery (DC), gating reduces the duty cycle to $\frac{1}{3} - \frac{1}{2}$ [Shi00]. A periodical beam structure (as provided by a synchrotron) further diminishes the duty factor

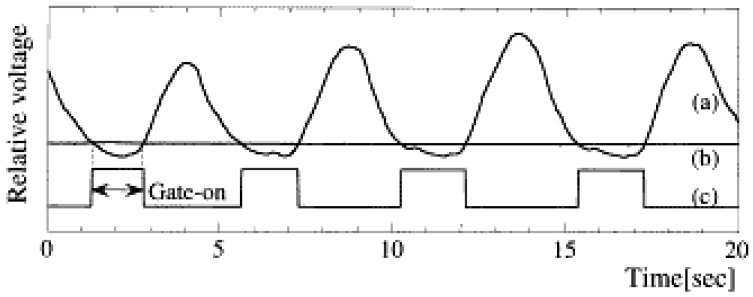

Figure 3.2:
Principle of respiratory gated irradiation (taken from [Min00]). At exhalation, the respiratory signal (a) has a flat gradient. The beam (c) is only active as long as the target position is within the predefined limits (b).

since the target might be in position for the irradiation while the accelerator is not ready for beam extraction and vice versa. *Minohara et al.* studied the performance of respiration gated heavy-ion therapy using a synchrotron as ion source and were able to reduce the target motion during irradiation to less than 10 % of the free breathing displacement (3.2/1.6/0.5 mm compared to 40.0/29.0/13.0 mm) with a gate-on period of 22.5 % of the breathing cycle [Min00]. The overhead in total irradiation time can be shortened using an accelerator with variable cycle time [Pöt98b]. This concept is shown schematically in fig. 3.3. The periods of irradiation (red) are defined by a positive respiration (target volume within pre-defined position window) and extraction trigger (accelerator ready for beam extraction). As soon as the target moves out of the position window, the irradiation is paused and a new accelerator cycle is started to have a full cycle available, once the target is back in position. But fig. 3.3 shows that even with this optimised mode of operation a significant fraction of time in which the accelerator is ready is not used for irradiation.
In principle, the required treatment time can also be reduced by accepting a larger part of the breathing cycle. But with this solution, the volume conformity is diminished, since a larger target motion is allowed. Breath-hold methods have been developed, arresting the target in the accepted position for a longer irradiation period. The breath-hold is achieved either actively by the patient (DIBH) [Han96] or passively by externally controlling the patient's breathing (ABC) [Won97].
In the deep inspiration breath hold-method (DIBH) the patient breathes freely through a spirometer. The patient is verbally coached through the breathing cycle and asked to hold his/her breath at a fixed level of inspiration according to the spirometer readings. The irradiation takes place during breath-hold only. As soon as the patient starts breathing again, the beam is switched off. Breath-holds as long as 12-16 s were reported to be well tolerated for 10-13 maneuvers per session [Han99]. The main disadvantage of DIBH is the coaching process itself. On the

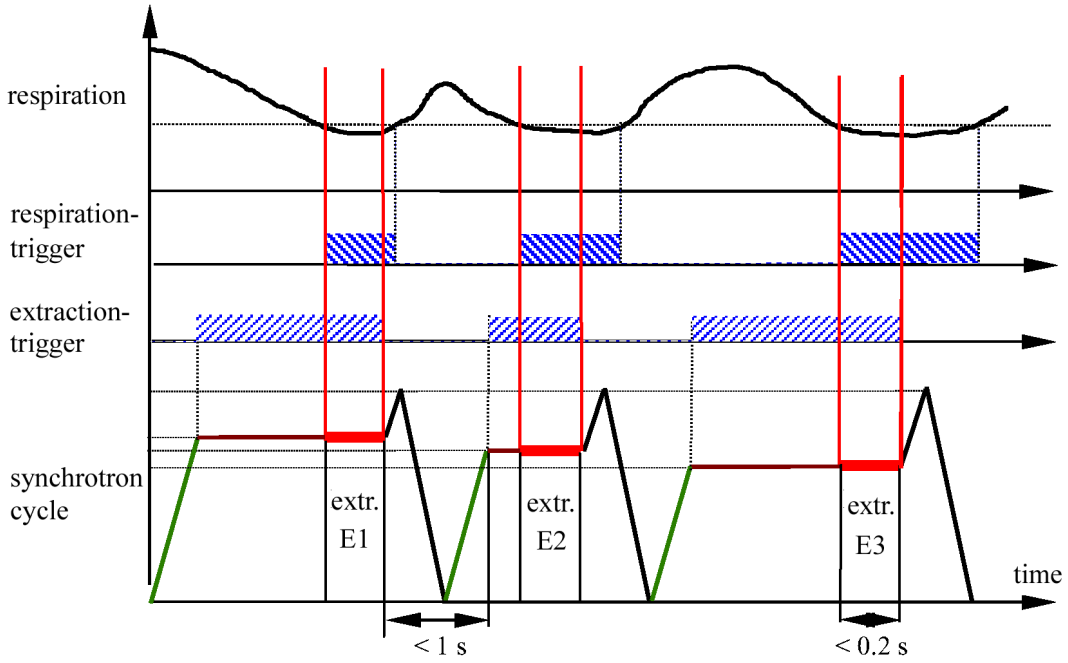

Figure 3.3:
Gating with variable accelerator cycle [Pöt98b]. The irradiation is triggered on the respiration pattern of the patient and the extraction cycle of the accelerator. As soon as the target moves out of the pre-defined position window, the current accelerator cycle is cancelled and a new one started.

one hand, not all patients are able to follow the slow vital capacity protocol used for DIBH [Mah00]. On the other hand, the consistency of the maneuver depends on the daily form of patient and coach. Moreover, intra-breath-hold displacements of up to 4 mm may occur without being realised [Mah00].
In contrast to DIBH, the active breathing control method (ABC) does not rely on the cooperation of the patient. Instead, the patient breathes through a mouthpiece connected to a valve, which shortly interrupts the air flow to the patient at a specific point in the breathing cycle. 11 out of 12 patients were able to stand a breath-hold time of 20 s and longer [Won99]. In initial studies the breathing motion was reproducibly immobilised to about 3 mm [Jaf99].
A gating functionality can be included into any beam delivery system with moderate technical effort. It has to allow a controlled pausing of the irradiation and requires an optimised resuming procedure. However, gating always results in an elongation of treatment time, which limits the patient throughput and thus the number of benefiting people. The amount of extra time is always a compromise to the accuracy. The possible target motion during the beam-on period has to be

included into the treatment planning. Compared to rescanning, gating reduces the dose contribution to normal tissue at the expense of treatment time. Although these restrictions do not generally exclude gating from the list of feasible methods for the irradiation of moving target volumes, it was not investigated in more detail in the current thesis.

3.4.3 Online Compensation

The more direct approach to expand *all* benefits of volume conformal, intensity modulated therapy to sites, which are subject to intra-fractional organ motion, is the synchronous compensation of target displacement in real-time. If the beam delivery system is fast enough, as for instance the magnetic raster scanning, the beam can follow the displacement of the target volume in addition to the dynamics required for intensity modulated irradiation. Up to now, online motion compensation has only been investigated for IMRT. [Kea01]. In an experimental study a pre-determined motion pattern of the field shaping multileaf collimators was superimposed with the known motion of the target volume (cf. fig 3.4). In this approach, the beam follows the motion of the target centre of mass, instead of gating the beam if the target displacement is too large. The target is always illuminated by the beam in the same way as if it was static. No additional safety margins for target motion have to be added and the dose is not smeared into normal tissue. In the ideal case, the accuracy of online motion compensation is only limited by the motion detection system.
Generalised to 3D, the same strategy can be applied for ion therapy. In the treatment planning process the target volume is divided into subvolume elements (voxels) each of them containing a single, planned beam position, which are processed consecutively in the irradiation process. These voxels are characterised by the position (x_i, y_i, z_i) as well as an assigned number of particles N_i. If the position of the voxel does not change significantly while it is irradiated, the scanning technique offers the possibility to correct for the displacement $\Delta\vec{x}(t)$ of the next voxel at the moment of its irradiation

$$(x_{i+1}, y_{i+1}, z_{i+1}) \longrightarrow (x_{i+1} + \Delta x(t), y_{i+1} + \Delta y(t), z_{i+1} + \Delta z(t)) \qquad (3.3)$$

so that the number of particles dN_{i+1} is delivered to the right part of the target volume. If the target moves very fast or the number of particles to be deposited is very high, a significant displacement might occur during the irradiation of a single point. In the worst case, the single spot dose would be smeared over several voxels. This can be avoided by subdividing the irradiation of the single voxel into short periods in which the displacement is not too large and applying the displacement compensation several times for the same voxel.
In contrast to photon beams, the depth dose distribution of ions exhibits a pronounced enhancement of dose deposition in a short distance at the end of the track

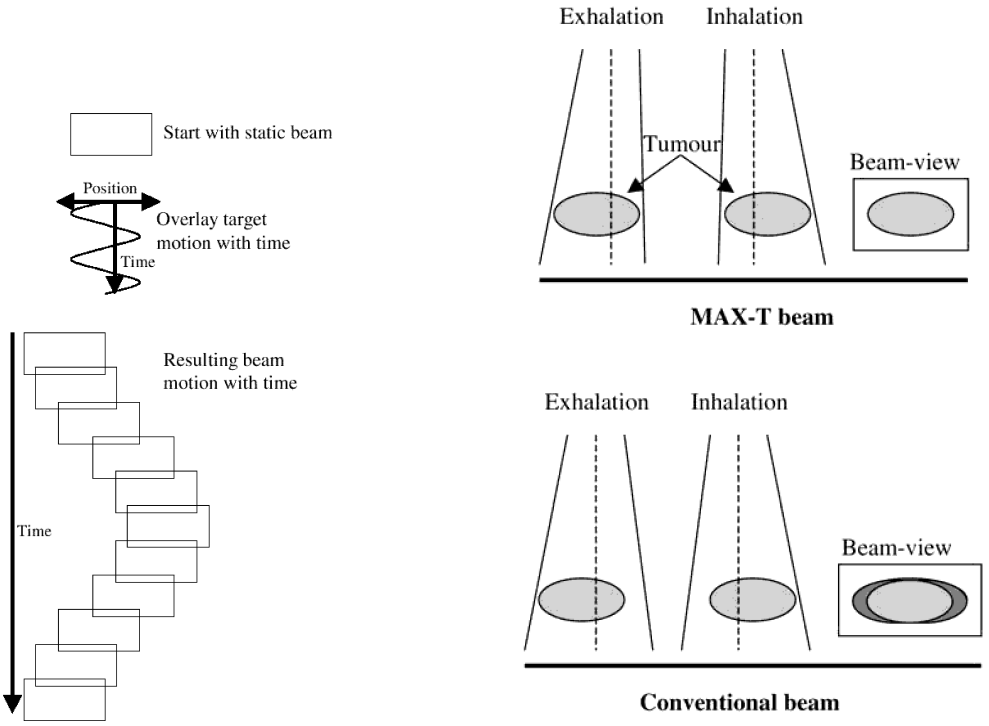

Figure 3.4:
Principle of online motion adapted x-ray therapy (Max-T) [Kea01]. The field shaping multileaf collimator motion is superimposed by the displacement of the target centre of mass and the static beam follows the moving target. Since the beam is dynamically tuned to match the target, no additional margin for target motion is required.

(see fig. 2.1). Being extremely suitable for dose shaping in the static target case, this feature introduces severe distortions when considering target motion. Fig. 3.5 illustrates schematically the error in dose deposition which results from a shift in the radiological path length for the photon and the carbon ion case. Due to the exponential attenuation of the beam, the effect can be neglected in the photon case. Even if the target volume is not located close to the maximum of dose deposition, as it is the case for superimposed fields, the effect will be much smaller than in the ion case. The narrow peak structure of the depth dose distribution of ^{12}C ions causes relatively small deviations in depth to contribute to a large degree in the dose. Since ion therapy is optimised to have the Bragg peak in the corresponding volume element, the influence of changes in radiological path length is always extremely high. Therefore, the depth information has to be considered very carefully

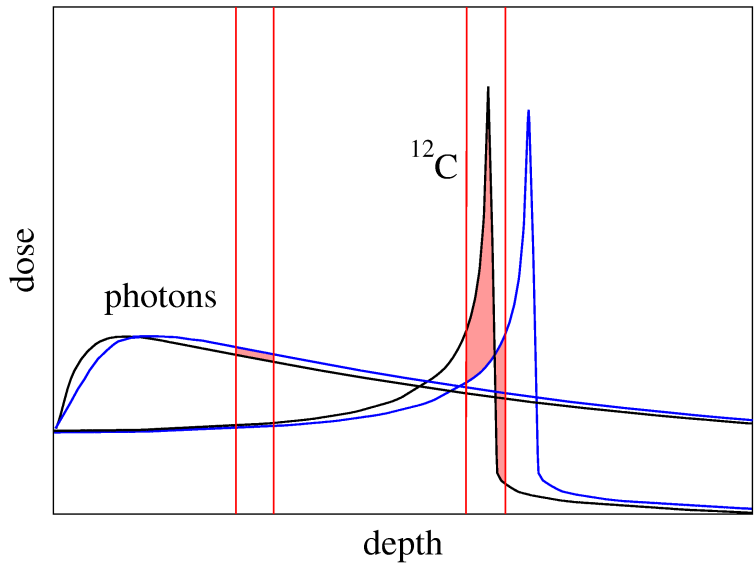

Figure 3.5:
Schematic illustration of the effect of variations in radiological path length on the dose deposition of photons and ^{12}C ions. The blue curves represent an arbitrary reduction in radiological path length in front of the target volume, which is enclosed by the vertical red lines. The light red, filled areas mark the dose deviation compared to the unmodified path length. The effect is negligible in the photon, but not in the ^{12}C ion case.

and included into the online compensation process when irradiating moving target volumes with ion beams.
The concept of online motion compensation offers the possibility of target motion independent, high precision tumour therapy. Limited by the precision of motion tracking, safety margins accounting for inaccuracies in the target position can be reduced. In addition, using this technique one might be able to loosen the rigid patient fixation [Bet04]. Small variations in the position of the patient's body can be tracked externally and compensated online. The prerequisite of 3D online motion compensation are the considerable technological effort in adapting the control and safety system for beam delivery, the intrinsic need for precise, real-time target motion information and, in ion therapy, the required motion adapted treatment planning (cf. chapter 5).
In the current thesis, a system for 3D online motion compensation (3D-OMC) based on magnetic raster scanning of ion beams was developed and tested. This system allows real-time compensation of target motion with the therapeutic ion beam in all three dimensions. Its concept and design is described in more detail in chapter 5.

Chapter 4

Simulating the Effect of Target Motion

In this chapter, the effect of target motion and different compensation strategies for intensity modulated heavy ion irradiation are systematically investigated in a series of simulations.
The validity of the existing treatment planning routines for the irradiation of static target volumes [Krä01] has been shown in numerous physical and biological experiments, as well as the successful patient treatment since 1997 [Jäk01]. Therefore, the results of the static treatment planning are taken as reference in all simulations for the moving target volumes. The fundamental idea of radiation therapy is a homogeneous, high damage inside the target volume. When considering the physical dose only, the amount of damage directly corresponds to the applied dose. Therefore, the target volume has to be painted homogeneously with the prescribed dose.
A measure for the dose inhomogeneity inside the target volume is the standard deviation of the dose contributions to the single volume elements (voxels). The *dose homogeneity* is defined as the difference to a fully homogeneous dose deposition

$$H_d = 1 - \frac{\sigma}{\bar{D}} = 1 - \frac{1}{\bar{D}}\sqrt{\frac{\sum_i (D_i - \bar{D})^2}{N-1}}, \tag{4.1}$$

with the single voxel dose D_i, the mean dose over the region of interest (ROI) $\bar{D}$ and the number of voxels in the ROI N. In the simulations, the dose homogeneity has been chosen as a suitable quantity to estimate the amount of motion-related distortion on the dose distribution delivered to moving targets. The optimisation of the dose homogeneity inside the target volume is for static targets an already solved problem of the treatment planning process.

4.1 Simulation Environment

The simulations are performed within the framework of the treatment planning code TRiP98 described in chapter 2.4.4. The effect of different motion parameters

and compensation strategies is studied by calculating the dose distribution of a static treatment plan delivered to a moving target volume under the conditions of the respective beam delivery. For all treatment planning steps, apart from the dose calculation, the unmodified TRiP98 routines, as described in [Krä01], are used. Based on the dose calculation routine, the signal of non-linear dose detectors (e. g. x-ray sensitive films) moving in the irradiation field is calculated. The simulations refer to the physical dose, without considering the RBE problem.

4.1.1 Dose Calculation Algorithm

To calculate the effect of a static treatment plan, delivered to a moving target volume, a modular function has been added to the treatment planning code TRiP98 [Li04]. For compatibility reasons, this function uses the core dose calculation routines for the static case. The next paragraphs shortly summarise the principles of the dose calculation algorithm for static target volumes. The extension to moving target volumes is described later.

Static Target Volumes

In general, the dose contribution of a single, Gaussian-shaped heavy ion beam with energy E_{beam}[MeV] and width σ[mm], centred at (x_0,y_0), to the target position $\vec{x}$ is given by

$$D(E_{beam},\vec{x})[\mathrm{Gy}] = 1.6\times10^{-8} d(E_{beam},z)\frac{N}{2\pi\sigma^2}\exp\left(-\frac{1}{2}\frac{r^2}{\sigma^2}\right) \tag{4.2}$$

where N is the total number of deposited particles and r the distance of the target position from the beam centre [Krä01]. The one-dimensional energy loss distribution $d(E_{beam},z)$ and the fragment spectra are derived from the physical beam transport model YIELD [Hab94] which describes the ion interaction with tissue.
One of the main advantages of heavy ion irradiation is the small lateral scattering. In the case of a carbon ion beam this scattering is negligible with respect to the initial beam width delivered by the accelerator. For first order dose optimisation purposes, it is sufficient to approximate the Gaussian beam profile by a delta-function [Krä01], simplifying eq. (4.2) to

$$D(E_{beam},\vec{x})[\mathrm{Gy}] = 1.6\times10^{-8} d(E_{beam},z)F(E_{beam},x,y) \tag{4.3}$$

with the ion fluence in units of $[cm^{-2}]$

$$F(E_{beam},x,y) = \frac{N(E_{beam},x,y)}{\Delta x\Delta y}. \tag{4.4}$$

where Δx and Δy represent the scanner step sizes. The total dose to a single point is accumulated from the contributions of all beams passing through that point, i. e. a weighted sum over all energies.
For the visualisation of the 3D dose distribution in a complex target, like the human body, the contribution to small volume elements (voxels) of a certain electron density, derived from the CT data, has to be calculated. The coordinates of the CT voxels are transformed into the water-equivalent (WE) beams-eye-view system $\vec{x}_{H_2O}$, in which the beam positions (raster points[1]) are defined (CT-to-WE transformation). Via binary grid search, the four closest raster points in the same slice are determined. The dose applied to the CT voxel is calculated via bilinear interpolation between the single point doses of these four points [Krä01]

$$D(\vec{x}) = 1.6 \times 10^{-8} \sum_{E_{beam}} \sum_{i=1}^{4} \xi_i d(E_{beam}, z_i) N_{acc}(E_{beam}, x_i, y_i) \tag{4.5}$$

with the relative weighting factors ξ_i describing the relative position of $\vec{x}_{H_2O}$ between the four neighbouring raster points (cf. fig. 4.1)

$$\begin{aligned} \xi_1 &= (1-t)(1-u) \\ \xi_2 &= t(1-u) \\ \xi_3 &= (1-t)u \\ \xi_4 &= tu \\ t &= \frac{x - x_k}{x_{k+1} - x_k} \\ u &= \frac{y - y_l}{y_{l+1} - y_l} \end{aligned} \tag{4.6}$$

and the accumulated particle contribution from all raster points on the grid

$$N_{acc}(E_{beam}, x_i, y_i) = \sum_j \frac{1}{2\pi\sigma^2} \exp\left(-\frac{1}{2}\frac{r_{ij}^2}{\sigma^2}\right) N(E_{beam}, x_j, y_j) \tag{4.7}$$

where $r_{ij}^2 = (x_i - x_j)^2 + (y_i - y_j)^2$ is the distance to the contributing point. The index j includes all raster points on the grid which contribute with more than 1 % of the total particle number.

[1] Raster points are points on a regular grid spaced by Δx and *Deltay* which represent the potential beam positions. The number of particles to be deposited at each raster point is determined by the dose optimisation routine. If the required number is zero, the beam is not directed to this position in the irradiation.

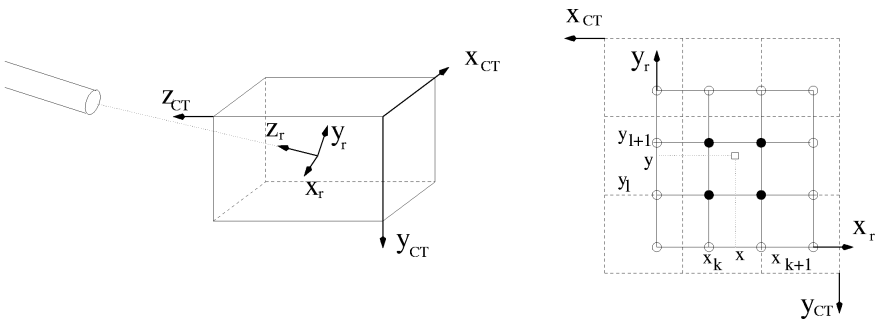

Figure 4.1: Relation between raster and coordinate system [Krä01].

Moving Target Volumes

In principle, the dose calculation algorithm on the CT grid (eq. (4.5)) is valid for the moving target volume as well. In contrast to a static target position, target motion introduces a time dependence in the dose calculation process. The binary grid search, the relative weighting factors ξ_i (eq. (4.6)) and the particle contribution from all raster points $N(E_{beam}, x_j, y_j)$ (eq. (4.7)) become dependent on the state of motion. Within the same state of motion, the dose calculation algorithm of the static case can be used without any modifications. Following this strategy, the new TRiP98 function for the dose calculation to a moving target subdivides the irradiation process into several discrete motion states. Fig. 4.2 shows schematically how the applied distribution to moving target volumes is determined. According to the time correlation, described in chapter 4.1.2, the start- and end-of-irradiation time for every single voxel in the target volume is determined. Starting with the first point at time $t = 0$, the target displacement for all voxels at the time of their irradiation is calculated. For each motion state, the particle fluences of all raster points, except of those with the same target displacement (motion state) at the time of irradiation, are temporarily set to zero. A target displacement leads to a shift of the CT data cube, describing the target material, with respect to the stationary raster system. The CT-to-WE transformation yields a different $\vec{x}'_{H_2O}$, a different set of neighbouring raster points and finally modified relative weighting factors ξ_i (eq. (4.6)). With the new relative weighting factors ξ_i the partial dose distribution can be calculated according to eq. (4.5), taking into account the contribution from those raster points only, which are processed in the same state of motion. If the target moves significantly during the irradiation of a single raster point, the resulting smearing of the dose would not be included in the calculations. Therefore, eq. (4.6) is not only updated once for every point, but within a regular time interval. If the irradiation time of a single point exceeds this interval, the weighting factors are updated again and the dose calculation continued with the new values, i. e. the point is virtually split into two or more points with the same

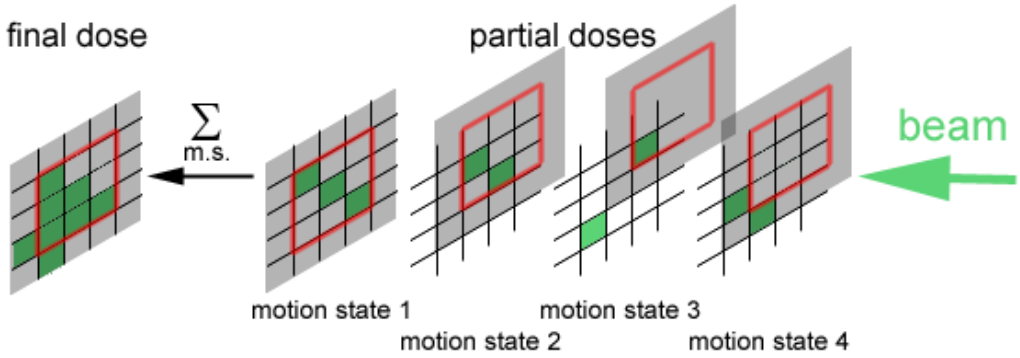

Figure 4.2:
The final dose to a target volume (red box) is calculated in the simulation environment as a sum of the partial doses of all motion states (m.s.). The partial doses of the single motion states include only contributions from those points, which are irradiated at a time, when the target volume is at the same position. In the final dose distribution, some parts inside the target volume have not received any dose, while other parts outside received the full therapeutical dose.

coordinates and total number of deposited particles. The length of this time interval determines the resolution of the dose calculation. Any motion within this time interval is neglected. Since the binary grid search is quite time consuming, the choice of the time resolution is a compromise between precision and computation time. During the development of the dose calculation code for the moving targets, the time resolution has been optimised to 10^{-2} s, corresponding to an uncertainty of 1 % in the dose homogeneity over the IESs and a practical computation time of several hours [Li04]. The sum of the partial dose distributions for all motion states and time intervals yields the final dose distribution applied to the moving target volume.

To simulate the effect of online motion compensation, the raster grid specifying the beam positions can be transformed, as well. In contrast to the CT transformation, which simulates the target motion, the raster grid transformation is straightforward. Offsets are added to the raster coordinates to shift the grid with respect to the CT volume. This influences the results of the binary grid search and thus the raster points contributing to the dose of the CT voxel. A shift of the raster coordinates is in direct correspondence with a shift in beam position. Performing both transformations (CT and raster system) in parallel, online target motion compensation can be simulated. A random positioning inaccuracy can be applied to the raster transformation, in order to investigate the technical hardware requirements. Based on the dose calculation algorithm, the response of non-linear detectors can be simulated for moving target volumes.

The target motion as a function of time can be approximated by a cyclic, sinusoidal dependence, according to the motion parameters discussed in chapter 3.2. Alternatively, a set of externally measured target displacement data can be imported. Further information about the single internal parameters of the dose calculation algorithm for moving targets and their optimisation can be found in [Li04].

4.1.2 Time Correlation via Beam Intensity Profile

The major challenge in the simulation of the expected dose distribution to a non-static target volume is the time correlation between scanning progress and target displacement. For a static target position (and orientation), the final dose distribution is absolutely independent of the time point in the irradiation process, at which the planned number of ions is delivered to a certain raster point. As soon as the target position becomes time-dependent, the exact start- and end-of-irradiation time for the single points determine the displacement of the ions with respect to the planned beam position. In the case of uncompensated target motion, different time correlations result in different dose distributions. To calculate the expected dose distribution for a certain target motion pattern, the exact time correlation between scanning and target motion has to be included in the simulation environment.
During the irradiation, the processing time of the single raster points depends on the beam intensity. In the GSI setup, the number of deposited ions is compared to the planned amount every 12.5 μs and if the value is reached or exceeded, the beam is deflected to the next point. Once optimised in the treatment planning process, the sequence of points is fixed.
To restore this time correlation in the off-line simulations, virtual ions of a measured beam intensity distribution (spill profile) were counted. Starting with the first raster point at time t_1^s=0, the ion rate in the beam spill profile is integrated until the sum of deposited particles reaches the planned value. This time value is set as the end of irradiation time t_1^e of the first point. Next, the time for the scanner transition to the second point is calculated and added to t_1^e to yield the start of irradiation time of the second point[2] t_2^s. In the same way, t_i^s and t_i^e are calculated for all raster points in one slice. If the end of the sample spill is reached before the start- and end-of-irradiation time for all points in the slice is determined, 3 s for refilling the synchrotron are added to the irradiation time of the current point and the ion rate integration is continued with the same beam spill profile. If the slice is completed, the remaining time in the current spill data and the 3 s beam spill break are added to the end-of-irradiation time of the last point in the slice to yield the starting time for the irradiation of the first position in the new IES.

[2] As in reality, all ions which are deposited during this very short transition period are already accounted to the next point. Consequently, the fact, that the scanner moves to the next point without the beam being switched off, causes a small misalignment of the dose, but no additional dose deposition (overdosage).

Obviously, each beam intensity level has a different ion rate. In cases were the beam intensity level of the next IES is not identical to the current one, the time calculation is continued with a different sample spill data set corresponding to the new accelerator settings. The start- and end-of-irradiation times for every single planned beam position in the target volume are calculated and stored. From these values the time dependent target displacement and the resulting dose distribution can be determined, as described in chapter 4.1.1.
Off-line calculation of the time correlation via sample beam intensity profiles is the only way to simulate the effect of arbitrary target motion patterns on the dose distribution. The beam intensity data is routinely monitored with a storage oscilloscope (LeCroy 9310 AM), which displays the amplified signal of one of the ionisation chambers of the therapy safety and control system. Single beam spill profiles with a time resolution of 10^{-5} s can be stored. Online beam intensity logging, however, is currently not possible due to the time required to read out the oscilloscope. For the simulations in this thesis, a set of sample beam intensity profiles has been measured for different accelerator settings at different times. Fig. 4.3 shows a sample of a measured beam spill profile. The intensity distribution has a flat increase of ion rate at the beginning and a similar decrease at the end. For a perfectly tuned

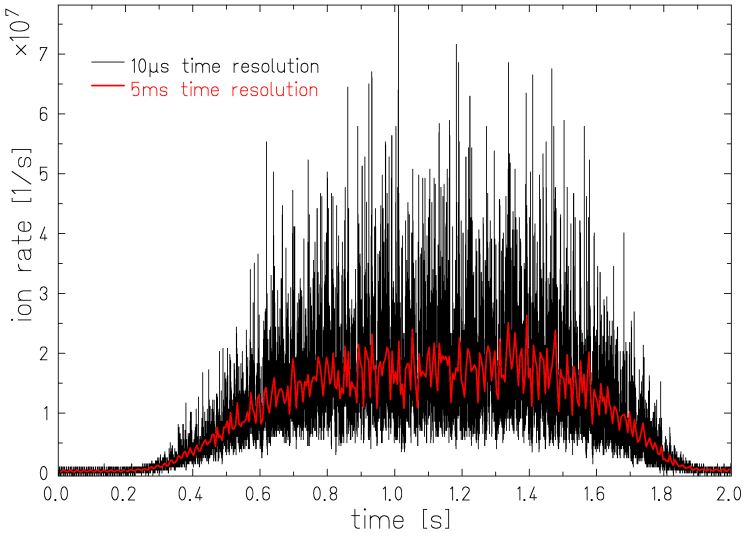

Figure 4.3:
The measured beam spill profile (black) shows two main features: A general bump-like form, determined by the accelerator settings, and a fine, random spike structure, which varies from spill to spill. To get rid of the large inter-spill variations, a reduced data set (red) is used for the simulations, being the original data averaged over 500 entries.

accelerator, the form of the intensity profile should be the same for all spills with the same accelerator settings. On top of this general structure are very fine, random spikes which vary from spill to spill. Some of the spikes have a factor of 3-4 in beam intensity compared to the average value and therefore strongly influence the time correlation. Without real-time beam intensity logging, the strategy of off-line calculating the time correlation is only an approximation for a verification of measured dose distributions. In order to get rid of this strong influence for the dose calculation, the 10^5 Hz data set (black) is averaged over 500 entries, reducing the resolution to 200 Hz (red). This reduced beam spill profile shows the same general form as the original set, but with less random fine structure. It represents an average beam spill profile of one accelerator setting.

Even the general form of the beam spill profiles varies, depending on the accelerator settings. The influence on the form is dominated by the spill extraction process. For different extraction time points within the synchrotron cycle, the beam intensity profile changes significantly. Fig. 4.4 shows reduced data sets of two spills for identical accelerator parameters, taken at two different time points in of the same therapy block. Except for trouble shooting, routine checks in the morning of each therapy day and general machine settings for physical experiments during the night,

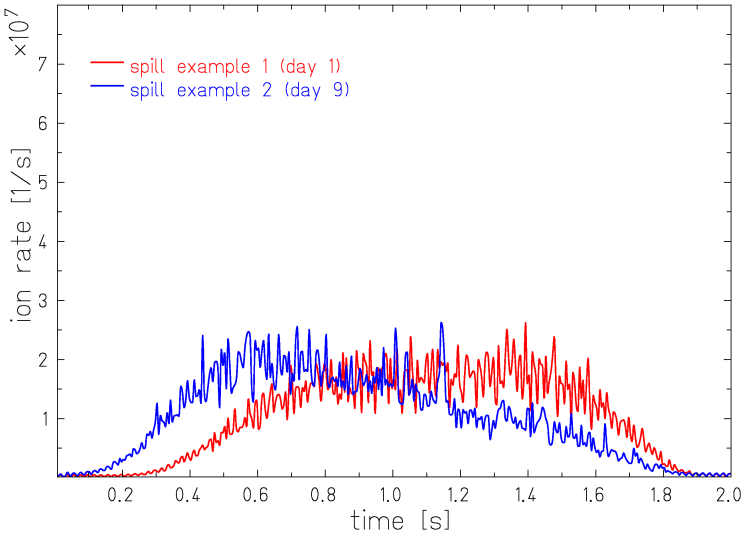

Figure 4.4:
Comparison of two reduced data sets for identical accelerator parameters, taken at two different days in the same therapy block. Although the virtual accelerator data set remains largely unchanged, the general form of the beam intensity changes. This effect is mainly due to variations in the ion extraction process from the synchrotron.

the virtual accelerator data sets remain unchanged over the course of one therapy block. Nevertheless, the two spill profiles in fig. 4.4 show a different general form. This effect is too large to be averaged out in the beam intensity data. For the simulations in this thesis, the effect is estimated by a comparison of different beam intensity profiles in chapter 4.3.1.

4.2 Target Configuration

If not stated otherwise, the simulations are performed with the following target configuration: The CT volume consists of a $100\times100\times100\,\mathrm{mm}^3$ cube of WE material with a spatial resolution of $2\times2\times2\,\mathrm{mm}^3$. Centred in this cube is a spherical volume of interest (VOI) with a diameter of 60 mm. This spherical target volume is planned to be filled homogeneously with a physical dose of 1.0 Gy. The beam positions are optimised on a $2\times2\times2\,\mathrm{mm}^3$ raster grid. The sequence of beam positions is determined according to the rules of the scanning path algorithm *tm* (cf. chapter 5.2.3). This algorithm moves the beam predominantly in the vertical direction.
A sphere represents a volume which can be fully described with analytical functions, but it is complex enough, to simulate realistic therapy conditions. A spherical target volume consists of slices with different diameters. Due to the pre-irradiation of more proximal slices, a homogeneous dose distribution requires an inhomogeneous particle coverage of the different slices. Fig. 4.5 illustrates this fact with the optimised raster data for all slices of the 60 mm sphere, starting with the most distal one. The irradiation parameters are optimised for a static target position and used as input for the dose calculation of all cases (static, moving, compensated).
The sphere represents a small but realistic tumour with more than 16 000 beam positions. Due to the large number of beam positions, the irradiation takes several minutes, which is enough time to study motion effects. The motion parameters were adapted to clinically realistic parameters, as discussed in chapter 3.2.

4.3 Results

4.3.1 Influence of the Beam Spill Profile

In order to estimate the influence of variations in the beam spill profile on the calculated dose, the irradiation of a typical target volume is simulated under exactly the same conditions with two different beam intensity data sets taken at two different days. A comparison of the resulting dose distributions reveals the influence of the beam spill profile on the calculations. The variations in the beam intensity profile modify the time spend for the irradiation of a pixel. Consequently, different target displacement values are determined. In this case, a large, overall target motion affects the dose distribution more than a small motion.

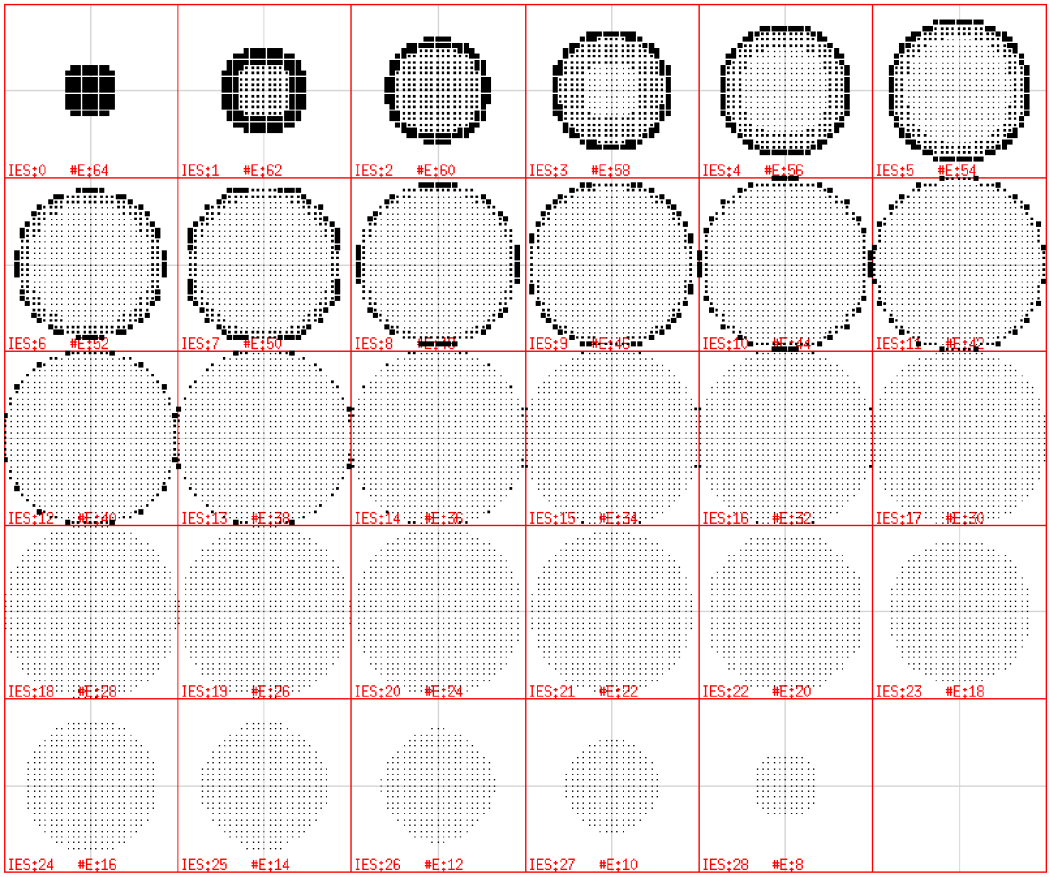

Figure 4.5:
Treatment plan for a spherical VOI, to be homogeneously irradiated with a physical dose. Each spot represents a beam position and its size indicates the amount of particles to be deposited at that point. Due to the pre-irradiation of proximal points, only the most distal slice consists of points with a constant, maximum particle deposition (large spots). In the more proximal slices, the inner positions did already receive a part of their final dose by pre-irradiation, and less particles have to be deposited at these spots.

For a worst case estimation, the largest motion parameters considered in the simulations are chosen. This corresponds to a target motion with an amplitude of $\pm 15\,mm$ in each direction. In this case, the motion pattern was chosen to be purely lateral, as this is the most relevant situation for the comparison with the experimental data (cf. chapter 7.4), where absolute values for the homogeneity are required. The theoretical 3D studies in the current chapter perform relative comparisons, only. The motion frequency is set to 0.25 Hz. Without loss of generality, the initial phase for the displacement calculation was chosen to be 0° . The resulting dose homogeneity

(H_d) per IES as a function of the depth in the CT cube is shown for both spill example profiles in fig. 4.6. The peculiar form of the dose homogeneity is discussed

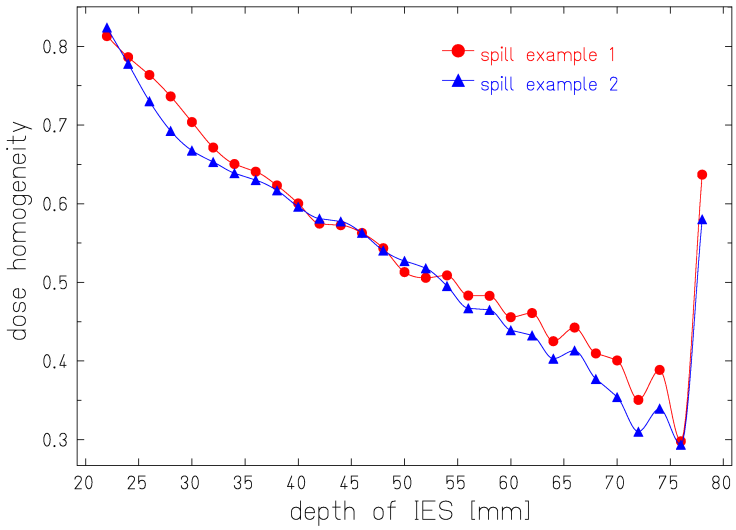

Figure 4.6:
The simulated dose homogeneity in the single slices of the test volume is not strongly influenced by the significant differences in the two beam intensity profiles.

in more detail in chapter 4.3.2. Although the beam spill profiles differ significantly from each other (cf. fig. 4.4), the dose homogeneity shows in both cases roughly the same depth dependence. This reflects the fact that dose homogeneity provides an averaged information over the region of interest. To get a better estimation of the beam profile influence, fig. 4.7 provides a histogram of the differences between both H_d distributions, showing that the homogeneity for the single slices does not differ by more than 6 % (absolute). For the experimental study in chapter 7.4 this value is taken as systematic error for the simulation of the expected dose distribution delivered to a moving target volume. In future, this systematic error can be reduced by a better knowledge of the actually applied beam intensity.

4.3.2 Translation of Target Volume

Breathing causes a quite regular cyclic internal motion with dominantly translational components (cf. chapter 3.2). Since any periodical function can be Fourier decomposed into a superposition of sinusoidal functions with different initial phases, the simulation assumes a sinusoidal motion pattern. The driving force for any respiration-related, internal motion is the expansion of the lung, affecting the whole organ. Therefore, a common initial phase Φ and motion period T are assumed for

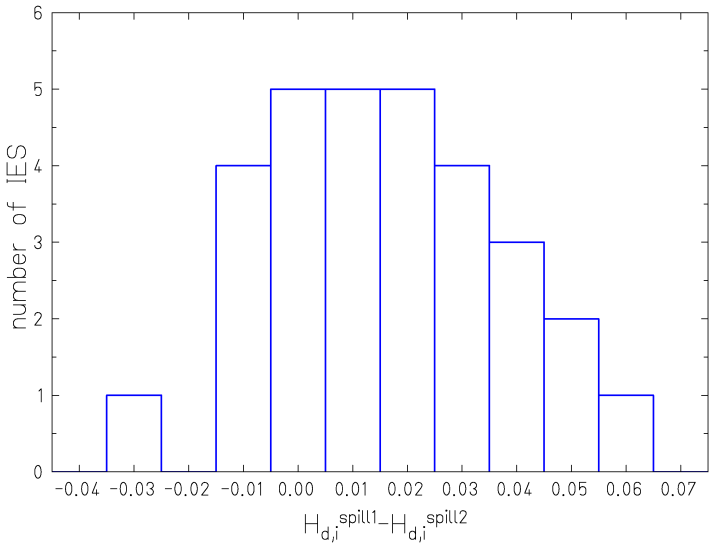

Figure 4.7:
Histogram of the difference in dose homogeneity over the single IES of a spherical target volume with 60 mm diameter, introduced by variations in beam intensity profile.

all three dimensions. To account for the anisotropy of the inner motion, the amplitude A_i can be set individually for each direction. The single components of the displacement vector Δx_i are determined by

$$\Delta x_i = A_i \sin\left(2\pi \frac{t}{T} + \Phi\right). \tag{4.8}$$

The influence of the single parameters of the purely translational target motion in eq. (4.8), is systematically investigated in the current section. If not stated otherwise, the simulations refer to the conditions described in chapter 4.2.

Influence of Motion Amplitude

The interference between target displacement and beam scanning procedure causes significant deviations from the expected, homogeneous dose distribution. Fig. 4.8 shows as an example a dose distribution histogram of the IES in 55 mm depth. In the static case, the slice is filled homogeneously with the optimised dose which sharply drops at the target boundary. For a 1-dimensional, cyclic target motion in x-direction with an amplitude of 15 mm, the simulated dose distribution is heavily distorted. The interference between target motion and beam scanning generates regions of over- (hot spots) and underdosage (cold spots) inside the target boundaries. The detailed pattern of the distortions strongly depends on the phase shift

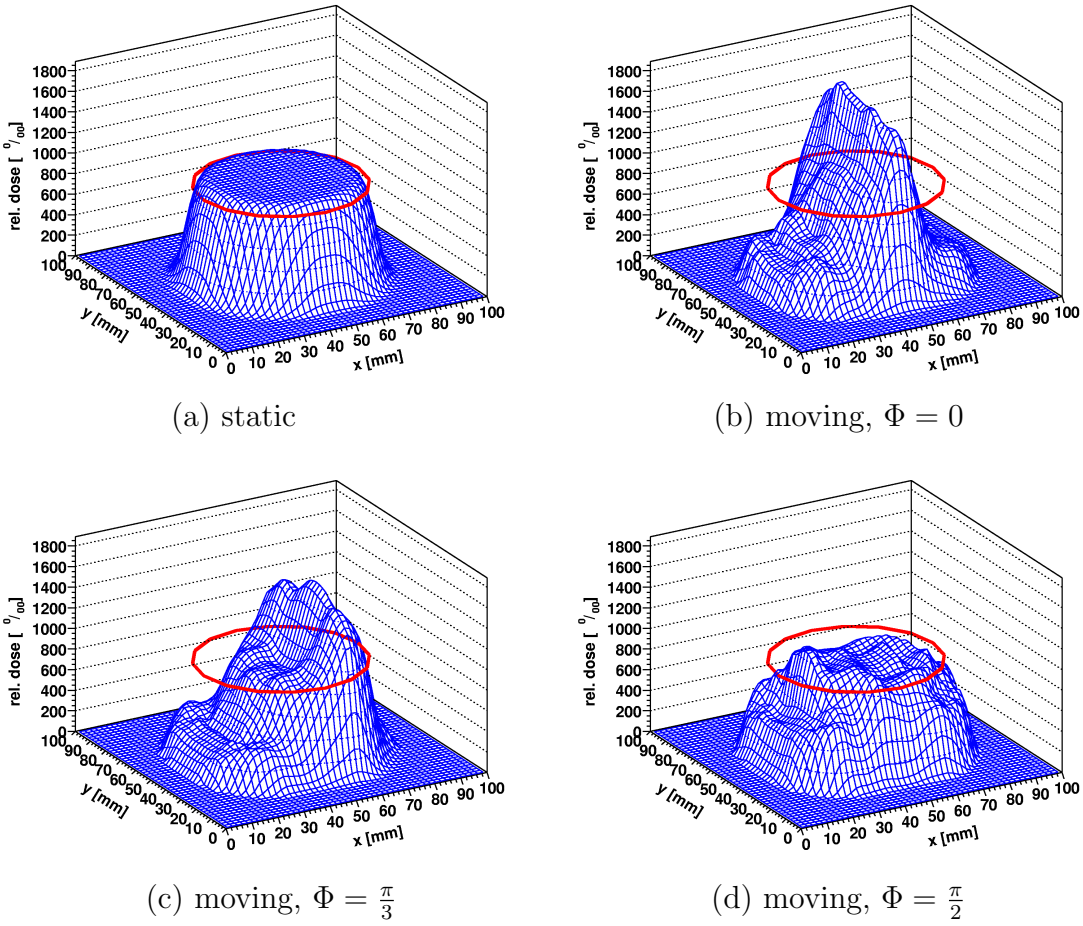

(a) static

(b) moving, $\Phi = 0$

(c) moving, $\Phi = \frac{\pi}{3}$

(d) moving, $\Phi = \frac{\pi}{2}$

Figure 4.8:
The dose distribution histograms show the calculated dose levels for the single pixels of a middle IES (55 mm depth) of the spherical target volume. The target boundary is indicated by the red circle. In the static case (a), the target volume is filled homogeneously with an average dose. If the same target moves periodically during the irradiation (A_x =15 mm, $A_y = A_z$ =0 mm), large interferences destroy the homogeneity (b-d). The detailed distortion pattern strongly depends on the phase Φ between target and scanning motion.

between target and scanning motion. For a phase shift of Φ=0 the hot spots in the current example receive up to almost twice the planned dose, whereas other parts of the target get only a third of the dose. In the clinical application, such large dose deviations in both directions will jeopardise the success of the therapy, reducing the dose homogeneity inside the target in this example from 98.39 % in the static case to 55.80 % for the moving target. A phase shift of $\Phi=\frac{\pi}{2}$, on the

other hand, yields a smooth but wide dose distribution. Compared to the Φ=0 case, the resulting dose homogeneity is higher (86.33 %), but the dose contribution to the outside of the target volume is increased by approximately $\frac{1}{3}$. The following simulations assume a static phase shift Φ=0 as a worst case estimation for the dose homogeneity with the used target geometry. The influence of the initial phase is studied in more detail in chapter 4.3.2.
Fig. 4.9 shows the dose homogeneity inside the target boundary of the single IESs of the spherical target volume in dependence of the motion amplitude and direction as a function of the IES depth. Except for the very distal end cap of the sphere, the dose homogeneity drops for all IES with increasing motion amplitude. The peculiar depth dependence reflects the influence of the IES size on the dose homogeneity value. A small slice is irradiated in a very short time interval. In this interval, the target displacement does not change much. Consequently, the dose is simply shifted by a constant offset and the pixel-dose variance is small; the distribution is considered to be more homogeneous. That is the reason for a rising homogeneity of the most distal slices. On the other hand, the proximal slices receive their dose partially by the pre-irradiation from more distal slices, which leads to an averaging of the motion-related effect. Therefore, the dose homogeneity rises towards the target surface, as well.
The magnitude of the motion-related effect depends on the direction of the motion. The largest effect occurs if the target moves parallel to the slow beam scanning direction (upper part of fig. 4.9). For a clinically realistic motion amplitude of $\pm$15 mm the homogeneity drops below 40 % in some slices. If the target moves in the other two directions, the influence is much smaller. In these cases the homogeneity is better than 80 % in all IES. To explain this behaviour, fig. 4.10 visualises the effect of the motion direction on the 2D dose distribution in different parts of the target volume. In all cases, the target underwent a 1-dimensional cyclic motion with an amplitude of $\pm$15 mm during the (virtual) irradiation process. A motion in the slow scanning direction (x direction) causes a regular dose pattern with extended areas of over- and underdosage. Due to the large differences in the dose of the single pixels, the homogeneity is small. On the other hand, a motion parallel to the fast scanning direction (y direction) causes a more random dose distribution with small hot and cold spots. From the statistical point of view, the dose deviations are averaged and the homogeneity is larger. If the target moves in z direction, the effect is dominated by the ion's depth dose distribution. In the proximal half of the sphere, a large fraction of the final dose is deposited by pre-irradiation. Therefore the target motion during the irradiation process of a single voxel is averaged over a long time. Consequently, the effect on the dose distribution is small. In all slices more distal than the middle slice, some voxels will receive their dose in one direct irradiation. Therefore, the dose homogeneity in the bottom graph of fig. 4.9 is significantly reduced for all slices in the distal half of the sphere. Due to the plateau region, the depth dose distribution is not point-like but extended, and the

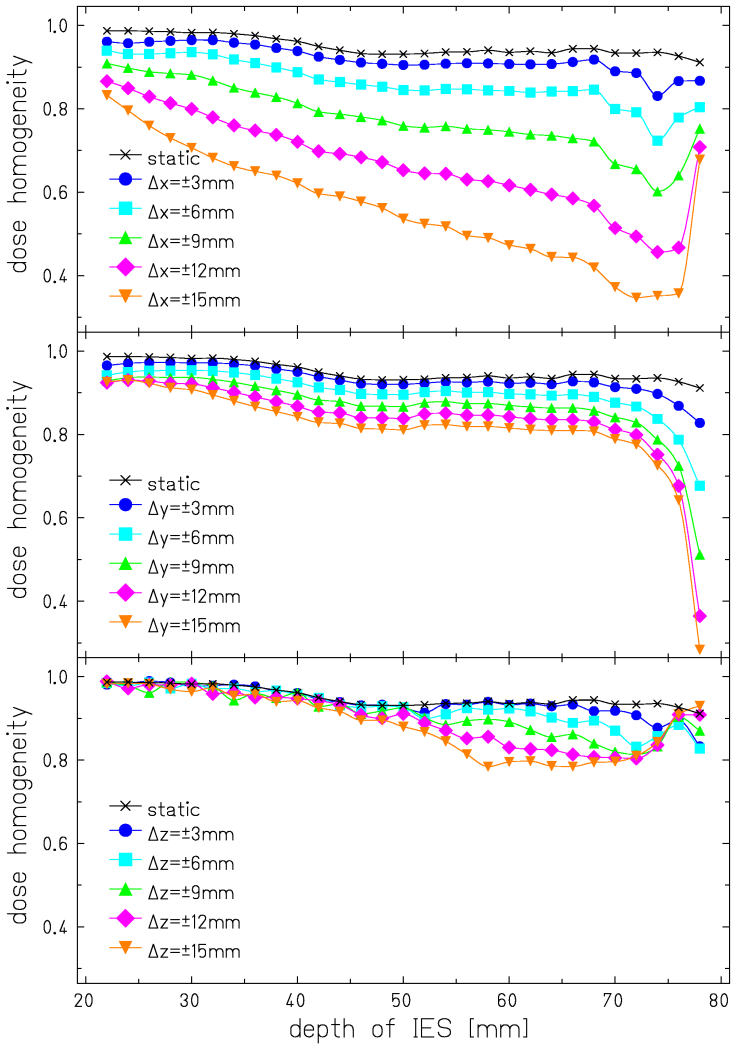

Figure 4.9:
Dose homogeneity for the single IES of a cyclically moving, spherical target volume for different motion amplitudes and directions. For comparison purposes, the dose homogeneity distribution of the resting target volume is added. The target translation in x-direction (top) is parallel to the slow changing component of the beam scanning and in y direction (middle) to the fast one. The z direction (bottom) is parallel to the beam.

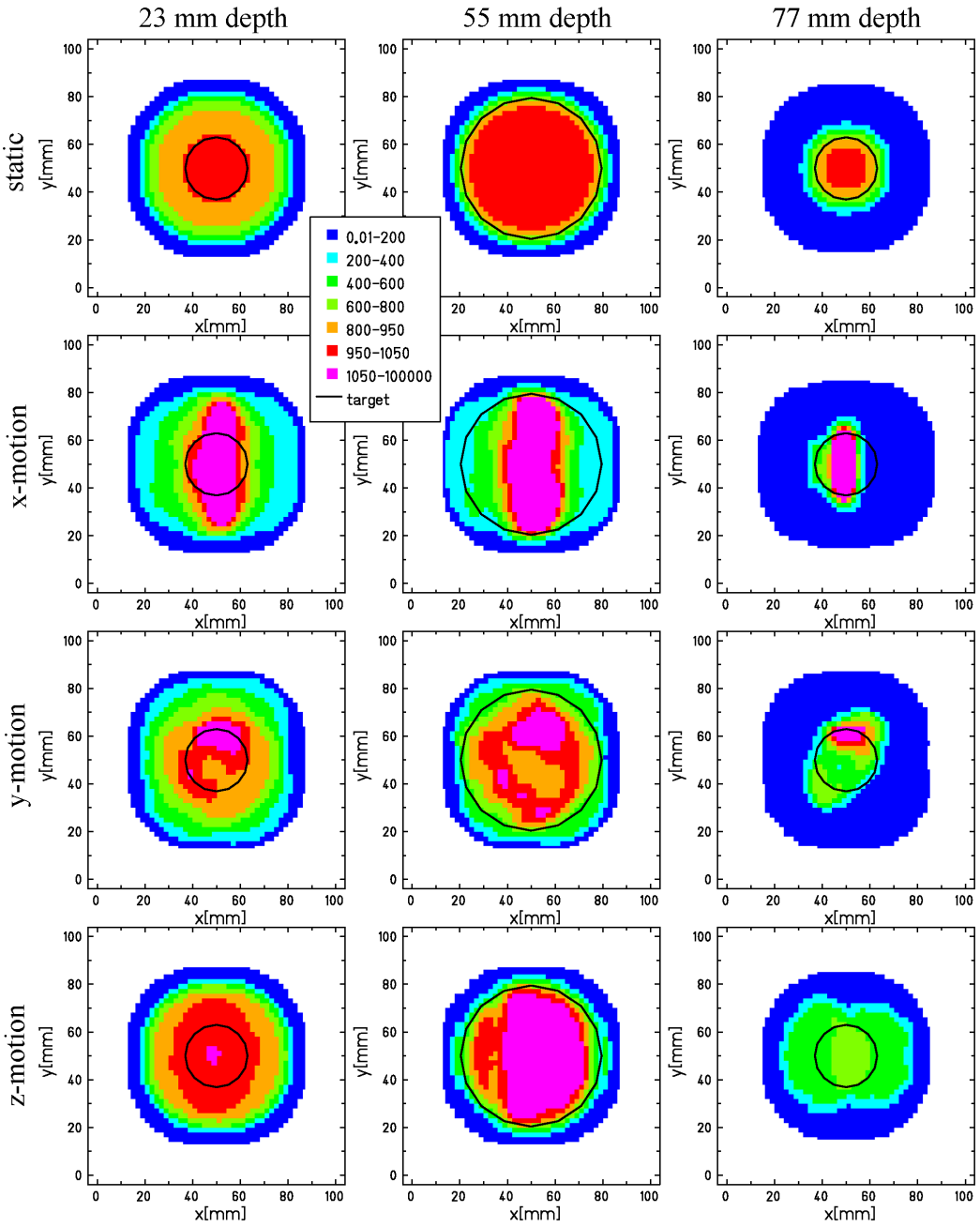

Figure 4.10:
Simulated dose distributions for 1-dimensional cyclic target translation with an amplitude of ±15 mm. The top row shows the reference dose to the static target for the different IES (23 mm, 55 mm and 77 mm depth). The bottom three rows show the dose distribution for a motion in x, y and z direction, respectively. The dose levels are specified in ‰ of the planned dose.

dose is not completely misaligned but blurred. Therefore, the motion-related effect on the dose homogeneity is smaller than for lateral displacements.
In conclusion, the simulations of the dependence of the dose distribution on the motion amplitude show, that for clinically realistic values of 5-15 mm the homogeneity is in all cases significantly reduced. Hot and cold spot regions are created inside the target volume, which would compromise the success of a treatment. In addition, the dose contribution to the tissue outside the target volume is raised in some cases (see for instance bottom left or bottom right picture of fig. 4.10). The strong dependence of the homogeneity on the motion direction can be considered in treatment planning. According to chapter 3.2, respiration-related target motion is large in the superoinferior (s.i.) direction and small in the other two. Therefore, the patient should, if possible, be positioned in such a way, that the s.i. direction does not coincide with the slow scanning direction. The simulations show, that for heavy ion therapy of moving tumour sites, target motion definitely has to be compensated.

Influence of Initial Phase

For a cyclic target motion described by eq. (4.8), a shift in the initial phase corresponds to different motion states at the beginning of the irradiation of the single voxels. In practice, start of the irradiation can be synchronised with the motion, choosing the most favourable phase for the beginning of the irradiation, but since the respiration-related motion is not perfectly regular, the phase correlation will soon be lost.
To estimate the effect of a variation in the initial phase on the dose distribution, the homogeneity inside the target volume was repeatedly calculated for different initial phases Φ. The calculations refer to a target motion amplitude of ± 15 mm in x and ± 5 mm in y and z direction. In contrast to reality, a constant phase correlation was assumed for the whole irradiation process. Fig. 4.11 shows the calculated dose homogeneity as a function of the IES depth for the phase values with the highest and lowest dose homogeneity. In the former cases, the motion-related effect is minimal, corresponding to a destructive interference, while the maximal distortion in the later cases correspond to a constructive interference. As expected from a sinusoidal target motion, the phase difference between the maximum and minimum H_d distribution is approximately $\frac{\pi}{2}$. All other phase values result in H_d distributions in between these two extreme cases. For $\frac{\pi}{2}$ and $\frac{3}{2}\pi$, the absolute displacement values are identical, but the sign is inverted. In case of a static field irradiation, the dose homogeneity would be exactly the same in both cases, since the dose distribution is only mirrored. However, the raster scanning process defines a preference direction and the homogeneity is not invariant under the inversion of the motion direction, anymore.

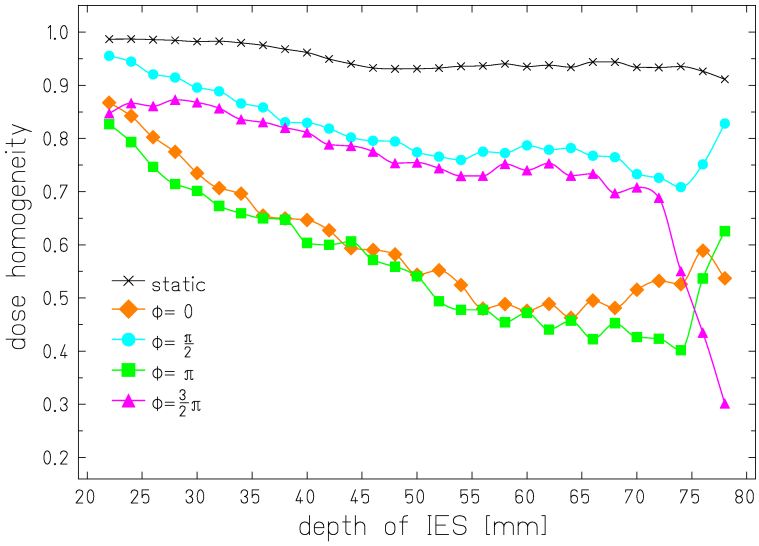

Figure 4.11:
Influence of initial motion phase on the dose homogeneity. The graph includes those phase values, which correspond to the maximum and minimum dose homogeneity distributions. The curves for all other phase values are in between the shown examples. The calculations refer to a cyclic target motion with an amplitude of ±15 in x and ±5 in y and z direction.

The influence of the initial phase (or starting point of the irradiation) has a large effect $(40 - 50\,\%)$ on the dose distribution. Even in the best case, the dose homogeneity in the moving target is in the current example reduced by more than 20 % compared to the static distribution. This large reduction reflects the need for strategies for motion compensation in a clinical application. In addition, a realistic respiration will not be perfectly regular over the irradiation, leading to a superposition of different phases. The dose homogeneity for an initial phase of π represents a worst case estimation for the spherical target volume with a diameter of 60 mm. For practical reasons, a default value of 1.028π is used for the simulations.

Influence of Motion Period

In the same way as the initial phase, the target motion period has a direct influence on the interplay with the scanning motion. The interference between target motion and scanning motion with different frequencies leads to a completely different time correlation and dose distribution for two successive period values.
As expected, fig. 4.12 shows that a change of the motion period has a large effect on the dose distribution. The calculations refer to a cyclical target motion of the spherical target volume with an amplitude of ±15 in x and ±5 mm in y and z

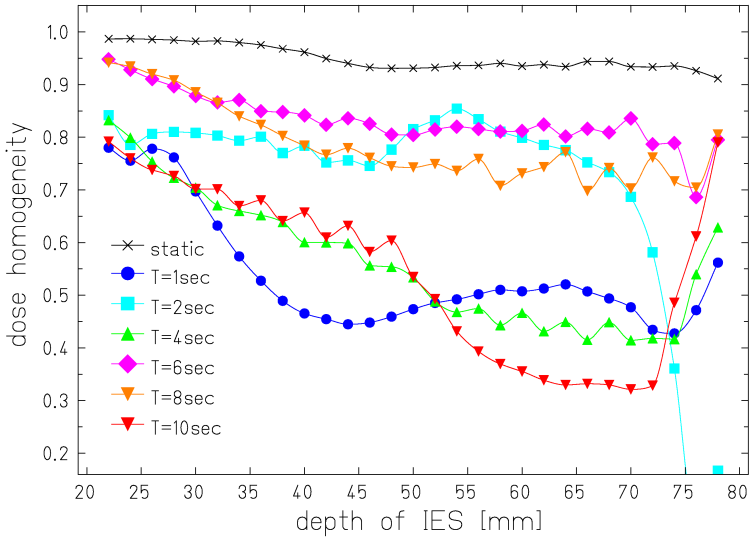

Figure 4.12:
Influence of different motion periods on the dose distribution. The simulations refer to a cyclical target motion with an amplitude of ±15 in x and ±5 in y and z direction.

direction. In contrast to the calculations on the variation of the initial phase, a trend for the dependence on the motion period cannot be extracted. In general, the influence of the motion period is approximately as large as for the initial phase calculations (40−50 %). Except for the most distal part in the T=2 s condition, two bands of resulting dose distributions emerge. These two states correspond to the constructive and destructive interference pattern. Even under the best condition (T=6 s), the dose homogeneity is not tolerable for a clinical application. A motion period of T=4 s represents a smoothed worst case estimation for the spherical target volume with a diameter of 60 mm and is therefore chosen for the study.

4.3.3 Rotation of Target Volume

From the geometrical point of view, any rotation of a position vector can be substituted by a superposition of three orthogonal translations. For an extended target volume, which is divided into discrete volume elements, this fundamental geometrical treatment is not sufficient in all cases, since it does not include the orientation of the voxels. If the target volume rotates around the axes orthogonal to the beam, the orientation of the voxels to the beam changes. In treatment planning the amount of pre-irradiation of proximal voxels has been determined and included into the optimisation of particle occupancies. If the rotation amplitude is large enough, the contribution to the proximal voxels is changed (cf. fig. 4.13).

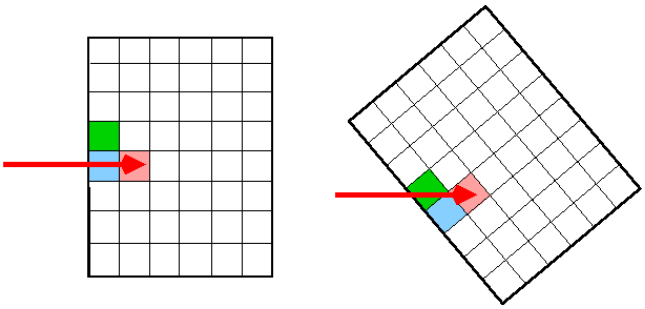

Figure 4.13:
Illustration of the effect of target rotation on the dose contribution to single volume elements. During the irradiation of the red voxel the blue one receives in the static case some dose from the plateau region of the depth dose distribution. Under the assumption that the width of the beam is smaller than the distance to the green voxel, this one does not receive any pre-irradiation. If the target rotation is large enough the green voxel will receive most of the plateau contribution while the blue one receives only a small fraction.

In fig. 4.14 the influence of target rotation on the H_d distribution is shown for rotation angles up to $\pm 20°$. Actually, the target swings (periodical rotation by $\pm X°$) around its axis of rotation. The rotation angle is determined by the same equation (4.8) as the displacement in the translation case, with a rotation amplitude $R_{\vec{e}}$ relative to the direction $\vec{e}$. The upper curves are calculated with the axis of rotation in x and the lower curves in y direction. The rotation around the beam axis can be considered to be a superposition of two translations orthogonal to the beam and is therefore covered in the section about target translation (chapter 4.3.2). The effect of target rotation is small, compared to translation. For the estimated, maximum rotation angle of $\pm 5°$ (cf. chapter 3.2), the reduction in dose homogeneity is almost negligible. For small rotation angles, the effect for x axis rotation is of the same order as for the y axis. This is due to the fact that with the small rotation angles only the directly neighbouring voxels can be affected. Consequently, either the partial dose is misaligned by one voxel, or it is accounted to the right voxel. In case of a one-voxel misalignment, the dose homogeneity is similarly distorted for both directions. Small differences exist due to the orientation of the affected voxel relative to the original one.

For a certain voxel to be irradiated, the proximal and distal voxels, which receive a partial dose via the plateau and tail region of the depth dose distribution, are determined by the beam geometry. Depending on the scanner path, voxels which have already received all of their planned dose might be affected, or a not yet fully irradiated voxel might receive more than the missing dose. Since a retrospective compensation is not possible, the rotation-related distortions cannot be online com-

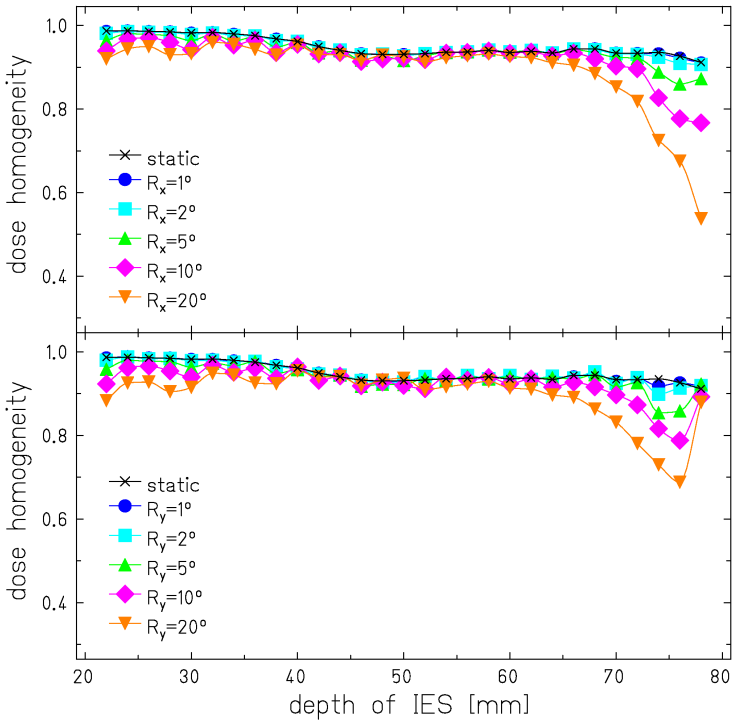

Figure 4.14:
The upper part shows the calculated dose homogeneity for a target rotation around the x axis, while in the lower part the y axis is assumed to be the axis of rotation.

pensated. The simulations showed that the effect can be neglected for a realistic target rotation. If, in practice, a larger target rotation occurred, the influence can only be minimised by scanning the target several times with a fraction of the planned dose (rescanning). The rescanning strategy is described in more detail and discussed with respect to target translation in chapter 4.3.4.

4.3.4 Strategies for Compensation

Rescanning

The large differences in the dose homogeneity for different initial phases (chapter 4.3.2) support the idea of compensating the motion-related distortions by scanning the target volume several times with a reduced dose. For an uncorrelated target motion, the inhomogeneities in the applied dose distribution should average out in the superposition of several uncorrelated scans [e. g. Bor02, Phi92]. For intensity modulated heavy ion therapy, steep dose gradients and an interplay between

beam and target motion result in a very strong phase dependence. Large differences in the final dose distribution can still be found, even after 10 times rescanning.

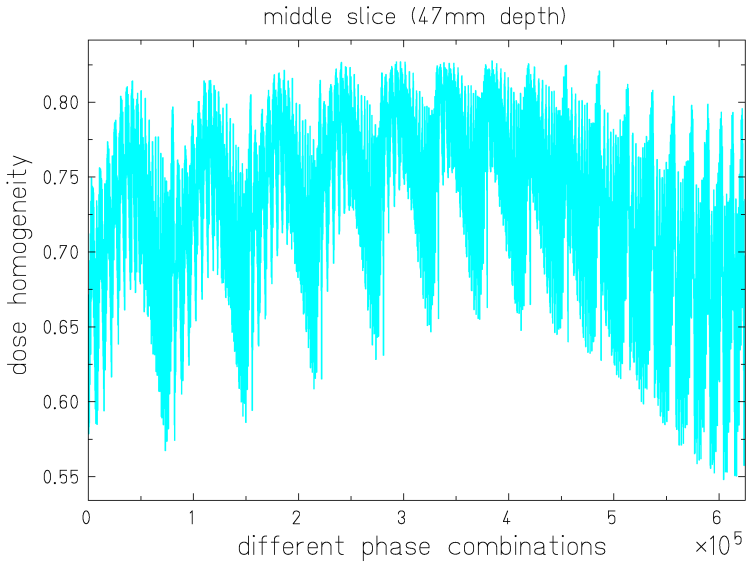

Figure 4.15:
Dose homogeneity of a middle slice (at 47 mm depth) of the 60 mm spherical target volume, moving cyclically with an amplitude of ±(15,5,5) mm, after 10 times rescanning. Dependent on the combination of initial phases of the single scans, the final dose homogeneity differs significantly.

Fig. 4.15 shows exemplarily the dose homogeneity of a middle slice of the 60 mm spherical, moving target volume plotted against the different combinations of the initial phase in the single scans. The calculations refer to a cyclic target motion with an amplitude of ±15 in x and ±5 mm in y and z direction. The dose homogeneity differs over all possible phase combinations by up to 25 %. Although the homogeneity is raised in some cases, other phase combinations are absolutely out of question for a therapeutic application.
Fig. 4.16 shows the dose homogeneity averaged over all phase combinations for different number of scans. As expected, the average is increased by rescanning, but the error bars (statistical standard deviation) reveal that there is no guarantee for a high degree of homogeneity (the treatment might occur with one of the unfavourable phase combinations). In the investigated case, the average dose homogeneity remains far worse than that of a static target, even for 10 times rescanning. This is caused by the finite lateral dose fall-off which is smeared into the target volume and reduces the calculated dose homogeneity over the whole target volume[3]. As

[3]The influence of this dose fall-off on the dose homogeneity is balanced against the dose deposition outside the PTV when planning a patient treatment. The settings used for the simulations and

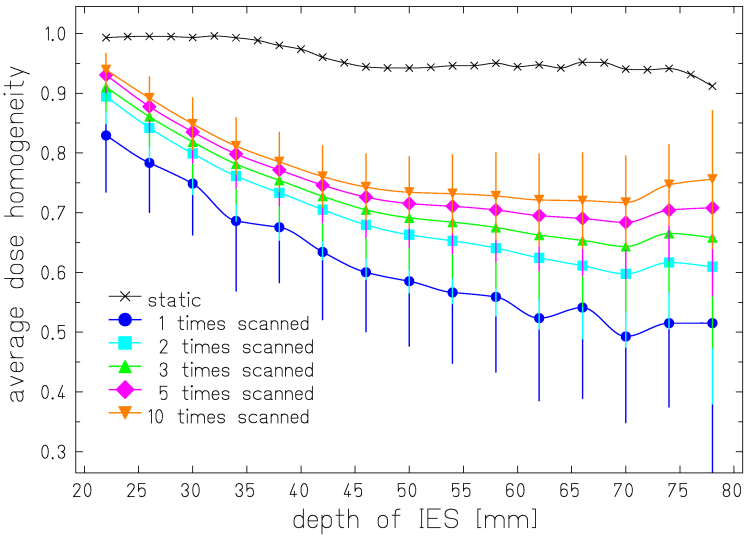

Figure 4.16:
Dose homogeneity for rescanning of a periodically moving target volume. The simulated target motion is cyclic with an amplitude of ±(15,5,0) mm. The integral dose was kept constant for all cases.

shown experimentally in chapter 7.1 the level of dose homogeneity after 10 scans is much higher in a subvolume of the actual target which excludes the influence of the dose fall-off.

Active Motion Compensation

The most direct approach to include target motion in the beam delivery is a compensation of the target displacement at the time of irradiation. In intensity modulated heavy ion therapy, the target volume is irradiated voxel-by-voxel. If the target displacement is measured in real-time, the beam position can be adapted to the actual, 3D target displacement for the irradiation of every single voxel. In the case of a purely translational target motion, the orientation of the single voxels relative to each other remains constant and the compensated dose distribution will be exactly the same as in the static case.
In reality, a perfect compensation is not possible, due to lags in motion monitoring and the accuracy of the beam position compensation. In fig. 4.17 the effect of a normally distributed compensation inaccuracy with a variance σ on the dose homogeneity of the 60 mm spherical target volume, moving cyclically by ±(15,5,5) mm in x, y and z direction respectively, is investigated. Up to a total error (displacement

experiments in this thesis causes a larger reduction in the dose homogeneity than contribution to the outside of the target boundary.

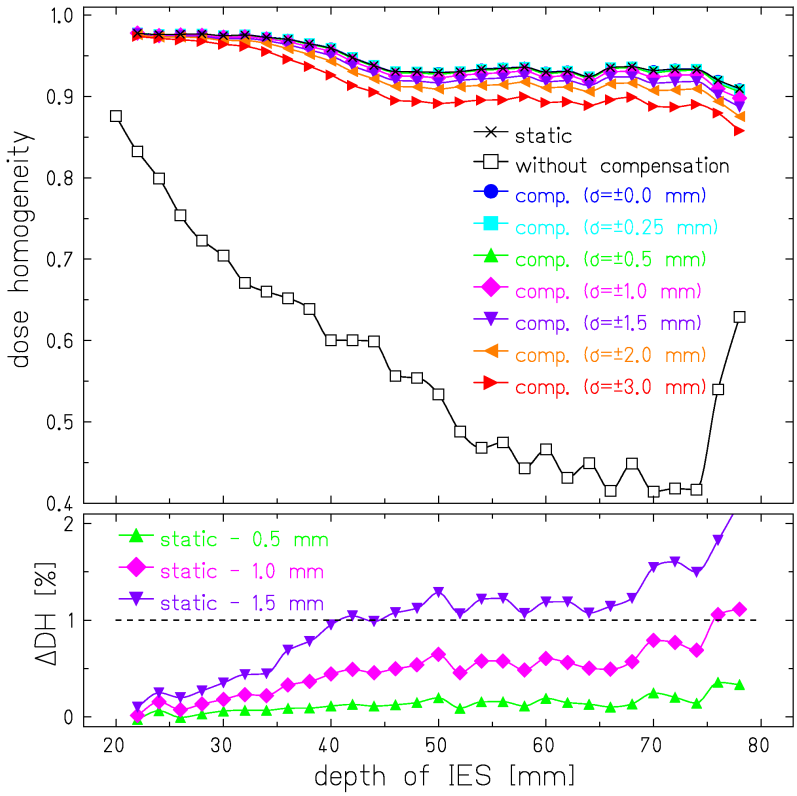

Figure 4.17:
Potential of active motion compensation at runtime, for different technical accuracies. The calculations refer to a 60 mm spherical target, moving cyclically with an amplitude of ±(15,5,5) mm. To account for potential compensation inaccuracies, the actual motion compensation is assumed to be normally distributed with a variance σ around the target displacement. The deviation to the statistic distribution is plotted for three accuracy levels in the bottom part.

measurement and beam positioning) of 0.5 mm the difference of the resulting dose homogeneity to the static case is negligible. The lower part of fig. 4.17 shows the difference of the homogeneity to the static case for three different accuracy levels. For σ=0.5 mm the difference is smaller than 0.5 % over the whole target volume. A technical accuracy of 1 mm leads to a deviation of approximately 1 % in the very distal slices. For larger inaccuracies, the dose homogeneity differs by more than 2 % in parts of the target volume. An active motion compensation system with sub-millimetre precision could deliver a conformal treatment plan to a translating target volume with almost the same quality as to a static one.
In principle, active motion compensation is not suited to compensate the effect of target rotation. Fig. 4.18 shows the simulated dose distribution for a target

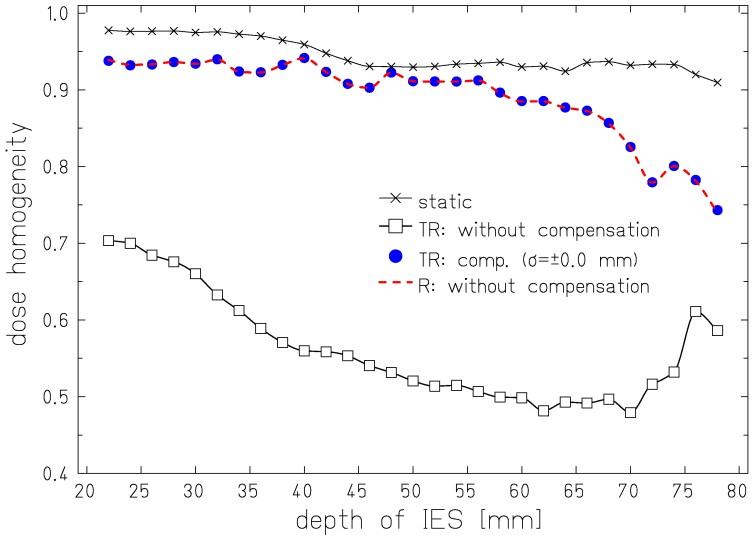

Figure 4.18:
Simulated dose homogeneity distribution for a target undergoing a cyclic target translation with an amplitude of ±(15,5,5) mm and superimposed rotation by ±20° (TR). Due to the change in voxel orientation, even an absolutely accurate active motion compensation cannot restore the static dose homogeneity. The remaining inhomogeneity corresponds to the contribution from the target rotation, only (R).

translation with an amplitude of ±(15,5,5) mm and a superimposed rotation with an amplitude of ±20° . The large rotation amplitude of ±20° was chosen for a worst-case estimation, since the effect of a small, realistic target rotation can be neglected (cf. chapter 4.3.3). Even with perfect accuracy, the active motion compensation cannot restore the dose homogeneity of the static case. A comparison with the simulated effect of a pure target rotation by ±20° reveals that the remaining difference corresponds to the contribution of the rotation. This contribution results from changes in the relative voxel orientation and can only be averaged out by rescanning (cf. chapter 4.3.4). In this case, rescanning can be successful, since the remaining effect, and thus the phase dependent variation, is small. The parallel active motion compensation of the large, translation-related interference constrains the dose into the target and its direct vicinity, only. A combination of both strategies will maximise the dose homogeneity and minimise the contribution to the healthy tissue for targets undergoing a large rotation.

Chapter 5

A Motion Compensation System for Heavy Ion Therapy

5.1 Motion Adapted Heavy Ion Therapy

Due to the high dynamics, geometrical precision and flexibility of beam delivery, intensity modulated heavy ion therapy is extremely well suited for online motion compensation. The sharp, spatial localisation of the dose deposition in the Bragg-peak enables the sub-division of the target volume into small volume elements (voxels), which are irradiated consecutively with a pre-defined number of ions. The key issue is the precise knowledge of the absolute voxel position with respect to the beam, presently achieved by a rigid patient fixation in the coordinate system of the treatment room. This method works only, if the target volume is not moving inside of the patient. For an expansion of heavy ion therapy to moving targets, three issues have to be addressed (cf. fig. 5.1).
The first task is the modification of the beam delivery system to dynamically adapt the position of the therapy beam to a time dependent target motion offset. Changes in orientation of the internal structures require a modification of the static planning data set. Since re-calculation of the treatment plan is too time consuming (several hours to half a day [Krä]) to determine the required modifications in real-time, strategies for including these changes in the treatment planning process have to be developed. Finally, a precise, real-time tracking of target motion during the treatment session is essential. The following paragraphs provide short problem definitions for all three issues.

Motion Adapted Beam Delivery

In contrast to the relatively compact electron linear accelerators used to generate photon beams for conventional therapy and IMRT, the accelerators required for charged particle therapy are much too large to be moved in space. In the dedicated cancer therapy centre in Heidelberg the ions will, for instance, be accelerated in a synchrotron measuring approximately 63 m in circumference [Deb98] and guided to

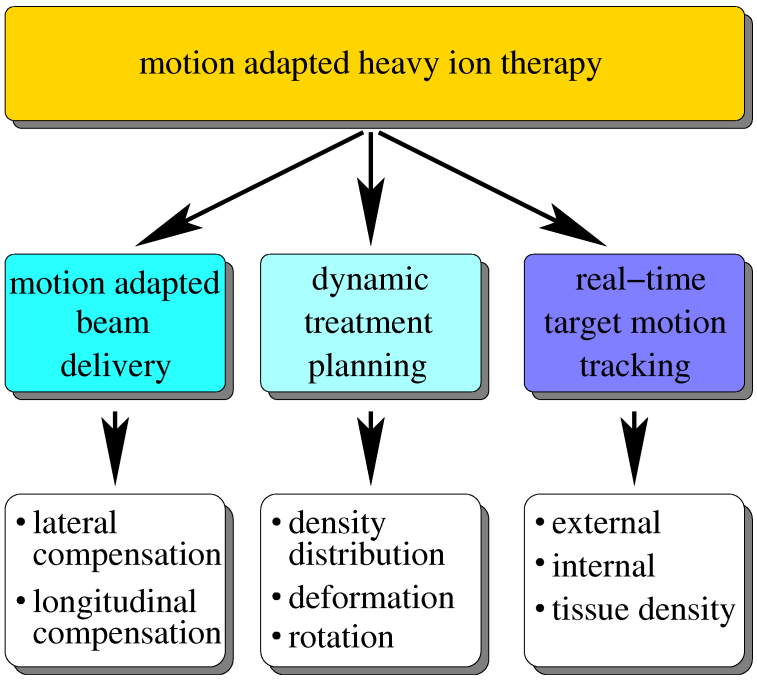

Figure 5.1:
The project of motion adapted heavy ion therapy has to deal with three disjoint problems: The beam delivery system has to be modified to adapt the beam position online, the motion of internal structures relative to each other has to be included into the treatment planning process and the motion of the target as well as neighbouring structures has to be monitored in real-time.

the treatment rooms in long beam transfer lines. Motion compensation strategies as in photon therapy adapting the accelerator position with a robotic arm to the target displacement [Sch93c] are beyond question for charged particle therapy. The most obvious solution would be a movable beam transfer line around the patient. But in design studies for a heavy ion gantry at the Heidelberg facility, planned to expand the range of irradiation field positions for the patient treatment, a weight of about 600 t was estimated for such a device [Spi00]. This weight is far too high for position changes on a millisecond basis. Proposed solution of synchronous movement of the treatment couch to compensate for the target displacement [e. g. Mac03] are difficult to realise due to spatial restrictions around the patient (e. g. by the heads of the PET camera which are positioned as close as possible to the patient during the treatment in order to improve the signal-to-noise ratio). Moreover, fast changes in couch position might induce additional target motion.
A practical solution is provided by the active beam delivery. The dynamic deflection of a narrow pencil beam allows the deposition of charged particles in a pre-defined

number to single volume elements of the target volume. The amount of deflection can be modified simply by adjusting the electric currents in the magnets. As long as the maximum scanning velocity exceeds the velocity of the target motion, displacements in the plane orthogonal to the beam can be compensated by the active beam delivery system. The penetration depth (range) of the beam depends on the ion energy. By altering the initial energy, adaption of the particle range to a longitudinal displacement, as well as to changes in the proximal density distribution can be achieved. In this way, the three dimensional position of the Bragg-peak can be matched to the actual water-equivalent (WE) location of each volume element at the time of its irradiation [GSI00]. A prototype setup combining both lateral and longitudinal motion compensation was realised in the course of this thesis. The detailed concept and design are described in section 5.2.

Dynamic Treatment Planning

The main goal of online motion compensation is the exact dose delivery to planned volume elements, independent of the target motion. Ideally, the energy deposition would be restricted to the Bragg peak region. In this case the depth dose distribution would have a Gaussian shape and the complete dose of the ion beam would be deposited in a single voxel. In reality, the depth dose distribution of an ion beam shows a pronounced plateau in front of the peak and a small tail behind (cf. fig. 5.2). These two regions contribute to the final dose of neighbouring volume elements. For a static target, the entrance and tail dose contributions are included in treatment planning by correcting the planned number of ions for each affected voxel. In the case of changes of the relative voxel orientation, as e. g. in the case of deformation or target rotation, these corrections have to be adapted. As mentioned above, a re-calculation of the treatment plan in real-time is impossible. Therefore, strategies have to be developed to calculate the effect of the measured displacement on the treatment parameters in advance. The issue of dynamic treatment planning is not a subject of this thesis, it is currently investigated in a follow-up study.

Online Motion Tracking

The strategy of online motion compensation depends essentially on a fast and precise motion tracking system. To achieve a high precision in the compensation, this tracking system has to provide real-time motion information. The simulations presented in chapter 4 recommend a maximum error in the online motion compensation process of $\pm 1\,\mathrm{mm}$. Assuming a periodical motion with a maximum amplitude of $\pm 15\,\mathrm{mm}$, the target volume moves a total of 60 mm in a full breathing cycle of approximately 4 s, yielding an average velocity of $15\,\frac{\mathrm{mm}}{\mathrm{sec}}$. To obtain a precision of 1 mm in the motion tracking process, the full set of relevant information has to be available every 66 ms (15 Hz). Considering the finite accuracy ($\approx 0.5\,\mathrm{mm}$) of the

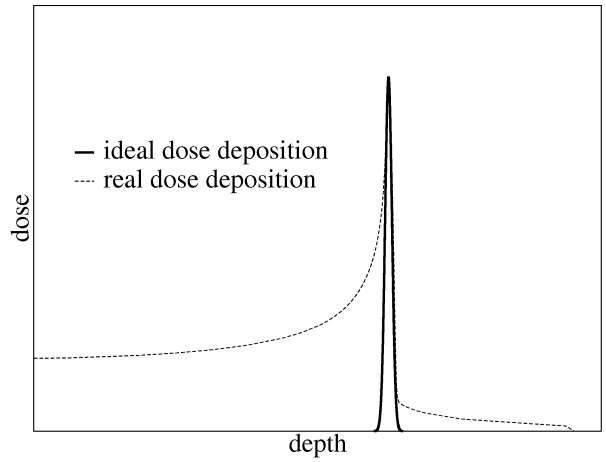

Figure 5.2:
In case of a Gaussian energy deposition, a perfect online motion compensation would be possible. In reality, the depth dose distribution of an ion beam shows a pronounced plateau in front of the peak and a tail behind. This contribution to neighbouring voxels is included in the treatment planning, but as soon as the relative position of the voxels is altered by target motion, the treatment planning conditions are not valid anymore.

dynamic beam delivery process (cf. chapter 7), the required tracking frequency is increased to about 30 Hz. The intrinsic accuracy of the motion tracking requires an even higher time-resolution. Apart from the 3D target displacement, the rotation angle and the proximal density distribution have to be measured, as well.
As discussed in chapter 3.3, various strategies for tracking internal tumour motion have been studied all over the world. Most of the existing strategies do not meet the requirements for motion adapted heavy ion therapy, which can be summarised as:

- a high spatial resolution in all three dimensions (has to be added to the intrinsic error of the dynamic beam delivery of ≈ 0.5 mm and will reduce the compensation efficiency)
- a high time resolution (> 30 Hz to keep the intrinsic motion compensation error below 1 mm)
- providing information on translation, rotation and density distribution
- feasibility for a long-term application (more than 10^4 s per patient)
- compact setup around the patient
- compatibility with magnetic raster scanning (insensitivity to magnetic stray fields and radiation)

Selecting a suitable motion tracking method is not a subject of this thesis. A more detailed, technical analysis has to follow.

5.2 Prototype Setup for Motion Adapted Beam Delivery

In the framework of this thesis a prototype setup for 3-dimensional correction of the beam position in real-time was developed, committed and tested. This setup realises motion adapted delivery of scanned ion beams. With online motion compensation the irradiation of moving phantoms with arbitrary patterns yielded dose distributions corresponding to the expectations for static targets.

The lateral position of a scanned particle beam is determined by the amount of beam deflection induced by the scanning magnets. In principle, the beam can follow the voxel to be irradiated, as long as the target motion is significantly slower than the maximum scanning speed of the magnets [Kra03]. The maximum scanning velocity of the deflection magnets used at GSI is 11 $\frac{\mathrm{m}}{\mathrm{s}}$ for the maximum beam rigidity of 8 Tm and up to 30 $\frac{\mathrm{m}}{\mathrm{s}}$ for the lowest energies [Hab93]. Assuming a sinusoidal target motion with 15 mm amplitude and a frequency of 0.25 Hz the maximum target velocity will be 23.6 $\frac{\mathrm{mm}}{\mathrm{s}}$, i. e. roughly a factor of 500 slower than the capability of the raster scanner. Even for the $15 - 20$ times faster vascular pulsation the condition $v_{target} < v_{scan}$ is still fulfilled. Consequently, the existing scanning system of CaveM could be expanded to perform lateral motion compensation.

Per definition, the longitudinal motion can not be compensated by the lateral scanning control system. In general, a modification of the ion range can be achieved according to eq. (2.5) by changing the initial particle energy T_0. But at GSI it is not possible to change the particle energy delivered by the synchrotron during the beam extraction, i. e. within one spill. In the current operation mode for therapy, the spill repetition time of the synchrotron is approximately 5 s, consisting of extraction of the beam over approximately 2 s, refilling of the synchrotron and acceleration of the particles. Energy variations on a smaller time scale have to be applied after beam extraction. The most direct approach would be to insert an additional linear accelerator structure in the beam transfer line between synchrotron and treatment room to actively accelerate or decelerate the ions in an electric field. To shift the range of ^{12}C ions with a medium initial energy for therapy of 200 $\frac{\mathrm{MeV}}{\mathrm{u}}$ by 2 cm, the energy has to be adapted by approximately ± 26 $\frac{\mathrm{MeV}}{\mathrm{u}}$. The technique of the injector stage at the dedicated cancer therapy centre in Heidelberg [Deb98], for instance, would require a structure of approximately 31 m in length, which is about half the planned synchrotron circumference. In addition, the acceleration parameters have to be adapted to the changes in water-equivalent path length (WEL) with a frequency of approximately 30 Hz (every 33 ms). The development of such a fast and

compact (low construction costs) acceleration structure would require an enormous effort. Since active energy variation is not possible with justifiable effort, the energy is passively modulated in the prototype setup for 3D online motion compensation.

5.2.1 Fast Range Modulation

In the prototype setup, fast, passive range modulation is achieved by a set of plexiglass wedges mounted on a linear hybrid stepping motor. Plexiglas wedges are a common tool for field shaping in radiation therapy, but are for the first time mounted dynamically on a linear motor to achieve fast, passive energy modulation [GSI99]. The same principle was initially used for depth scanning [Web00]. Fig. 5.3 shows the main components of the wedge drive, consisting of two blocks with five PMMA wedges each, which are mounted face-to-face with overlapping tips on the two slides of the motor. To increase the performance, the slides glide on a thin

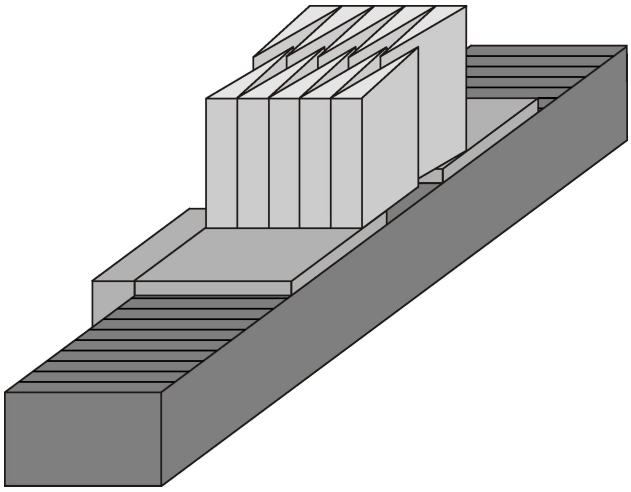

Figure 5.3:
Schematic drawing of the wedge drive system used as fast, passive energy modulator. Two blocks of five wedges each are mounted on two slides of a linear hybrid stepping motor. Moving the two slides relative to each other, the PMMA thickness in the overlap region can be adapted.

air cushion. The position of each slide is permanently verified by an optical linear encoder. By changing the relative distance between the two blocks the region of overlap is modified and thereby energy modulation proportional to the difference in thickness of PMMA is achieved.
Using one block of wedges for the energy modulation would require a large opening angle, causing, due to the finite beam width, a significant broadening of the Bragg peak. To avoid distortion of the beam, two opposing wedges are used, adding

together to a rectangular block. Assuming an overlap region (active area) wider than the beam, a fast depth modification is achieved without large effect on the beam.

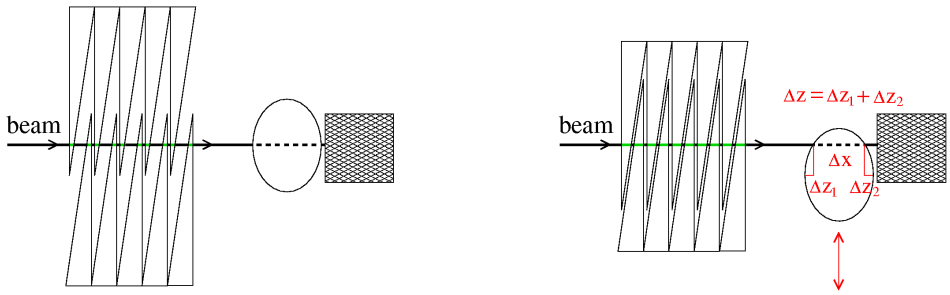

Figure 5.4:
Principle of the depth correction using a dynamic wedge drive. The displacement Δx causes a change Δz in the thickness of the structure penetrated by the beam in front of the target (hatched area). This would lead to a change in ion range which is compensated by adjusting the amount of wedge material the beam has to pass.

Fig. 5.4 shows the principle of longitudinal motion compensation at the example of a relative motion of internal structures. The white sphere represents a dense structure (e. g. a bone) in front of the hatched target volume. As the total WEL of material in front of the target is reduced, the ions will travel too far, causing an undesirable dose deposition behind the target. The difference in material can be compensated by moving the wedges closer together. To allow equal compensation in both directions, the reference position for zero compensation was set to half the maximum amount of PMMA thickness. This additional offset, as well as additional scattering and fragmentation of the PMMA on has to be included in the treatment planning.

Technical Realisation

The power supply and amplification unit of the wedge drive is connected to a PC by a Parker[1] AT6400 four axes step and direction controller. The longitudinal target displacement is received via TCP/IP and converted into a relative distance of the wedges according to the geometrical considerations in appendix D. The relative distance and the information about the vertical beam deflection are finally converted into an absolute position for each of the slides. This position is passed to the AT6400, which automatically generates the step and direction signals for

[1]Parker Hannifin Corporation, Ohio (USA)

the stepping motor electronics. In the current setup, a feedback loop with optical encoders gains a precision of $\pm 10\,\mu$m for the final position of each slide after several iteration steps. The control software running on the PC under the LabVIEW[2] environment is described in more detail in appendix E.2.
The mechanical performance of the wedge drive has earlier been optimised to the irradiation conditions at GSI [Web00]. Tab. 5.1 summarises the main properties of the wedge drive system.

positioning precision	$\approx 20\,\mu$m
maximum velocity	$2\,\mathrm{ms}^{-1}$
maximum acceleration (loaded)	$\approx 25\,\mathrm{ms}^{-2} \sim 2.5\,\mathrm{g}$

Table 5.1: Mechanical properties of the wedge drive system

5.2.2 Lateral Motion Compensation

To compensate lateral target motion components, the existing magnetic raster scanning system was adapted. To include an externally measured target displacement into the beam positioning routine, changes of the scanning control unit (SCU) on a pure software basis were required.
During irradiation of static targets the measured beam position (derived from MWPC signal) is compared with the planned coordinates from the treatment plan every $150\,\mu$s. A deviation between both values leads to an automatic realignment by a feedback loop with the scanning magnets. For moving targets, an external offset, corresponding to the actual lateral displacement, is added to the planned beam position and the feedback loop will automatically adapt the beam position to the new position.
The details of the changes in the source code of the control programs are given in appendix E.1.

Expansion of Scanning Control System

Due to safety reasons, no access to the data loaded into the memory of the existing scanning control system is possible, after the irradiation has been started (cf. chapter 2.4.1). The only exception is a small shared memory block (SMB), originally reserved for debugging information, which is open to read/write access from both sides during the irradiation. In the prototype setup for 3D online motion compensation (3D-OMC) the first 10 bytes of this SMB are used to exchange the data for motion compensation at runtime. During the irradiation, the x and

[2]National Instruments Corporation, Austin (USA)

y offset in this memory block are regularly updated with the externally measured, lateral displacement information (in units of 0.1 mm). In each cycle of the position verification the SCU adds these offsets to the target position from the treatment plan and uses the result of this operation for the verification of the beam position. To guarantee the consistency of the data, one byte of the shared memory is used as read/write access flag, prohibiting read access while the data is updated and vice versa. For safety reasons, the current prototype setup accepts a maximum target displacement of ±30 mm for compensation.

5.2.3 3D Motion Compensation

To compensate target motion in all three dimensions, the beam position has to be corrected in lateral and longitudinal direction simultaneously. Fig. 5.5 shows a typical setup for 3D motion compensation with the lateral correction achieved upstream by the scanning magnets and the energy modulation directly in front of the patient. This way, the lateral beam deflection is not influenced by the

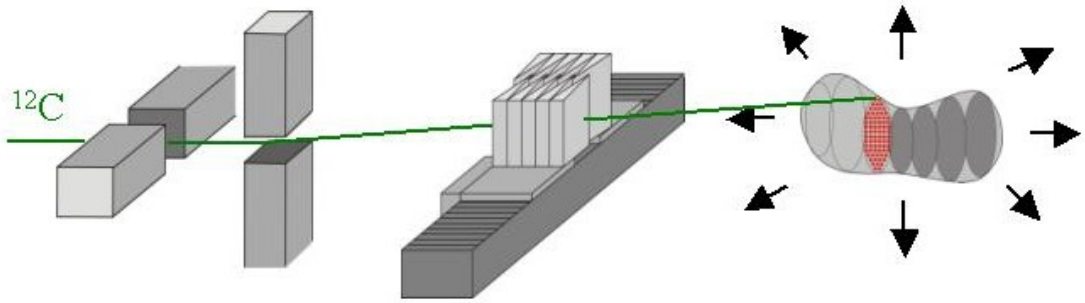

Figure 5.5:
For a 3D motion compensation two compensation strategies have to be combined. Lateral components are compensated by the deflection magnets of the raster scanner and at the same time a fast passive energy modulator deals with longitudinal motion.

passive energy modulation. The operation of the wedge drive, however, depends on the dynamics of the scanning process. The prototype setup of the wedge drive supports an active area with a width d of 10 mm$< d <$110 mm, limited in the lower case by the maximum width of the ^{12}C beam used for therapy (nominal 8.8 mm according to the treatment planning database)[3]. To avoid distortions of the depth

[3]If larger beam spots are known to occur, the parameter for the minimum width of the active area can be adapted in the control system of the wedge drive. The range of motion compensation is then reduced according to the new setting.

dose profile the beam always has to pass through the active area in the centre of the wedge system. Consequently, the centre of the wedge system has to be adapted to the amount of beam deflection. The magnetic raster scanning system supports a maximum beam deflection of ±200 mm.
The vertical and horizontal scanning magnets are located 7.800 and 8.826 m upstream of the treatment reference point (isocentre) [Hab], leading to a quasi-parallel beam orientation over the complete scanning range. Therefore, a correction of the PMMA thickness due to diagonal beam passage is not required.
The irradiation time for one point is in the order of milliseconds [Kra00]. This rate would require extremely high dynamics of the drive for shifting the system centre. The raster scanner at GSI preferentially moves in horizontal lines. By scanning in vertical direction, the irradiation of a full line without shifting the wedge centre is possible. A corresponding scanning path optimisation algorithm, labelled *tm*, was added to the treatment planning software TRiP98. If not stated otherwise, all experiments and calculations in this thesis are performed under the conditions of this new path optimisation.

Technical Realisation

As a consequence of the ongoing patient irradiation in CaveM, the prototype setup for motion compensation has not been included into the interlock management and data flow of the therapy control system, yet. A closed system was designed without the need of additional I/O ports in the scanning control unit.
Fig. 5.6 shows the typical setup used for the feasibility experiments. Collecting, pre-processing and distributing the data relevant for motion compensation was performed by a VME-based master processor (E7). In the experiments, the motion information was obtained from rotary encoders connected to a CAMAC interface card. The E7 directly accessed the displacement data via a VSC[4] interface. The x and y displacement components were transferred via VME bus into a dedicated memory block of the control module responsible for the scanning magnets (SAM S). To correlate the wedge drive system to the scanning procedure, the actual beam position was passed back to the E7. Finally, the z displacement information and the corrected x position of the beam were transferred via ethernet to the wedge drive control.
As it will be shown in chapter 7, the prototype setup is able to compensate for arbitrary target motion in any of the three directions with sub-millimetre precision. Without loss of generality, the experiments purely relied on mechanically measured target motion with rotary encoders. However, the flexible design of the interface to the motion compensation system allows the inclusion of any kind of motion tracking without major changes. After some method specific pre-processing of the measured

[4]VSB to differential cable, extension of VME subsystem bus (VSB) to connect remote hardware

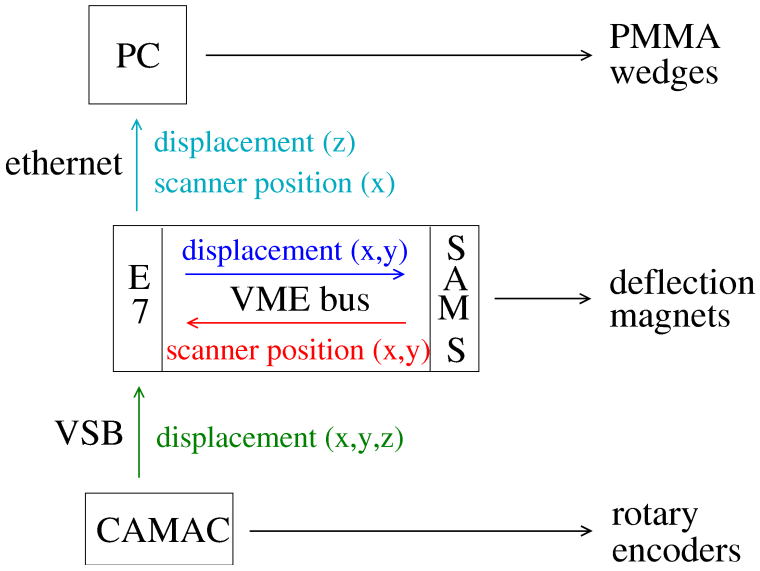

Figure 5.6:
Overview on the components of the prototype setup for online motion compensation and the data transfer between those. A VME computer (E7) is operating as master for all other components. It gets the displacement information from rotary encoders via CAMAC, converts the encoder values into lengths and distributes these to the single components. In order to adapt the reference point of the wedge drive to the horizontal scanning motion, the actual scanner position is reported back from the scanning control module (SAM S).

data, any tracking system can pass the required parameters (3D-displacement[5] and rotation vector) to the E7. In this case, the dedicated VSC connection from the tracking sensor system (CAMAC) to the E7 has to be replaced by a suitable communication protocol (e. g. TCP/IP).

[5]Changes in density distribution can already be included into the z-component at the stage of pre-processing.

Chapter 6

Experimental Means and General Sources of Errors

The design of the prototype setup for three-dimensional online motion compensation (3D-OMC) in chapter 5 is based on simulations of the motion-related effect on the applied dose distributions (cf. chapter 4). To verify the design, the online compensation performance was studied experimentally. In preparation of the feasibility study, presented in chapter 7, the current section describes the experimental means for simulating target motion and the detectors used for verifying the applied dose distribution. The relevant sources of experimental errors are discussed as well.

6.1 Inducing Target Motion

Many kinds of target motion, like respiration, heart-beat, patient displacement etc., can be compensated by 3D-OMC. The current study focuses on respiration-related target motion. Breathing causes a slow, cyclic motion with significant amplitude. The clinical parameters for respiration-related target motion are discussed in more detail in chapter 3.2.

Any cyclic function is represented by a superposition of trigonometric functions with different periods and phases. Consequently, periodical target motion can be approximated by a sinusoidal relation

$$x(t) = A \cdot \sin\left(2\pi\frac{t}{T} + \Phi\right) \tag{6.1}$$

with amplitude A, period T and initial phase Φ.

During the breathing cycle the lung expands in all directions, the inflation reaches a maximum and then the lung contracts in all three dimension. The resulting motion is strongly correlated in time over all three dimensions. In this thesis, 3D respiration-related target motion is approximated by a linear combination of

sinusoidal motion components along all three axes ($\vec{e}_i$) with the same period (T_0) and initial phase (Φ_0)

$$\vec{r}(t) = \sum_{i=1}^{3} A_i \cdot \sin\left(2\pi \frac{t}{T_0} + \Phi_0\right) \cdot \vec{e}_i \tag{6.2}$$

6.1.1 Lateral Motion

In the experiments of the feasibility study, lateral target motion was induced by a 3D positioning table. This setup consists of three orthogonal, stepping motor driven axes with an object table mounted on the third axis. The motion of each of the axes is PC controlled via profibus connection. The position of the object table is measured by rotary encoders attached to each of the axes. The data from these encoders is read-out by a dedicated CAMAC module. This setup is schematically shown in fig. 6.1.

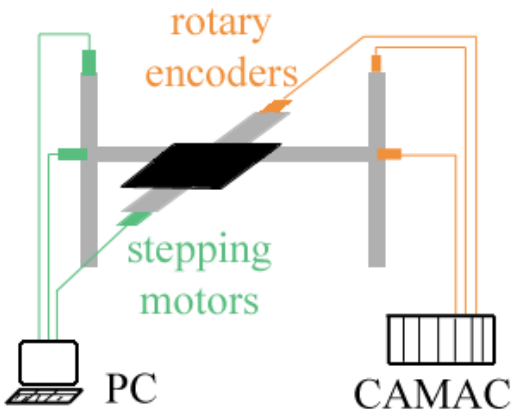

Figure 6.1:
Schematic setup of the 3D positioning table inducing lateral target motion for the experimental study. The setup consists of three orthogonal stepping motor driven axes. The motion of the single axes is PC controlled. The actual position of the object table is measured by rotary encoders attached to each of the axes. The encoder signal is read-out via a dedicated CAMAC interface.

For simulation of a periodical target motion each of the three axes was permanently moved in accelerated mode between two defined positions (P_1 and P_2). The drive started to accelerate from the starting point (P_1) until it reached a maximum velocity. With this velocity it moved until shortly before the final point (P_2) and decelerated until P_2 was reached. Next, the previous starting point (P_1) was set as new position and the motion was started with the same pattern. When P_1 was

reached, one motion cycle was completed. The reference point for calculating the displacement was the centre position between P_1 and P_2 yielding a symmetrical displacement around zero. In the experiment, the drive parameters were adjusted corresponding to respiration-related organ motion.

Fig. 6.2 shows two excerpts of a measured, lateral motion signal of the 3D positioning table. From the technical point of view, the performance of the drive is far from being perfect. The motion pattern of all axes is periodical (top figure), temporarily interrupted by distortions in the communication between controller and the axes (bottom figure). Due to technical limitations of the controller a time lag for the initiation of the motion between both axes exists. For the two lateral axes, this time lag is approximately 1 s. At the first glance, these limitations seem to distort the feasibility experiments. On the other hand, the unpredictability of the motion pattern and the missing correlation between both axes are perfect conditions to test the performance of the 3D-OMC system under realistic conditions. The actual displacement in each dimension is permanently verified. The position verification is achieved with rotary encoders operating independently of the drive control. In this way, the actual position of each of the axes can precisely be determined at any time, independent of the status of the drive.

6.1.2 Longitudinal Motion

The 3D positioning table allows to move objects on arbitrary patterns through the air. Due to the reduced atomic density of air (about a factor 1000 less dense than water), the relative change in WEL for a movement parallel to the beam can be neglected and the setup is only feasible to induce lateral target motion.

In the human body longitudinal translation of a deep seated target volume is directly transferred to the proximal tissue, including the body surface. In analogy to the 3D positioning table, the influence of longitudinal organ motion is expected to be small in the clinical case. Variations in the density distribution of the proximal tissue (e. g. compression by bones or expansion like the inflating lung tissue), having a direct impact on the WEL and requiring compensation, are much more likely to occur[1]. The study of longitudinal compensation performance of the 3D-OMC system concentrated on density changes. In a first approximation a change in the proximal density distribution was simulated by modifying the initial beam energy (active energy variation). Reducing the beam energy corresponds to a higher loss of energy in front of the target and thus a larger WEL. In a second approach a dense object (water filled ball) was placed in front of the target volume, changing its extension in longitudinal direction and thus varying the actual amount of penetrated matter.

[1] Clinical data suggests that, in general, the tumour itself is hardly compressed [Rie].

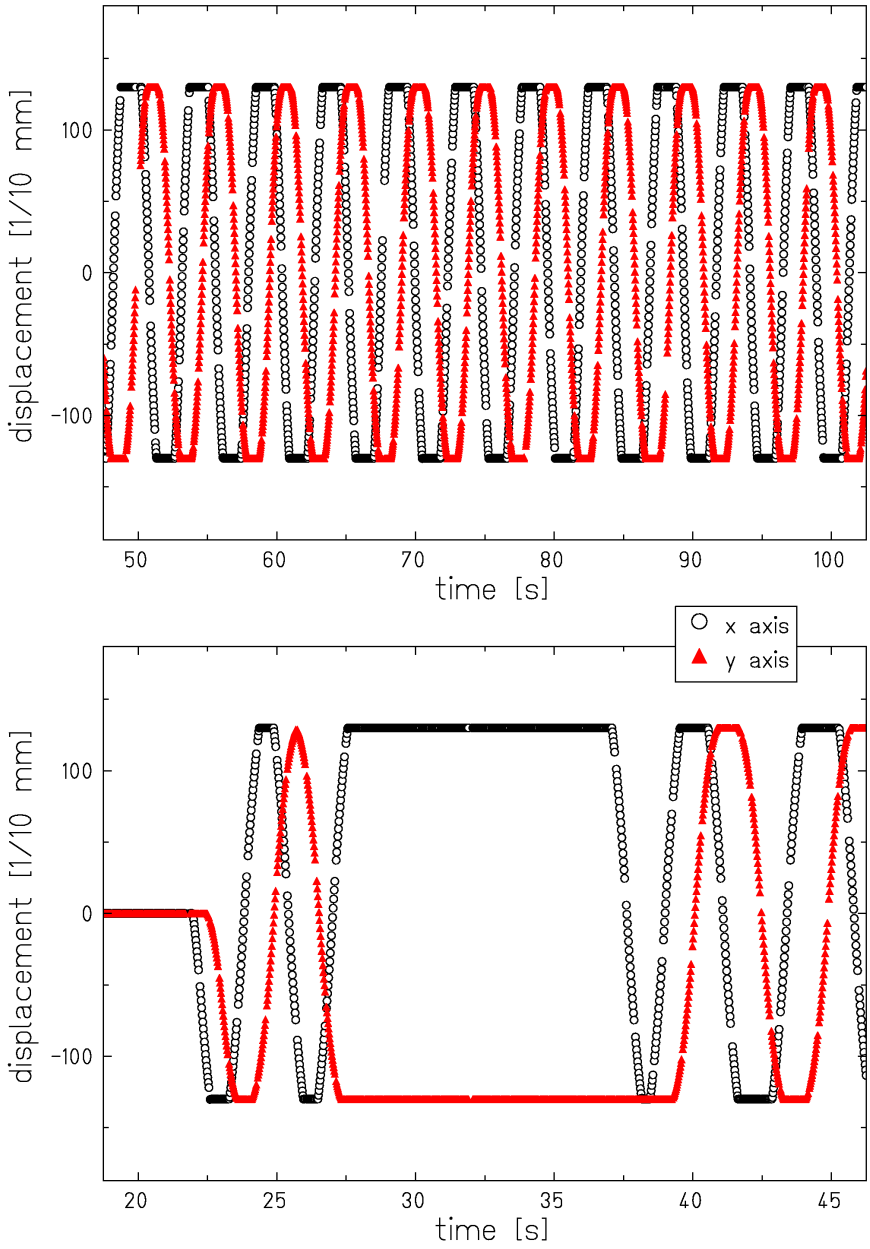

Figure 6.2:
The graphs show excerpts from a measured target motion signal at two different time points. The motion is mostly periodical (upper figure). Temporarily, the communication between drive and controller fails (lower figure). These failures enable a reliable verification of the performance of the 3D-OMC system. Due to technical limitations, the time lag between the start of motion for the two axes is approximately 1 s.

Active Energy Variation

One of the major requirements for the fully active beam delivery is a fast energy variation. At GSI different energies can be requested from the accelerator for each spill (approximately every 5 s). In a volume conformal irradiation of static targets the active energy variation is used to switch between different depths of the IES. By controlled changing of beam energy after one IES has been completed an extended target volume is homogeneously filled with dose.
For the experimental study a different approach was used. The energy of the extracted beam was changed during the irradiation of a single IES, simulating a change of WEL in front of the target.
The current energy settings can be extracted from the status information of the accelerator electronically, at any time. This information is used for automatic compensation of the longitudinal beam position. The energy settings are read out via a dedicated CAMAC interface. The energy range correlation used as an input for the motion compensation was verified for all applied energy settings by a separate measurement with the water column setup.

Density Changes in Front of the Target Volume

Active energy variation is only possible between two beam spills, i. e. approximately every 5 s. While this is enough for a general test of the functionality of the 3D-OMC system, it is not sufficient to study the feasibility for the compensation of respiration-related target motion. In contrast to a respiration-like displacement, the changes in WEL induced by the active energy variation are slow and discrete.
In a different approach, the density distribution in front of the target was altered. A suitable object had to be found, which on the one hand was flexible enough to allow deformation, but having enough elasticity to retain its original form without the deforming force. On the other hand, a high atomic density is necessary to produce a significant effect on the WEL. A water filled rubber ball[2] combined all three requirements. Unmodified, the air-filled ball measured 70.0±2.5 mm in diameter. In order to increase the density, the air was slowly substituted by water, using a syringe. To achieve a periodical deformation, the ball was placed into a piston, made from plexiglass and Teflon (cf. fig. 6.3). Excentrically attached to a rotary stepping motor the piston compressed the water filled ball in vertical direction. Due to the incompressibility of the water and the elasticity of the ball, this compression transferred into an isotropic, horizontal expansion. The distance between mounting point and centre of rotation was (6.0 ± 0.6) mm, yielding a stroke of (12 ± 1.2) mm. The effective WEL of the whole setup (including the piston walls, the rubber envelope and the water filling) in the maximum relaxed position was verified with the water column setup to amount to 88.64 ± 0.21 mm. As the horizontal extension

[2] Anti-Stress Ball, John Inc., Freilassing, Germany

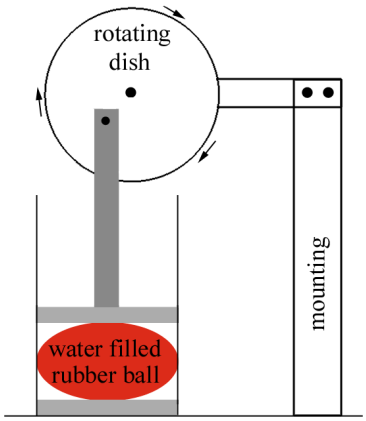

Figure 6.3:
Schematic setup for changing the WEL in front of the target volume. A water filled rubber ball is periodically deformed by a stepping motor driven piston. Due to the incompressibility of the water and the elasticity of the ball, a vertical compression results in an isotropic, horizontal expansion. Via the rotation angle of the motor, measured with an encoder, the position of the piston and thus the state of deformation of the ball is determined.

of the ball is increased, the surrounding air is substituted by a part of the water filled ball. Consequently, the beam has to penetrate a larger amount of water in the longitudinal direction than in the case of a relaxed ball, which corresponds to an increased WEL in front of the target. A continuous motion of the piston during irradiation causes a continuously changing WEL. The correlation between piston position (encoder) and the change in WEL was determined in advance by a relative measurement with the water column setup (cf. chapter 6.2.3). Due to the size of the rubber ball, a lateral beam deflection would alter the WEL, even if the ball remains in the same state of compression, leading to a complex encoder-WEL correlation. In the feasibility study the lateral beam position was kept fixed for all experiments.

6.2 Online Motion information

6.2.1 Data Connection

The availability of very accurate and reliable motion information is a crucial condition for successful 3D-OMC. All motion inducing devices used in the feasibility study were designed to support electronic read-out of the motion information at any time. An intrinsic time lag is caused by the data transmission between the encoder interface (currently CAMAC) and the 3D-OMC system. A detailed investigation of the time behaviour of the data connection is presented in appendix F.

Two different types of data connection were investigated. In one case the encoder data is transmitted to the 3D-OMC system at a fixed rate and the newest data is taken for compensation when needed (passive, TCP/IP-based). In the other case, the 3D-OMC system requests the displacement data at the time of compensation (active, VSB[3]-based). In general, the time lag introduced by both data connections is sufficiently small to determine the actual target position with a precision of better than 1 mm. Assuming an average target velocity of $15\,\frac{\mathrm{mm}}{\mathrm{s}}$, the timing-related inaccuracy is (0.25 ± 0.23) mm and (0.39 ± 0.23) mm for the active and passive connection, respectively. The feasibility study for 3D-OMC is based on the active solution.

6.2.2 Lateral Positioning Accuracy

The 3D positioning table is equipped with encoders, monitoring the motion of the motor or axis they are attached to with a precision of $\sigma{=}\pm5\,\mu$m. Due to rigid mechanics, this precision is transferred to the mounting of the object table. The three-dimensional position of the object table can be measured with an accuracy of better than $\pm9\,\mu$m. Such a small error can certainly be neglected for the feasibility experiments and the measured, lateral displacement were considered to be absolutely accurate.
To eliminate large uncertainties in the absolute detector position, dedicated reference marks were added to the irradiation plan for the film and BANG$^{\mathrm{TM}}$ gel experiments. These marks are single points or lines being irradiated on the resting detector, after or before the treatment plan. The position of these marks depends on the precision of the static beam delivery. The measured data is analysed relative to these marks.

6.2.3 Accuracy of Depth Variation

The longitudinal beam position is measured with the water column setup (cf. chapter 6.3.1). The accuracy of this measurement depends on the form of the Bragg curve, which changes with energy, and on the step size of the data points. For a typical energy of $200\,\frac{\mathrm{MeV}}{\mathrm{u}}$ and a data point step size of $50\,\mu$m, the absolute position of the Bragg maximum can be determined with an accuracy of $\sigma{=}\pm0.1$ mm. The relative position information required for the feasibility study is obtained by comparing the position of two curves with a similar shape. Overlaying the curves in one graph, the relative offset can be determined with a much higher precision than the absolute position.
For the density changes in front of the target volume a large source of error is the reproducibility of the rubber ball deformation. Correlated to the piston motion

[3]VME Subsystem Bus

the deformation measurement is affected by the elasticity of the rubber ball, the slackness of the mounting of the connecting rod and the tilt of the piston. The total error in the correlation between encoder reading and longitudinal expansion was determined monitoring the ball extension optically and with the water column setup over several motion cycles. In the optical case, snapshot photographs were taken from the rubber ball in different motion states. For each motion state the ball dimensions were extracted on a pixel basis via digital image processing. Each of the images contained a reference scale to precisely determine the pixel dimensions. With this method the relative change in diameter could be determined with a spatial precision of $\sigma = \pm 1\,\mathrm{mm}$. Variations in the rubber skin thickness over the motion cycle could be neglected. Fig. 6.4 shows the results of these measurements. The deformation of the rubber ball follows a general pattern but the absolute values vary significantly from cycle to cycle. According to an empirical finding, the deformation pattern is described best by an 8^{th} grade polynomial. The state of

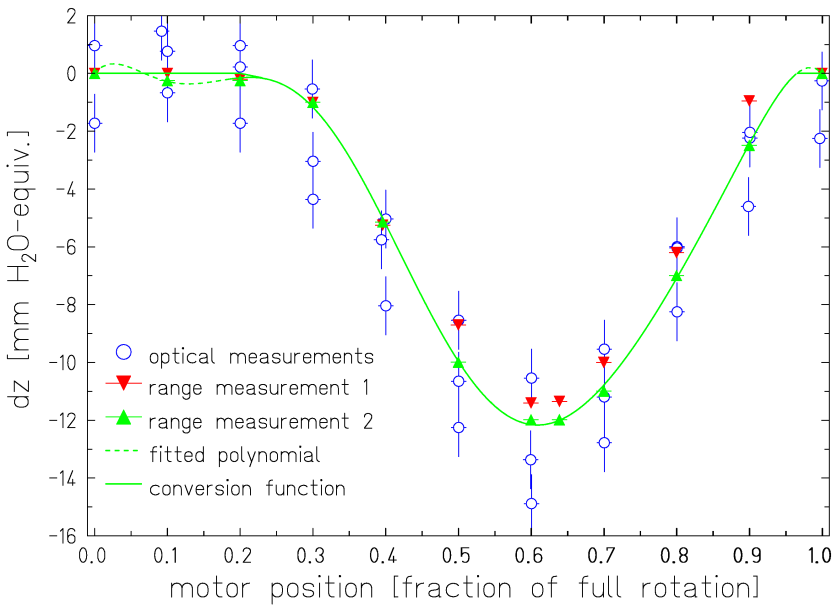

Figure 6.4:
Calibration of the irradiation phantom for density variations. The graph shows the change in ball dimension (dz) over several motion cycles, measured via digital imaging (optical) and with the water column setup (range). To convert the motor position into a longitudinal displacement, a conversion function was fitted to one of the range data sets. This function consists of a 8^{th} grade polynomial, which is forced to zero during the maximum expansion of the ball. (For the range measurements, the error bars on the change in WEL are smaller than the symbols.)

maximum expansion was taken as the reference for the changes in WEL. As a result of the piston height alignment, the rubber ball remains fully expanded for a longer time than fully compressed. This behaviour is similar to the breathing pattern, where the state of full exhalation lasts longer than the maximum inhalation. Since the ball is fully expanded in this state, the conversion function is forced to zero. The resulting function, fitted to one of the range measurements, is shown as a solid line in fig. 6.4. A statistical analysis of all calibration data sets shows that this conversion function describes the changes in WEL with an accuracy of σ=$\pm$1.56 mm.

6.3 Experimental Verification of Dose Distributions

The basic intention of 3D-OMC is the application of equivalent dose distributions, independent of the target's state of motion. The performance and feasibility study of the prototype setup is based on the comparison of delivered dose distributions to static and moving targets by means of relative dose measurements. Depending on the investigated issue, three types of dose detectors were used: water column setup, x-ray films and BANG^{TM} gels.

6.3.1 Water Column for Depth Dose Verification

The Bragg curve, or depth dose distribution, is measured with an ionisation chamber and a motor-driven water column of variable thickness [Sch93a]. Fig. 6.5 schematically shows the water column setup. The actual thickness of the water column is determined by means of an optical linear encoder. An ionisation chamber measures the specific ionisation of the heavy ion beam behind the water tank. For determination of the specific ionisation at different depths the thickness of the water column is changed between two consecutive spills leading to a variation of WEL in front of the detector. Plotting the measured specific ionisation versus the thickness of the water column yields the depth dose distribution. Variations in the beam intensity between two data points are eliminated by normalising the signal to the ion flux, measured by an additional ionisation chamber in front of the water column.

6.3.2 X-Ray Films for Lateral (2D) and 3D Dose Verification

X-ray films are a common tool in conventional therapy for dosimetric applications, combining direct visualisation of the applied dose distribution with high spatial resolution and a relatively easy handling. For quantitative analysis the films are digitalised in dedicated film scanners. The limitation of films, as any solid state detector, is the strong dependence of film response $m(Z, E)$ on ion species (Z) and energy (E) [Spi01]. Especially in mixed particle radiation fields, absolute film

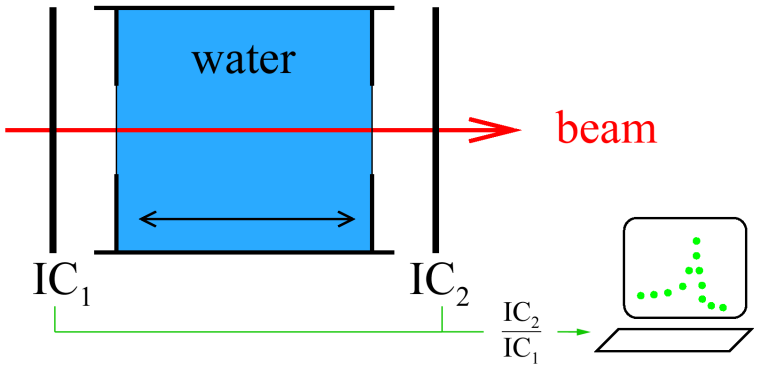

Figure 6.5:
In the water column setup the specific ionisation of charged particles crossing a certain distance of water is measured with an ionisation chamber (IC). By changing the thickness of water, the position of the measurement is varied. The plot of the specific ionisation versus the depth of the measurement yields the depth dose distribution. To account for fluctuations in the initial ion beam, the signal is normalised to the specific ionisation measured by an additional IC in front of the tank.

dosimetry is not possible. But if the field composition as well as the corresponding film responses $m(Z, E)$ are known [Spi02] the applied dose can be verified with high accuracy in two and three dimensions [Spi03a, Spi03b]. Based on this data set, the expected signal of the irradiated films can be calculated with the treatment planning software TRiP98 [Krä01] and finally compared with the experimental data. With the actual energy and fragment spectra included in TRiP98, as well as a model to calculate film responses for all particle types and energies [Spi01], the measured and calculated film signals agree better than 3 %, even for extended target volumes. All measurements of the experimental feasibility study in this thesis were carried out with the Kodak X-Omat V film (size: $24 \times 30\,\mathrm{cm}^2$; thickness: $182\,\mu m$), a classical silver bromide film frequently used in radiotherapy. Each film is single packed in a light-tight paper sheet (ready pack) with a thickness of $250\,\mu m$ [Spi01] on each side. For film developing a Kodak M35 processing machine with the developer DX31 and fixer FX31 was used. After development the films were read out and digitalised with a FIPS Plus LS75 laser densitometer[4] using a medium spatial resolution of $\approx 0.3\,\mathrm{mm}$ for the scanning process and 1 mm for the data extraction.
The shape of the characteristic curve of a film detector (dose response curve), describing the relation between applied dose D and optical density $optD$, is expressed by a purely exponential function

$$optD(\mathrm{D}) = optD_{max}[1 - \exp(-m(Z, E)\mathrm{D})] \tag{6.3}$$

[4]PTW Freiburg, Germany

with the saturation optical density $optD_{max}$ and the exponential slope (film response) $m(Z, E)$ [Spi01]. The deposited dose is derived from the particle fluence according to eq. (2.2).
For the study of extended 3D dose distributions, several films are stacked between polyethylene (PE) absorbers. Fig. 6.6 shows the setup of the film stack used for 3D dose verification measurements in this thesis.

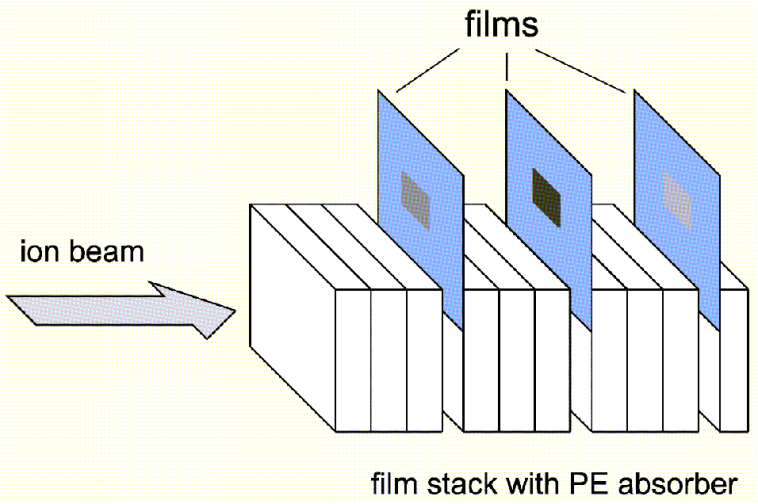

Figure 6.6:
Film stack for verification of 3D dose distributions. Several films are arranged between polyethylene absorbers simulating an extended volume. (taken from [Spi03a])

To calculate the expected optical density in every point $\vec{r}$ of the irradiated volume, it has to be considered that the physical dose is composed by a mixed particle field, containing different ion species (primary ions and fragments) with a spectrum of energies. The sum over all these contributions weighted with the corresponding film response yields an effective dose D_{eff} and the correlation between optical density ($optD$) and applied dose is calculated by [Spi03a]

$$optD(\vec{r}) = optD_{max}[1 - \exp\left(-\mathrm{D}_{eff}(\vec{r})\right)]. \tag{6.4}$$

For known radiation fields 3D film dosimetry is an excellent tool to verify the dose distribution. To evaluate the performance of the 3D-OMC system the optical density distribution of an exposed, 2D area perpendicular to the beam was studied, which required no detailed fragment analysis. According to eq. (6.3) the optical density depends on two parameters: the saturation density $optD_{max}$ and the film response m. While m characterises the physical processes of the interaction between radiation and film, $optD_{max}$ is determined by the developing conditions [Spi03a].

Even if an automatic film processing unit is used, $optD_{max}$ can vary significantly from day to day. In the feasibility study, the absolute value of $optD_{max}$ was determined for each experiment with a calibration curve. The calibration curve is a fit of the dose response curve on the net (background free), measured optical density in dependence of the particle fluence of a set of calibration fields. Fig. 6.7 shows

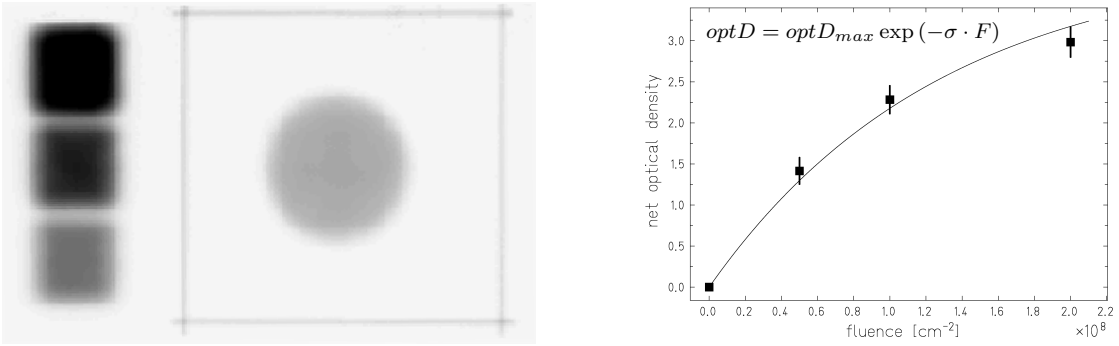

Figure 6.7:
Example of the calibration of the film response. The saturation optical density $optD_{max}$ is determined by a fit to the measured optical density ($optD$) in dependence of the ion fluence (F) in three calibration fields irradiated on each film.

a sample film from the feasibility study and the corresponding calibration curve. The three calibration fields are visible at the left side of the film and the target volume at the right is encircled by the reference frame for aligning the film position. The large error bars on the measured optical density in the calibration curve (right figure) reflects the inhomogeneity within the calibration fields due to their limited size. In order to compare the data sets among each other and with the results of the treatment planning software, all film data in this thesis are normalised to $optD_{max} = 1$.

6.3.3 BANG™ Gels for full 3D Dose Verification

In contrast to 3D film dosimetry, BANG™ gel dosimetry provides full 3D information on the dose distribution within an extended target volume [e. g. Gor84, Mar93, Ram00]. BANG™ gels consist of acrylic monomers which are homogeneously embedded in an aqueous matrix. Ionising radiation induces polymerisation and cross linking of these monomers, affecting the mobility of the water protons. The formation of polymer chains reduces the spin-spin relaxation time of the hydrogen atoms [Ahl98] which can be measured with magnetic resonance imaging (MRI) by a dose dependent transversal relaxation rate R_2. Due to the

isotropic monomer concentration, the spatial resolution is only limited by the MRI resolution.
Similar to film dosimetry, the strongly LET dependent relative efficiency in BANG^{TM} gels has to be determined for mixed radiation fields. While the detailed behaviour of these gels in heavy ion beams is still under investigation, gel dosimetry is already used for relative dose measurements with a high 3D resolution.
In the feasibility study for 3D-OMC, BANG^{TM} gel measurements were performed, to verify the compensation performance over the whole, extended target volume. For good dose resolution BANG-3^{TM}gels (MGS Research, Guilford, USA) with the highest MR sensitivity on photon irradiation [Ram00] were used[5]. Stored in special Pyrex glass vessels, the gels were irradiated through the bottom of the container, yielding a cylindrical gel geometry around the beam axis.

[5]The dose range of maximum sensitivity was tuned to 5-8 Gye during the manufacturing process.